XLIIIrd RENCONTRES DE MORIOND

# Electroweak Interactions and Unified Theories

## VI - Young Scientists Forum

# The Z Transverse Momentum Distribution

T. Andeen for the DØ Collaboration
*Department of Physics and Astronomy, Northwestern University, Evanston, Illinois, USA*

The DØ collaboration has measured the transverse momentum of the Z boson in the process $Z/\gamma^* \to ee$. This is compared to a theoretical model of the boson transverse momentum and found to agree well with the existing parametrization. This parametrization is a critical input in the measurement of the W boson mass measurement, which is discussed briefly.

## 1 Introduction

At leading order W and Z bosons are produced at the Tevatron predominately through the Drell-Yan diagrams shown in figures 1 and 2, where the only particle in the final state is the boson. Without anything to recoil against the boson is necessarily produced at rest in the $q\bar{q}$ frame. The partons themselves are assumed to have very little momentum transverse to the beam direction (from the confinement of the parton within the proton). Therefore the boson is produced with effectively no $p_T$.

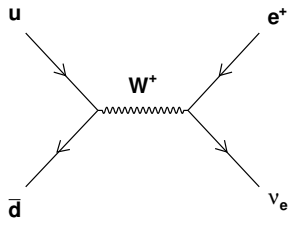


Figure 1: W boson production and decay at tree level.

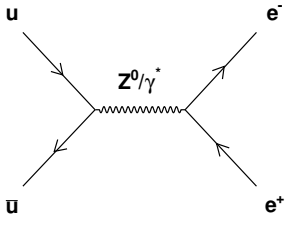


Figure 2: $Z/\gamma^*$ production and decay at tree level.

Higher order quantum chromodynamics (QCD) processes involve additional particles in the final state. The most straightforward to consider are the initial state radiation of a gluon (ISR)

and the Compton radiation of a gluon (figure 3). This additional particle gives the boson something to recoil against. Typically this results in a boson $p_T$ of several GeV.


Figure 3: W boson production at next to leading order. Here the boson recoils against the gluon, resulting in non-zero boson transverse momentum.

## 2 Boson Production

A complete discussion of the $p_T$ distribution of electroweak bosons at production is a significant undertaking, the full details of which are beyond the scope of this discussion. However, because of the critical role the description of boson production plays in the measurement of the W boson mass, as well as searches for production of the Higgs boson and other beyond the Standard Model physics, we describe several of the important phenomenological details. The differential cross section with respect to the boson transverse momentum is written as

$$\frac{d^2\sigma}{dP_T^2} = \sum_{ij} \int dx_1 dx_2 f_i(x_1) f_j(x_2) \frac{d^2\sigma(ij \to V)}{dP_T^2}. \tag{1}$$

For the process $qg \to W\bar{q}$ shown in figures 3 one can accurately calculate the transverse momentum distribution at high $p_T$ ($p_T \approx M_{\text{Boson}}$) using perturbative QCD. In the low $p_T$ region the results are divergent. A framework was developed by Collins, Soper and Sternman [1] to re-sum the perturbation series by grouping the divergent, non-perturbative terms together. This re-summation works for all orders in perturbation theory but requires a correction at low-$p_T$ where non-perturbative physics becomes important. The correction is parameterized with a function $W$ that smoothly turns off as the boson $p_T$ increases. The parton level cross section is then

$$\frac{d^2\sigma(q\bar{q} \to V)}{dP_T^2} \sim \int_0^\infty \left[ d^2b e^{i\vec{P}_T \cdot \vec{b}} \times W(b,Q) \right] + Y(P_T, Q) \tag{2}$$

where $Y$ is the perturbative piece and the impact parameter $b$ is the conjugate variable of $p_T$ (as $b$ increases $p_T$ decreases). The form of the $W$ function is phenomenologically motivated and is determined by fitting data from several experiments. Recently the form

$$W_{NP}(b) = \exp\left( -\left( g_1 + g_2 \ln\left( \frac{Q}{2Q_0} \right) + g_1 g_3 \ln(100 x_1 x_2) \right) b^2 \right) \tag{3}$$

was proposed by Brock, Landry, Nadolsky and Yuan [2], where in this case

$$Q \sim 91\text{GeV},\ Q_0 = 1.6\text{GeV},\ x_{i,j} \sim 0.05 \tag{4}$$

and the parameters

$$g_1 = 0.21 \pm 0.01\ \text{GeV}^2\ \ g_2 = 0.68^{+0.01}_{-0.02}\ \text{GeV}^2\ \ g_3 = -0.60^{+0.05}_{-0.04} \tag{5}$$

are determined through global fits. In the kinematic region we are interested in the $g_2$ term dominates. Independent of the global fits the DØ experiment uses the transverse momentum spectrum of $Z \to ee$ decays to determine $g_2$.

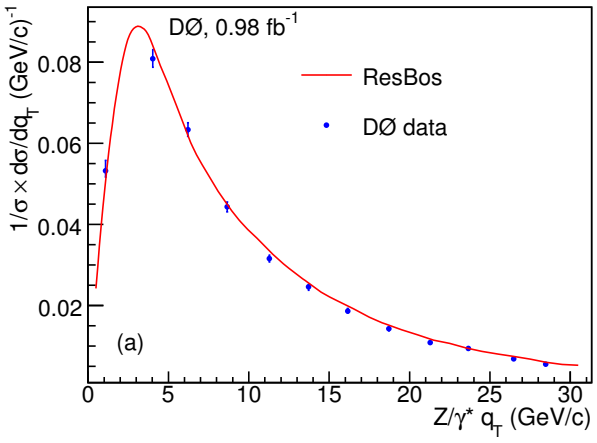


Figure 4: $Z/\gamma^*$ transverse momentum distribution with boson $|y| < 2.0$. The points are the data and the solid line is the ResBos prediction.

## 3 Z Transverse Momentum Analysis

The event selection used to collect Z boson candidates requires two isolated electromagnetic (EM) clusters that have a shower shape consistent with that of an electron and are away from the module boundaries of the calorimeters. Electron candidates are required to have transverse momentum greater than 25 GeV. The pairs of electrons must have a invariant mass $70 < M(ee) < 110$ GeV . If both electrons are in the central calorimeter, then each electron must be spatially matched to a reconstructed track. The central section of the calorimeter has coverage for electrons of $|\eta| < 1.1$ and two endcap calorimeters have an approximate coverage of $1.5 < |\eta| < 3.2$ for electrons ($\eta = \ln[\tan(\theta/2)]$). In figure 4 the Z boson $p_T$ distribution is shown corrected for efficiencies, background and acceptance and then unfolded to obtain the true differential cross section[3]. The curve is the ResBos [4 5 6] prediction using the BLNY parametrization.

We fit for the parameter $g_2$ using the distribution in figure 4 and find the best fit value to be $g_2 = 0.77 \pm 0.06$. This is then used as an input in the measurement of the W mass.

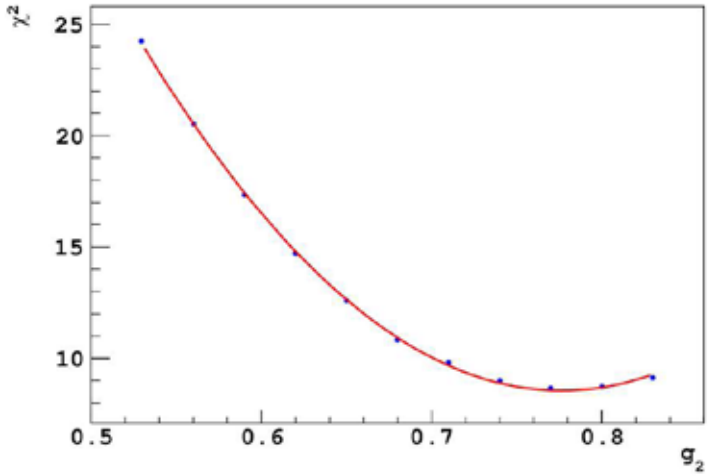


Figure 5: The $\chi^2$ as a function of the $g_2$ parameter using the unfolded data and the BLNY model. The solid line is a polynomial fit.

## 4 Implications for W Mass Measurement

To measure the W boson mass using the $W \rightarrow e\nu$ decay channel a theoretical description of the boson's transverse momentum is necessary. This is because the invariant mass cannot be reconstructed from the electron/neutrino final state. Instead, the sensitivity of the electron transverse momentum and the transverse mass (analogous to the invariant mass) distributions to the W boson mass are exploited. The electron $p_T$ and the transverse mass distributions cannot be described analytically so a theoretical description of the boson production and decay is employed, in conjunction with a parameterized detector simulation. Using the parametrization in [5] with the value for the $g_2$ parameter determined above we estimate the contribution to the overall uncertainty on the W boson mass at DØ (using approximately 1 fb$^{-1}$ of data) to be 5 MeV for the transverse mass distribution and 16 MeV for the transverse momentum distribution. With a total estimated statistical uncertainty of 17 MeV using the transverse mass distribution (23 MeV using the electron $p_T$ distribution) for this sample this aspect of the theoretical description is not the dominate uncertainty.

### Acknowledgments

We thank the staffs at Fermilab and collaborating institutions, and acknowledge the support of the U.S. Department of Energy, the National Science Foundation and the European Union Marie Curie Programme.

### References

1. J. Collins, D. Soper, G. Sternman, *Nucl. Phys.* B **250**, 199 (1985).
2. F. Landry, R. Brock, P. Nadolsky, C.-P. Yuan, *Phys. Rev.* D **67**, 073016 (2003).
3. V. Abazov *et. al*,*Phys. Rev. Lett.* **100**, 102002 (2008).
4. G. Ladinsky, C.-P. Yuan, *Phys. Rev.* D **50**, 4239 (1994).
5. C. Balazs, C.-P. Yuan, *Phys. Rev.* D **56**, 5558 (1997).
6. E. Barberio, Z. Was, Comput. Phys. Communications, **79**, 291, (1994).

# Precision Top Quark Mass From a Simultaneous Fit in Lepton + Jets and Dilepton Channels Using 2 $\mathrm{fb}^{-1}$ of data collected by the CDFII detector

Wojciech Fedorko
(on behalf of the CDF collaboration)
*University of Chicago, 5640 S. Ellis Avenue, Chicago, IL 60615, USA*

We present a preliminary measurement of the top quark mass employing the template method with data sample collected by the CDF Run II detector corresponding to integrated luminosity of 2 $\mathrm{fb}^{-1}$. Lepton + Jets and Dilepton final states are selected. For each event in the Lepton + Jets channel we apply kinematic constraints on the pair of top quarks and their decay products to determine a reconstructed top quark mass. We simultaneously determine the invariant mass of the decaying W boson to calibrate the energy response of the detector. The events in the Dilepton sample are reconstructed using the Neutrino Weighting Algorithm. To improve the precision, for each Dilepton event we calculate $H_T$ - the linear sum of missing transverse energy and transverse momenta of jets and leptons. The reconstructed top quark mass and W boson invariant mass distributions from the Lepton + Jets channel and reconstructed top quark mass and $H_T$ distributions from the Dilepton channel are fit to Monte Carlo derived templates in a likelihood fit to extract the top quark mass and an *in-situ* measurement of the jet energy scale. We measure $\mathrm{M_{top}} = 171.9 \pm 2.0$ GeV/$c^2$.

## 1 Introduction

Since it's discovery [1,2] at the Tevatron the top quark has been one of the most studied fundamental particles. It is more than an order of magnitude heavier than the next heaviest Standard Model fermion. This points to it's crucial role in a puzzle of the origin of mass. The top quark and the Higgs boson contribute in the loop corrections to the W boson mass, therefore knowing precisely the top quark mass and the W boson mass allows to constrain indirectly the Higgs boson mass [3]. Once the Higgs boson is discovered the knowledge of it's mass together with measurements of the top quark mass and the W boson mass will provide a sensitive test of the Standard Model [4]. Current measurements of the top quark mass and the W boson mass may be giving us hints on the nature of physics beyond the Standard Model [5]. In this letter we present a preliminary top quark mass measurement using the Lepton + Jets and Dilepton decay channels simultaneously. This approach is applied for the first time in a top quark mass measurement. More details on this analysis can be found in [6].

## 2 Top Quark Production and Decay

Top quarks are produced at the Tevatron mainly in quark-antiquark anihilation events where a gluon is produced, splitting into a $t\bar{t}$ pair. Each of the top quarks then decays into a $W$ boson and a $b$ quark with essentially 100% branching fraction. The $W$ bosons can decay into a quark pair or a charged lepton-neutrino pair, giving rise to classification of the $t\bar{t}$ decays into three

classes. Thus we have an All-hadronic decay channel with six jets in the final state, a Lepton + Jets decay channel where we find four jets, one lepton and missing transverse energy and a Dilepton decay channel characterized by two leptons, two jets and missing transverse energy. Due to difficulty of reconstructing $\tau$ leptons we restrict the meaning of lepton to an electron or a muon.

## 3 Combination Strategy

Measurements in all decay topologies are valuable as statistically independent cross-checks and are all needed to obtain best precision possible. Traditionally a dedicated analysis is performed in each channel and the results are combined using an averaging technique [7]. In any such combination one must assume the values of correlations in systematic effects between the measurements in different channels. A form of the likelihood shape is also required as an input and is usually assumed to be Gaussian. In this letter we present a preliminary top quark mass measurement using two decay channels simultaneously. The analysis presented here allows us not to make any assumptions mentioned above, yielding a more robust measurement.

## 4 The Jet Energy Scale

In the top quark mass measurements a major source of uncertainty is the modelling of the jet callibration or the jet energy scale (JES). Multiple effects contribute to the uncertainty on the jets [8]. A major uncertainty arises from modelling of nonlinearities of the calorimeter and energy loss in uninstrumented regions (absolute energy scale). Flow of particles outside of the jet cone (out of cone energy scale) gives large uncertainty especially for low energy jets. Another large systematic uncertainty arises from detector nonuniformity as a function of the pseudorapidity (relative energy scale). Interactions of the spectator partons (underlying event energy scale) and additional soft $p\bar{p}$ interactions in the same bunch crossing are sources of small systematics. We measure the offset from a nominal calibration in units of the total systematic uncertainty on the calibration $\sigma_c$. In Lepton + Jets channel presence of a hadronically decaying $W$ boson allows us to callibrate *in-situ* the value of the shift $\Delta_{\mathrm{JES}}$ from the nominal JES. Since the measurement is performed in two channels simultaneously this callibration will be applied uniformly to the two decay channels used.

## 5 Event Selection

### *5.1 Lepton + Jets Channel*

To select the Lepton + Jets sample we require at least four jets with high transverse energies. At least one of the jets has to be identified as a $b$ quark jet based on a presence of a secondary vertex or a "b-tag". We separate the Lepton + Jets sample into 1-tag and 2-tag subsamples. In the 1-tag sample we require that there are exactly four jets with transverse energies greater than 20 GeV when corrected to the paritcle level. In the 2-tag samples we relax the energy for the fourth most energetic jet to have $E_T > 12$ GeV. We also allow additional jets in the event. We require a central electron or a muon with $E_T$ or $p_T > 20$ GeV. The missing transverse energy must be greater than 20 GeV.

The background estimate for the Lepton + Jets samples is obtained form combination data - Monte Carlo technique. The major backgrounds arise from production of $W$ boson in association with heavy flavour jets and light flavor jets where the light flavour jet is tagged (so called "mistag") and from QCD events where one of the jets is misidentified as a lepton. We expect in the 1-tag sample $42.7 \pm 12.5$ and in the 2-tag $4.2 \pm 1.9$ background events.

### *5.2 Dilepton Channel*

We require at least two jets with $E_T > 15$ GeV. Two leptons of opposite charge must be present with transverse energies of at least 20 GeV. If the leptons are of the same flavor we impose the requirement that their invariant mass lies at least 15 GeV/$c^2$ from the $Z$ boson mass. Additionally we require that $H_T > 200$ GeV, $\not\!\!E_T > 25$ GeV where $H_T$ is a linear sum of $\not\!\!E_T$ and transverse energies of jets and leptons. Topological cuts designed to remove events where $\not\!\!E_T$ arises due to instrumentational effects or $\tau$ production are applied. The Dilepton sample is divided into two subsets: a 0-tag sample and a 1-tag sample.

The background contributions to the Dilepton channel include events where a lepton is produced in association with jets and one of the jets is reconstructed as a lepton ("Fakes"), Drell-Yan production and diboson production. The Fakes background is estimated from data while other backgrounds are estimated using data-Monte Carlo and Monte Carlo only techniques. In the non-tagged sample we expect $31.1 \pm 5.6$ and in the tagged sample $2.4 \pm 0.6$ background events

### *5.3 Event Reconstruction*

In each event we form a reconstructed top quark mass, a variable which is highly sensitive to the true top quark mass. In the Lepton + Jets channel we use a $\chi^2$ fit where the magnitudes of lepton and jet momenta and the transverse components of unclustered energy are allowed to float within their resolution around the observed values. We impose a constraint that the invariant masses of the neutrino-lepton system and the light quark system are close to the measured $W$ boson mass. The invariant mass of the leptonically decaying top quark daughters is constrained to be within the theoretical top quark width from the invariant mass of the hadronically decaying top quark daughters. The constraint is impsed through fit parameter taken to be the reconstructed top quark mass. The $\chi^2$ minimization is performed for all jet-to-quark assignmets consistent with b-tagging combination and the combination with lowest minimum $\chi^2$ is used. To form a reconstructed top quark mass in the Dilepton channel events we use the Neutrino Weighting Algorithm. We scan a range of top quark masses. At each point in the scan we integrate over the pseudorapidities of the two neutrinos and sum over the two possible jet-to-quark assignments. Knowing the top quark mass, neutrino pseudorapidities and masses of all particles in the decay cascade we solve for the neutrino transverse momenta. The integrand is formed by a Gaussian weight that compares the measured $\not\!\!E_T$ value to the solution obtained for the neutrino transverse momenta. The top quark mass in the scan that yields the highest weight is taken as the reconstructed top quark mass in this event. Additionally in each Dilepton event we calculate the $H_T$. In the Lepton + Jets channel we reconstruct also the invariant mass of the hadronically decaying $W$ boson. As mentioned above this variable captures the shifts in JES.

### *5.4 Mass Fitting*

We employ a template approach in this analysis. We generate $t\bar{t}$ Monte Carlo samples with a range of top quark mass and JES shifts. We also construct background models using data and Monte Carlo samples. We form probability density functions (pdf) for the observables mentioned above and compare them to the distributions of the observables obtained from data in an extended likelihood fit, to obtain a measurement of the top quark mass $\mathrm{M_{top}}$ and the jet energy scale shift $\Delta_{\mathrm{JES}}$. The probability density functions are constructed using the Kernel Density Estimation (KDE) techniques [9,10,11]. In this approach the probability for an event to have certain values of the observables is calculated as a sum of values of kernel functions from all events in a given Monte Carlo sample. This technique treats intrinsically the correlations

between observables. KDE gives the value of signal pdf at distinct values of $M_{top}$ and $\Delta_{JES}$ where Monte Carlo samples were generated. To obtain a pdf that varies smoothly as a function of those two parameters we use Local Polynomial Smoothing (LPS) [12]. LPS performs a fit to a parabolic function using the KDE estimates from Monte Carlo templates with the $M_{top}$, $\Delta_{JES}$ parameters lying close to the point where the estimate is desired. The value of the parabola at that point is interpreted as the pdf.

Using the distributions of observables in data, the negative log-likelihood is minimized for the top quark mass of 171.9 $\pm$ 1.7 (stat.+JES) GeV/$c^2$. Fitted $\Delta_{JES}$ value is consistent with nominal calibration of 0 $\sigma_c$.

## 6 Systematics

The largest systematic (0.6 GeV/$c^2$), $b$ quark jet energy scale arises due to differences in modelling $b$ and light flavour jets. As described in section 4 many effects contribute to uncertainty on JES. Modelling the offset from the nominal calibration as just one number $\Delta_{JES}$ gives source to the residual JES uncertainty of 0.5 GeV. Another large systematic (0.5 GeV/$c^2$ is due to the modelling of the initial and final state radiation. Additional systematics include generator differences (0.2 GeV/$c^2$), background shape (0.1 GeV/$c^2$), Monte Carlo sample statistics (0.1 GeV/$c^2$), lepton energy scale (0.1 GeV/$c^2$) and multiple $p\bar{p}$ interactions (0.1 GeV/$c^2$). Total systematic uncertainty is 1.0 GeV/$c^2$.

## 7 Conclusions

We performed the first top quark mass measurement simultaneously in two decay channels treating the correlations in the systematic effects intrinsically. No assumptions on the form of the likelihood needed to be made and the JES calibration was applied uniformly to both channels. The result obtained is:

$$M_{top} = 171.9 \pm 1.7 \text{ (stat.} + \text{JES)} \pm 1.0 \text{ (other syst.) GeV}/c^2 = 171.9 \pm 2.0 \text{ GeV}/c^2$$

## References


1. F. Abe et al. *Phys. Rev. Lett.*, 74:2626–2631, 1995.
2. S. Abachi et al. *Phys. Rev. Lett.*, 74:2632–2637, 1995.
3. L3 OPAL The LEP Collaborations ALEPH, DELPHI and the LEP Electroweak Working Group. arXiv:hep-ex/07120929. Updated for 2008 winter conferences, 03/19/2008 , http://www.cern.ch/LEPEWWG.
4. M Beneke et al. Top quark physics. arXiv:hep-ph/0003033v1.
5. D. Stockinger A.M. Weber G. Weiglein S. Heinemeyer, W. Hollik. arXiv:hep-ph/0604147.
6. CDF9206 CDF Collaboration. http : //www − cdf.fnal.gov/physics/new/top/confNotes/cdf9206_thepublictopmass_2.pdf
7. The Tevatron Electroweak Working Group for the CDF and DØ Collaborations. arXiv:hep-ex/0803.1683v1.
8. A. Bhatti et al. *Nucl. Instrum. Meth.*, A566:375–412, 2006.
9. David W. Scott. *Multivariate Density Estimation: Theory, Practice and Visualization.* Wiley-Interscience, 1992.
10. B. W. Silverman. *Density Estimation for Statistics and Data Analysis.* Chapman and Hall, 1986.
11. Kyle Cranmer. *Computer Physical Communcations*, 136(3):198–207, 2001.
12. Clive Loader. *Local Regression and Likelihood.* Springer, 1999.

# BiPo PROTOTYPE FOR SuperNEMO RADIOPURITY MEASUREMENTS

M. BONGRAND
(on behalf of the SuperNEMO collaboration)
*LAL, Université Paris-Sud 11, CNRS/IN2P3, Orsay, France*

The BiPo project is dedicated to the measurement of extremely low radioactive contaminations of SuperNEMO $\beta\beta$ source foils ($^{208}$Tl $< 2$ $\mu$Bq/kg and $^{214}$Bi $< 10$ $\mu$Bq/kg). A modular BiPo1 prototype with its 20 modules and its shielding test facility is running in the Modane Underground Laboratory since February, 2008. The goal of this prototype is to study the backgrounds and particularly the surface contamination of plastic scintillators. After 2 months, a preliminary upper limit on the sensitivity of a 10 m$^2$ BiPo detector in $^{208}$Tl contamination of selenium source foils can be extrapolated to: $\mathcal{A}(^{208}\text{Tl}) < 7.5$ $\mu$Bq/kg (90 % C.L.).

## 1 Principle

The BiPo detector is dedicated to the measurement of the high radiopurity levels in $^{214}$Bi and $^{208}$Tl of very thin materials and especially the double beta source foils of the SuperNEMO detector[1]. The expected sensitivity is $\mathcal{A}(^{208}\text{Tl}) < 2$ $\mu$Bq/kg and $\mathcal{A}(^{214}\text{Bi}) < 10$ $\mu$Bq/kg.

In order to measure $^{208}$Tl and $^{214}$Bi contaminations, the original idea of the BiPo detector is to detect the so-called BiPo process, which corresponds to the detection by organic scintillators of an electron followed by a delayed alpha particle. The $^{214}$Bi isotope is nearly a pure $\beta$ emitter ($Q_\beta = 3.27$ MeV) decaying into $^{214}$Po, an $\alpha$ emitter with a half-life of 164 $\mu$s (Fig. 1). The $^{208}$Tl isotope is measured by detecting its parent the $^{212}$Bi isotope. $^{212}$Bi decays with a branching ratio of 64 % via a $\beta$ emission towards $^{212}$Po ($Q_\beta = 2.25$ MeV) which is again an $\alpha$ emitter with a short half-life of 300 ns. So, for these two chains a BiPo signature is an electron associated to a delayed $\alpha$ with a delay time depending on the isotope contamination we want to measure.

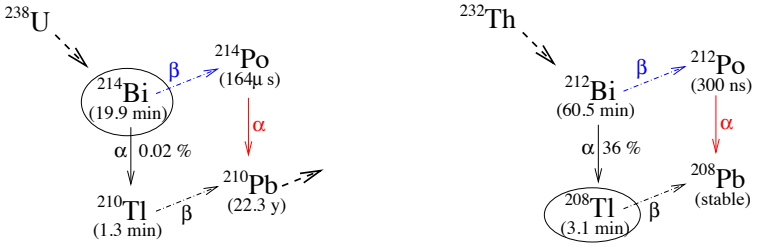


Figure 1: BiPo processes for $^{214}$Bi and $^{208}$Tl.

The particles emitted by the source foil are detected with plastic scintillators coupled to low radioactivity photomultipliers (Fig. 2). Plastic scintillators are very radiopure and reduce the backscattering of electrons. The detection efficiency is dominated by the capacity for an $\alpha$ particle to escape the foil. GEANT4 simulations give a total efficiency of 6.5 % for contaminations

in selenium foils (40 mg/cm$^2$) with 1 MeV threshold for $\alpha$. Therefore the energy threshold of the detector must be as low as possible. Moreover the energy converted into scintillation light is much lower for $\alpha$ compared to electrons. This quenching factor depends on the energy of the $\alpha$ and has been measured with a dedicated test bench[2]. For example, a 1 MeV $\alpha$ will produce same amount of light than a 40 keV electron.

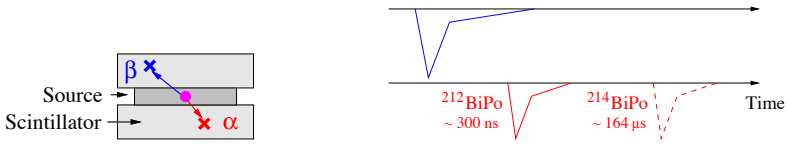


Figure 2: BiPo detection principle with plastic scintillators and time signal seen with PMTs. Dots represent the contamination and crosses represent energy depositions in scintillators (trigger in blue and delayed in red).

## 2 Backgrounds

The BiPo measurement consists in the detection of the electron in one scintillator and the detection of the delayed $\alpha$ particle in the other scintillator. This strong BiPo signature constrains the background of the detector to only 3 processes:
- bismuth ($^{212}$Bi or $^{214}$Bi) contaminations in the volume of the scintillator. In such decay the electron deposits part of its energy in the first scintillator before crossing the foil to reach the other one. The delayed $\alpha$ is detectable only in the first scintillator because it can't cross the foil. This background can be rejected because two hits in time are observed in the two scintillators: this is not a BiPo event. (Fig. 2a)
- bismuth contaminations on the surface of the scintillator[a]. In this case the electron doesn't deposit enough energy in the first scintillator to be detected. The delayed $\alpha$ particle is still detectable only in this first scintillator. This contamination is not distinguishable from a BiPo signal because this signature exactly corresponds to a BiPo event coming from the foil. (Fig. 2b)
- random coincidences due to external $\gamma$. To reduce this background, the BiPo detector uses low background materials, is shielded and installed in underground lab. The single counting rate of each scintillator has to be less than 40 mHz to measure $^{208}$Tl and less than 10 mHz for $^{214}$Bi because of $^{214}$Po longer half-life. Pulse shape discrimination also reduces this background. (Fig. 2c)

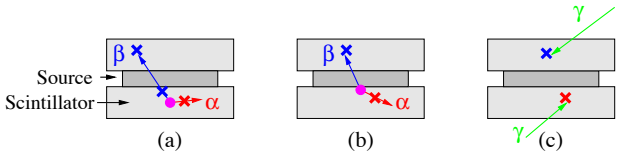


Figure 3: Surface and volume bismuth contaminations of the scintillators and random coincidences backgrounds.

## 3 BiPo1 prototype

BiPo1 prototype is divided in 20 modules. Each module is a black box containing two polystyren based scintillators coupled to low background 5" photomultipliers with PMMA light guides. Scintillator dimensions are 20×20×1 or 20×20×0.3 cm$^3$, the entrance window is covered with 200 nm of ultra-pure aluminum to isolate optically each scintillator and to improve the light collection. The sides of scintillators and light guides are covered with 0.2 mm of Teflon for

[a] Small thickness where the energy deposited by the electron is below the threshold ($\sim$ 100 $\mu$m for 150 keV).

light diffusion. The prototype is installed in the Modane Underground Laboratory (LSM) under 4800 m.w.e.. Surrounding the modules, a shielding of 15 cm of low activity lead reduces external $\gamma$ and 3 cm of pure iron stops bremsstrahlung $\gamma$ emitted in the lead by the decay of the $^{210}$Bi from long half-life $^{210}$Pb. Radon-free air flushes the volume of each module and the inner volume of the shielding (Fig. 4).

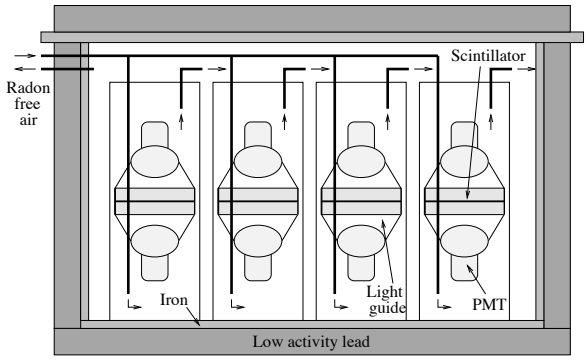


Figure 4: BiPo1 prototype in its shielding in LSM.

Photomultipliers signals are sampled with VME digitizing board[3], during 2.5 $\mu$s with a high sampling rate (1 GS/s) and a 12 bit high dynamic range (1 V). The acquisition is triggered each time a pulse reaches the 150 keV energy threshold and the 2 photomultipliers signals from a module are stored. The delayed hit research is performed later by the analysis of the signals (Fig. 5).

## 4 BiPo1 calibration

The first BiPo1 module has been dedicated to the validation of the detection principle for $^{212}$Bi contaminations inside a foil. A 150 $\mu$m aluminum foil (40 mg/cm$^2$) with a contamination measured with HPGe detectors of $\mathcal{A}(^{212}\text{Bi}\rightarrow^{212}\text{Po}) = 0.19 \pm 0.03$ Bq/kg, has been installed between the two scintillators. After 141 days of data taking, 1501 BiPo events have been detected. Taking into account the efficiency calculated by GEANT4 simulations, it corresponds to a reconstructed activity of $\mathcal{A}(^{212}\text{Bi}\rightarrow^{212}\text{Po}) = 0.22 \pm 0.01$ Bq/kg, in good agreement with initial HPGe measurement. The delay between the two hits is also measured, and the fit of the decay law perfectly corresponds to the $^{212}$Po half-life (Fig. 5). These results are a strong validation of the measurement principle and the calculated efficiency.

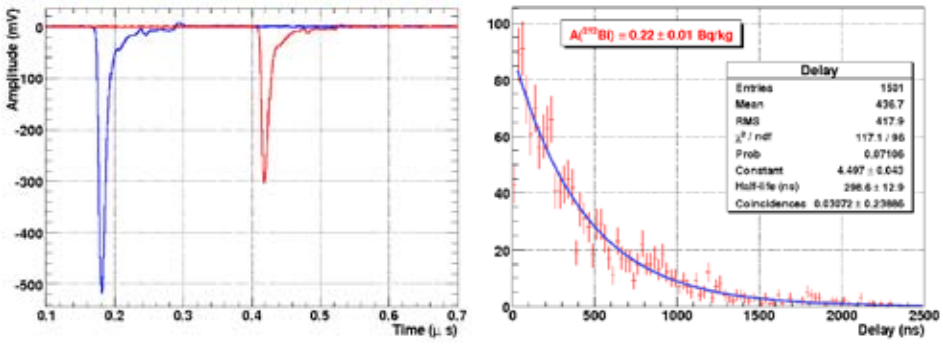


Figure 5: Example of a BiPo event observed in BiPo1 and delay distribution between the $\beta$ and the $\alpha$ decays.

Particle identification in the plastic scintillator could help to sign the BiPo process and reject random coincidences of $\gamma$. Indeed, longer half-life states in scintillators are excited by $\alpha$ particles

but not by electrons. More light is therefore observable in the tail of the pulse for $\alpha$ particles. A pulse shape discrimination, using tail-to-total charge ratio as discrimination factor, has been applied on the photomultiplier signals from the data of the calibration foil. A good separation has been observed for prompt ($e^-$) and delayed ($\alpha$) signals (Fig. 6). Using this discrimination, it is possible to reject 80 % of the random coincidence background and to keep 90 % of the true BiPo events.

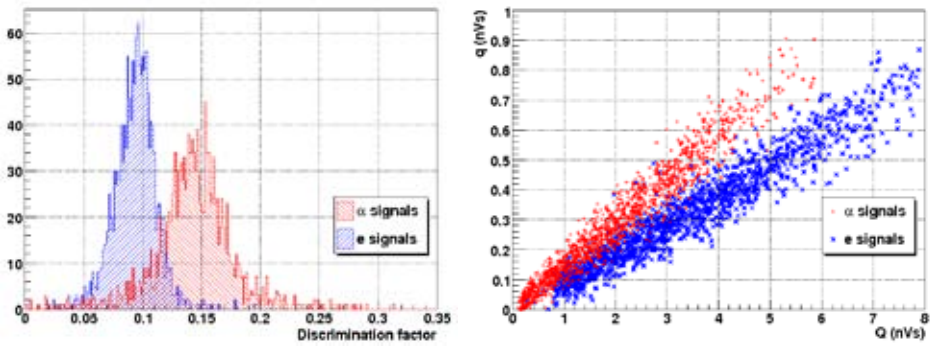


Figure 6: Distributions of the tail-to-total charge ratio and the tail charge $q$ as a function of the total charge $Q$ for the prompt and delayed signal from the aluminum foil in the first module of BiPo1.

## 5 BiPo1 surface radiopurity

The other modules of BiPo1 are dedicated to the measurement of the surface radiopurity of scintillators. BiPo events, coming from the contact surface between the two scintillators, are observed by a hit in one scintillator and a delayed hit in the other one. After 2 months of data taking, 7 BiPo events have been observed on a statistics equivalent to 0.8 $m^2 \times$month. It corresponds to an activity of about 2 $\mu$Bq/$m^2$. Extrapolating this background to a final 10 $m^2$ BiPo detector for a one month measurement of 4 kg selenium source foil for SuperNEMO, the thallium preliminary sensitivity is: $\mathcal{A}(^{208}\mathrm{Tl}) < 7.5$ $\mu$Bq/kg (90% C.L.).

## 6 Conclusion

The BiPo1 prototype demonstrated the validity of the experimental technique to measure $^{208}$Tl contaminations in thin materials. The preliminary sensitivity achieved is 10 times better than standard HPGe measurements. Particles identification with simple plastic scintillators enhance the performances of the prototype. New modules using "phoswich" scintillators, a compound of a thin fast scintillator to detect $\alpha$ and a thick slow scintillator for electrons, will improve the discrimination between the 2 particles. A second prototype, BiPo2, using large scintillator plates (0.56 $m^2$) will also be tested in LSM before this summer.

## References

1. L. Simard, Status of the SuperNEMO Project, Workshop on calculation of double-beta decay matrix elements, Prague, Czech Republic, 2007
2. M. Bongrand, The BiPo Detector for Ultralow Radioactivity Measurements, Topical Workshop on low radioactivity Techniques, LRT 2006, Aussois, France, 2006, arXiv:physics/0702070v1
3. D. Breton, E. Delagnes and M. Houry, Very high dynamic range and high sampling rate VME digitizing boards for physics experiments, Nuclear Science, IEEE Transactions on Volume 52, Issue 6, Dec. 2005 Page(s): 2853 - 2860

# SEARCH FOR THE STANDARD MODEL HIGGS BOSON IN THE $HZ \to b\bar{b}\nu\bar{\nu}$ CHANNEL AT DØ

CHRISTOPHE OCHANDO
*Laboratoire de l'Accélérateur Linéaire,*
*IN2P3-CNRS, Université Paris-Sud XI,*
*Bâtiment 200, 91898 Orsay Cedex, France.*

A search for the standard model Higgs boson has been performed in 2.1 fb$^{-1}$ of $p\bar{p}$ collisions at 1.96 TeV, collected with the DØ detector at the Fermilab Tevatron. The final state considered is a pair of $b$ jets with large missing transverse energy, as expected from the reaction $p\bar{p} \to HZ \to b\bar{b}\nu\bar{\nu}$. The search is also sensitive to the $HW \to b\bar{b}\ell\nu$ channel, when the charged lepton is not identified. Boosted decision trees were used to discriminate the signal from the backgrounds, dominated by $Wbb$ and $Zbb$ final states. For a Higgs boson mass of 115 GeV, a limit has been set at 95% C.L. on the cross section times branching fraction of $(p\bar{p} \to H(Z/W)) \times (H \to b\bar{b})$, which is 7.5 times larger than the standard model value.

## 1 Introduction

The $p\bar{p} \to HZ$ reaction, with $H \to b\bar{b}$ and $Z \to \nu\bar{\nu}$, is among the most promising for the discovery of a low mass Higgs boson at the Fermilab Tevatron [1]. A search with 2.1fb$^{-1}$ of data collected with the DØ detector is presentend here. A lower mass limit of 114.4 GeV was set by the LEP experiments for the Higgs boson from analyses of the reaction $e^+e^- \to HZ$ [2], while an upper limit of 144 GeV can be inferred from precision electroweak data [3]. Here and in the following, all limits quoted are at the 95% confidence level.

The final state topology considered in this analysis is a pair of $b$ jets from the decay of the Higgs boson, with missing transverse energy ($\not\!\!E_T$) due to the neutrinos from the $Z$ decay. The search is therefore also sensitive to the $HW$ channel, with $W \to \ell\nu$ when the charged lepton from the $W$ decay is not detected. The main backgrounds arise from $(W/Z)$+ jets, from top quark and diboson production and from multijet events produced by the strong interaction, with fake $\not\!\!E_T$ resulting from fluctuations in jet energy measurements and with real $b$ or mistagged light parton jets.

A kinematic selection is first applied to reject most of the multijet events. The two jets expected from the Higgs boson decay are next required to be tagged as $b$ jets, using a neural network $b$-tagging algorithm. Finally, discrimination between the signal and the remaining backgrounds is achieved by means of a boosted decision tree technique.

## 2 Data and Simulated samples

For this analysis, the data were recorded using a set of triggers designed to select events with jets and missing transverse energy. As the trigger conditions are not included into the full simulation, the calibration of the trigger response was performed on Z$\rightarrow \mu^+\mu^-$+jets events. Due to the muons which only deposit energy in the calorimeter at the minimum of ionization, these events have the same topology as the signal. Except for the background from multijet production, which was estimated from data, all backgrounds from the standard model (SM) were determined by Monte Carlo simulation.

## 3 Event Selection

### *3.1 Pre-Tagging Selection*

At this stage, most of the cuts are applied to specifically reject the multijet background. The selected events are required to have:

- exactly 2 or 3 jets with $p_T > 20$ GeV and within $|\eta_{\rm det}| < 2.5$ [a]
- $\Delta\phi(\text{jet}_1, \text{jet}_2) < 165^\circ$ to avoid back-to-back jets in the plane transverse to the beam direction.
- $\not\!\!E_T > 50$ GeV. This criterion is tightened in case the direction of the missing $E_T$ is close to the direction of one of the jets in the transverse plane: $\not\!\!E_T(\text{GeV}) > 80 - 40 \times \min\Delta\phi(\not\!\!E_T, \text{any jet})$, where the angle is measured in radians.
- The asymmetry $\mathcal{A} = (\not\!\!E_{T'} - \not\!\!H_{T'})/(\not\!\!E_{T'} + \not\!\!H_{T'})$, where $\not\!\!H_{T'} = |-\Sigma\overrightarrow{p}_{T\text{jet}}|$, is required to lie between $-0.1$ and 0.2.
- In signal events, the missing track-$p_T$, $\not\!\!p_T$, defined as the opposite of the vectorial sum of the charged particle transverse momenta, is expected to point in a direction similar to that of the $\not\!\!E_T$. Advantage is taken of this feature by requiring $\Delta\phi(\not\!\!E_T, \not\!\!p_T) < \pi/2$.

To reject backgrounds from $W$+jets, top, and diboson production, events containing an isolated electron or muon are rejected.

### *3.2 Heavy-Flavor Tagging*

Advantage is next taken of the large branching fraction for $H \rightarrow b\bar{b}$ by requiring the two leading jets to be $b$-tagged.

As can be seen in Fig. 1 for the invariant mass of the dijet system built from the two leading jets, the simulation provides a good description of the data both before (40 340 events expected and observed) and after (439 events observed and 442.8$\pm$1.1 expected) $b$-tagging. After $b$-tagging, the $W$+jets and $Z$+jets backgrounds are dominated by heavy flavor jet production, which contributes $\mathcal{O}(90\%)$.

## 4 Discriminant Analysis

In order to take full advantage of the different kinematic characteristics of the signal and background processes, a boosted decision tree (DT) technique [7] was used. A dedicated DT was trained for each of the Higgs boson masses probed and for each of the two data taking periods (these are Run IIa and Run IIb with different in experimental conditions).

The DT discriminants are shown in Fig. 2 for a Higgs boson mass of 115 GeV.

[a] $\eta_{\rm det}$ is the pseudorapidity measured from the detector center.

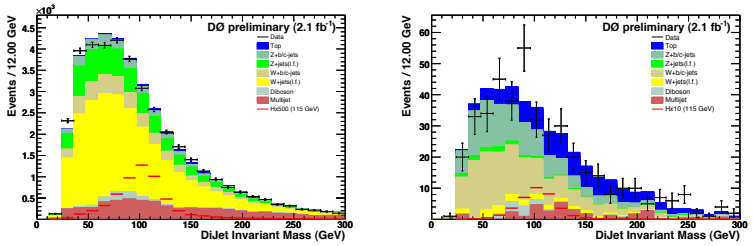


Figure 1: Distributions of the invariant mass of the two leading jets before (left) and after $b$-tagging (right). The data are shown as points with error bars. The various background contributions (SM and multijet) are shown as histograms, with color codes as indicated in the frames. Distributions for a signal with a Higgs boson mass of 115 GeV are also shown, multiplied by 500 before and by 10 after $b$-tagging.

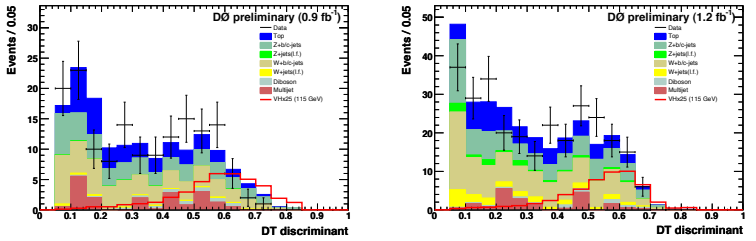


Figure 2: Distributions of the decision tree discriminants for a Higgs boson mass of 115 GeV ($HZ$ and $HW$ signals combined) for Run IIa (left) and Run IIb (right). The data are shown as points with error bars. The various background contributions (SM and multijet) are shown as histograms, with color codes as indicated in the frames. The distributions for the signal are multiplied by a factor of 25.

## 5 Systematic Uncertainties

Systematic uncertainties originate from various sources. Experimental uncertainties arise from the trigger simulation (5.5%), from the jet energy calibration (from 2% to 3%), resolution (about 1%), and reconstruction efficiency (2%), and from $b$-tagging (about 6%). Furthermore, a 6% error is assigned to the luminosity determination.

Moreover, the cross sections of the various SM and signal processes suffer from theoretical uncertainties. They were found to be at a level of 6 to 16%. They were estimated from MCFM [4] or from Refs. [5] and Ref. [6]. Finally, uncertainties on the heavy flavor fractions of W/Z+jets background(50%) are quoted.

## 6 Results

Agreement between data and expectation from SM and multijet backgrounds is observed both in terms of numbers of events selected and of DT discriminant shapes (Fig. 2). To set limits, based on the DT output, on the SM Higgs boson production cross section, a modified frequentist approach [8] was used.

The results obtained are shown as a function of the Higgs boson mass in Fig. 3 and in Table 1, in terms of the ratio of the excluded cross section times branching fraction for $H \to b\bar{b}$ to the SM Higgs prediction. The LLRs (Log Likelihood Ratios) are also shown in Fig. 3. For a 115 GeV Higgs boson mass, the observed and expected limits on the cross section of combined $HZ$ and $HW$ production times branching fraction for $H \to b\bar{b}$ are 7.5 and 8.4 times larger than the SM value, respectively.

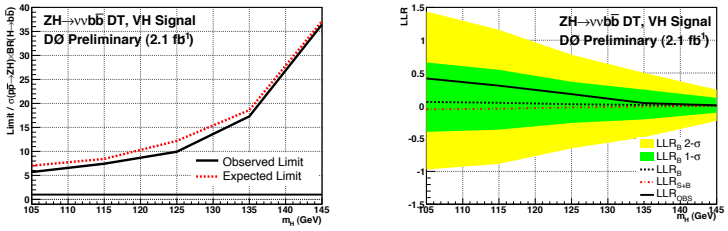


Figure 3: As a function of the Higgs boson mass, limit on the cross section of combined $HZ$ and $HW$ production times branching fraction for $H \to b\bar{b}$ (left), relative to the SM value, and log likelihood ratio (right). On the right, the observed and expected limits are shown as solid and dashed curves, respectively. On the left, the observed LLR is shown as a solid curve, the expected LLRs are shown as black and red dashed curves for the background-only and signal+background hypotheses, respectively, and the green and yellow areas correspond to the one and two $\sigma$ deviations around the expected background-only LLR.

| Mass (GeV) | 105 | 115 | 125 | 135 | 145 |
|---|---|---|---|---|---|
| Observed | 5.7 | 7.5 | 9.9 | 17.3 | 36.4 |
| Expected | 7.0 | 8.4 | 12.2 | 18.6 | 37.1 |

Table 1: For various Higgs boson masses, observed and expected ratios of excluded to SM production cross sections times branching fraction for $H \to b\bar{b}$.

## 7 Summary

A search for the SM Higgs boson has been performed in 2.1 fb$^{-1}$ of $p\bar{p}$ collisions at 1.96 TeV. The topology analysed consists of a pair of $b$ jets with large $\not\!\!E_T$, as expected from $p\bar{p} \to HZ \to b\bar{b}\nu\bar{\nu}$. The search is also sensitive to $HW$ production, where the $W$ decays leptonically and the charged lepton is undetected. No deviation from the expectation from SM backgrounds was observed. A boosted decision tree technique was used to derive an upper limit on the cross section of the $p\bar{p} \to HZ$ and $p\bar{p} \to HW$ processes combined, as a function of the Higgs boson mass. For a mass of 115 GeV, this limit is a factor 7.5 larger than the SM cross section.

## References


1. M. Carena *et al.*, *"Report of the Tevatron Higgs Working Group"*, arXiv:hep-ph/0010338; CDF and DØ Collaborations, *"Results of the Tevatron Higgs Sensitivity Study"*, FERMILAB-PUB-03/320-E.
2. R. Barate *et al.* [LEP Working Group for Higgs boson searches], Phys. Lett. B **565**, 61 (2003).
3. The LEP Collaborations: ALEPH Collaboration, DELPHI Collaboration, L3 Collaboration, OPAL Collaboration, the LEP Electroweak Working Group, *"Precision Electroweak Measurements and Constraints on the Standard Model,"* CERN-PH-EP/2007-039, arXiv:0712.0929v2.
4. J.M. Campbell and R.K. Ellis, Phys. Rev. D **60**, 113006 (1999).
5. M. Cacciari *et al.*, JHEP **404**, 068 (2004); N. Kidonakis and R. Vogt, Phys. Rev. D **68**, 114014 (2003); N. Kidonakis, Phys. Rev. D **74**, 114012 (2006).
6. S. Catani *et al.*, JHEP **0307**, 028 (2003).
7. L. Breiman *et al.*, *"Classification and Regression Trees"*, Wadsworth (1984); Y. Freund and R.E. Schapire, *"Experiments with a new boosting algorithm"*, in Machine Learning: Proceedings of the Thirteenth International Conference, pp. 148-156 (1996);
8. T. Junk, Nucl. Instrum. Methods in Phys. Res. A **434**, 435 (1999); A. Read, in *"1st Workshop on Confidence Limits,"* CERN Report No. CERN-2000-005, 2000.

# Search for SM Higgs in the $WH \to l\nu b\bar{b}$ Channel using $\sim$2fb$^{-1}$

**Tatsuya Masubuchi** on behalf of the CDF Collaboration
*Doctoral Program in Physics, Graduate School of Pure and Applied Sciences,*
*University of Tsukuba,*
*Ten'noudai 1-1-1, Tsukuba, Ibaraki 305-8571, Japan*

We report a search for Standard Model (SM) Higgs boson production in association with a $W^{\pm}$ boson. This search uses data corresponding to an integrated luminosity of 1.9 fb$^{-1}$ collected with the CDF detector at Tevatron. We select events matching the $W$ + jets signature and require at least one jets to be identified as $b$-quark jets. To further increase discrimination between signal and background, we use kinematic information in an artificial neural network. The number of tagged events and the resulting neural network output distributions are consistent with the Standard Model expectations, and we set an upper limit on the $WH$ production cross section times branching ratio $\sigma(p\bar{p} \to W^{\pm}H) \times BR(H \to b\bar{b}) < 1.1$ to 1.0 pb for Higgs masses from 110 GeV/$c^2$ to 150 GeV/$c^2$ at 95% confidence level.

## 1 Introduction

The success of the Standard Model in explaining and predicting experimental data provides strong motivation for the existence of a neutral Higgs boson. Current electroweak fits combined with direct searches from LEP2 indicate the mass of the Higgs boson is less than 190 GeV/$c^2$ at 95% confidence level [1]. In proton-antiproton collisions of $\sqrt{s} = 1.96$ TeV at the Tevatron, the Standard Model Higgs boson may be produced in association with a $W$ boson [2]. For low Higgs masses (below 140 GeV/$c^2$) the dominant decay mode is $H \to b\bar{b}$. The final state from the $WH$ production is therefore $\ell\nu b\bar{b}$, where the high-$p_T$ lepton from the $W$ decay provides an ideal trigger signature at CDF. The analysis strategies make use of $b$-tagging algorithm to suppress the $W$+jets backgrounds and apply artificial neural network to discriminate signal to remaining backgrounds.

## 2 Event Selection

Events are collected by the CDF II detector with high-$p_T$ central electron or muon triggers which have an 18 GeV threshold. The central electron or muon is further required to be isolated with $E_T$ (or $p_T$) $> 20\,\mathrm{GeV}$ in offline. Events having the $W$+jets signature are confirmed with a missing transverse energy requirement ($\not\!\!E_T > 20\,\mathrm{GeV}$).

We use forward (plug) electron events with a trigger intended for $W$ candidate events. This trigger requires both a forward electron candidate and missing transverse energy. Plug electron events are further required to have $E_T > 20$ GeV and $\not\!\!E_T > 25$ GeV. For plug electron events, additional selection is required to suppress QCD background.

Events are required to have 2 jets with $E_T > 20\,\mathrm{GeV}$ and $|\eta| < 2.0$. Because the Higgs boson decays to $b\bar{b}$ pairs, we employ $b$-tagging algorithms which relies on the long lifetime and large mass of the $b$ quark to suppress enormous $W$+jets backgrounds.

### *2.1 Bottom Quark Tagging Algorithm*

To greatly reduce the backgrounds to this Higgs search, we require that at least one jets in the event be identified as containing $b$-quarks by one of three $b$-tagging algorithms. The secondary vertex tagging algorithm identifies $b$ quarks by fitting tracks displaced from the primary vertex. In addition, we add jet probability tagging algorithm that identifies $b$ quarks by requiring a low probability that all tracks contained in a jet originated from the primary vertex, based on the track impact parameters [3]. To be considered for double tag category, an event is required to have either two secondary vertex tags, or one secondary vertex tag and one jet probability tag.

Furthermore we also make use of exactly one $b$-tagged events with the secondary vertex tagging algorithm. To improve signal-to-background ratio for one tag events, we employ neural network (NN) $b$-tagging algorithm [4] applied. This neural network is tuned for only jets tagged by the secondary vertex tagging algorithm. The purity of $b$-jets tagged by this algorithm is improved.

Finally we categorize events in three $b$-tagged conditions, double secondary vertex tagged events, one secondary vertex tagged plus one jet probability tagged events and one NN tagged events. These two categories of double-tagged events and one category of one neural network tagged events are defined exclusively.

### *2.2 Expected Signal Events and Systematics*

The acceptance in Higgs mass of $120\,\mathrm{GeV}/c^2$ in central region is 0.48±0.05%, 0.38±0.04%, 0.93±0.05% for the double secondary vertex tagged, the secondary vertex plus jet probability and one neural network tagged category, respectively. The expected signal events in Higgs mass 120 GeV/c$^2$ are about 3.9 events in central plus plug data.

The uncertainties on the signal acceptance currently have the largest effect on the Higgs sensitivity. The $b$-tagging uncertainty is dominated by the uncertainty on the data/MC scale factor. 3.5-9.1% systematic is assigned for each $b$-tagging category. The uncertainties due to initial state radiation and final state radiation (2.9-5.2%) are estimated as difference from the nominal. Other uncertainties on parton distribution functions ($\sim$ 2%), jet energy scale (2-3%), trigger efficiencies ($<$ 1%) and lepton identification contribute (2%) are taken into account.

## 3 Backgrounds

This analysis builds on the method of background estimation detailed in Ref. [4]. In particular, the contributions from the following individual backgrounds are calculated: falsely $b$-tagged events,

$W$ production with heavy flavor quark pairs, QCD events with false $W$ signatures, top quark pair production, and electroweak production (diboson, single top).

We estimate the number of falsely $b$-tagged events (mistags) by counting the number of negatively-tagged events, that is, events in which the measured displacement of the secondary vertex is opposite the $b$ jet direction. Such negative tags are due to tracking resolution limitations, but they provide a reasonable estimate of the number of false positive tags after a correction for material interactions and long-lived light flavor particles.

The number of events from $W$ + heavy flavor is calculated using information from both data and Monte Carlo programs. We calculate the fraction of $W$ events with associated heavy flavor production in the ALPGEN Monte Carlo program interfaced with the PYTHIA parton shower code. This fraction and the $b$-tagging efficiency for such events are applied to the number of events in the original $W$+jets sample after correcting for the $t\bar{t}$ and electroweak contributions.

We constrain the number of QCD events with false $W$ signatures by assuming the lepton isolation is independent of $\not\!\!E_T$ and measuring the ratio of isolated to non-isolated leptons in a $\not\!\!E_T$ sideband region. The result in the tagged sample can be calculated in two ways: by applying the method directly to the tagged sample, or by estimating the number of non-W QCD events in the pretag sample and applying an average $b$-tagging rate.

In this analysis, 83, 90 and 805 events for each $b$-tagging category are observed against 80.62±18.75, 86.99±17.99 and 809.61±159.38 expected in signal region. The good agreement is also obtained in plug region.

## 4 Artificial Neural Network

To further improve signal to background separation we employ an artificial neural network. This neural network combines six kinematic variables into a single function with better discrimination between the Higgs signal and the background processes than any of the variables individually. To train the neural network, JETNET package [5]. The input variables are defined below:

**Dijet invariant mass+:** The invariant mass reconstructed from the two jets. If there are additional looser jets, the loose jet that is closest to one of the two jets is included in this invariant mass calculation.

**Total System $p_T$:** The vector sum of the transverse momenta of the lepton, the $\not\!\!E_T$, and the two jets.

$p_T$ **Imbalance:** The scalar sum of the lepton and jet transverse momenta minus the $\not\!\!E_T$.

$\sum E_T$ **(loose jets):** The scalar sum of the loose jet transverse energy.

$M_{l\nu j}^{min}$**:** The invariant mass of the lepton, $\not\!\!E_T$and one of the two jets, where the jet is chosen to give the minimum invariant mass. The $p_z$ of neutrino is ignored for this quantity.

$\Delta R$ **(lepton-$\nu$):** The distance between the direction of lepton and neutrino in $\eta - \phi$ plane, where the $p_z$ of the neutrino is taken from largest $|p_z|$ calculated from $W$ mass constraint.

The training is defined such that the neural network attempts to produce an output as close to 1.0 as possible for Higgs signal events and as close to 0.0 as possible for background events. For optimal sensitivity, a different neural network is trained for each Higgs mass considered. Fig.1 show the neural network results for each $b$-tagging category.

## 5 Results

We perform a direct search for an excess in the signal region of the neural network output distribution from single-tagged and double-tagged $W$+2 jet events. A binned maximum likelihood technique is used to estimate upper limits on Higgs production by constraining the number

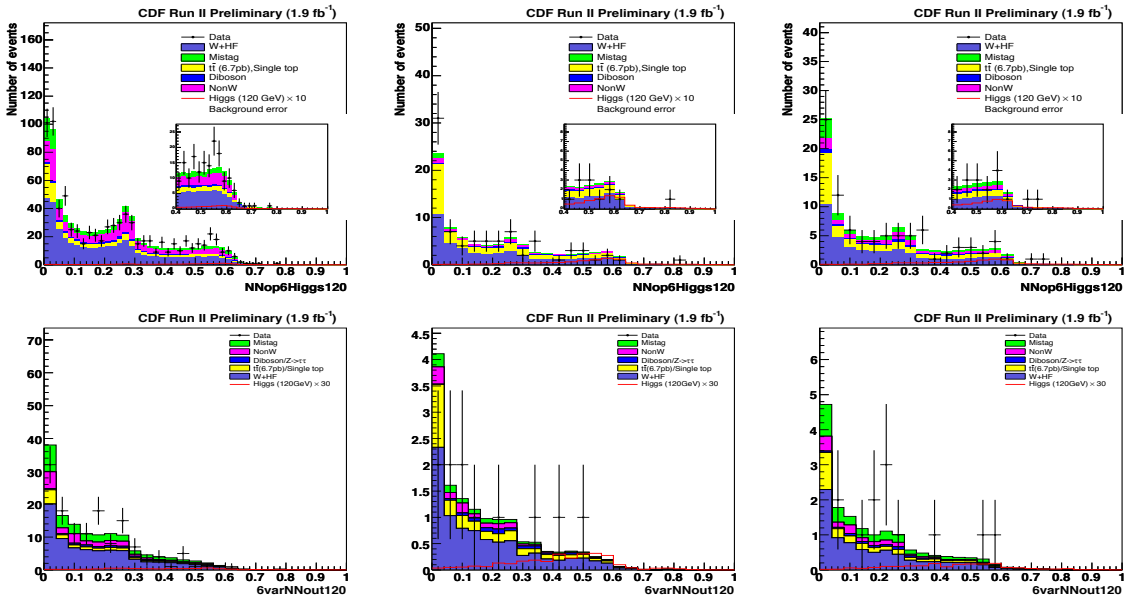


Figure 1: Neural network results calculated from six variables for each lepton region (Top:central lepton, Bottom: plug electron). The plot on the left shows exactly one $b$-tagged events, the plots on the center and right show double secondary vertex $b$-tagged event and one secondary vertex plus one jet probability $b$-tagged events, respectively.

of backgrounds to the estimates within uncertainties. Each $b$-tagging category is combined to obtain best sensitivity for both central and forward lepton region. We set an upper limit on the production cross section times branching ratio as a function of $m_H$, plotted in Fig. 2. The results are also collected in Table 3.

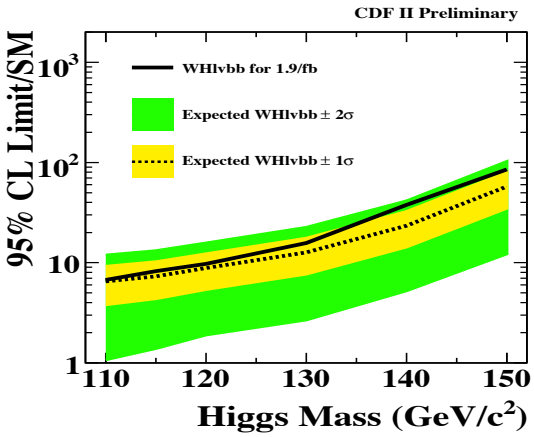


Figure 2: Observed and expected limits as a function of the Higgs mass hypothesis. The solid line shows observed 95% C.L. upper limit and dash line shows expected limit obtained by the assumption of null signal hypothesis.

| Higgs Mass ($GeV/c^2$) | Upper Limit (pb) / (pb/SM) | |
|---|---|---|
| | Observed | Expected |
| 110 | 1.1 (6.8) | 1.1 (6.5) |
| 115 | 1.1 (8.2) | 1.0 (7.3) |
| 120 | 1.1 (9.8) | 1.0 (8.9) |
| 130 | 1.0 (15.8) | 1.0 (12.6) |
| 140 | 1.2 (37.8) | 0.7 (23.4) |
| 150 | 1.0 (85.2) | 0.7 (57.6) |

Figure 3: Observed and expected 95% C.L. upper limit on $\sigma(p\bar{p} \to WH) \times (\mathrm{BR}(H \to b\bar{b})$. The numbers in parenthesis show the values normalized by the Standard Model theoretical cross section.

## References


1. LEP electroweak working group, http://lepewwg.web.cern.ch/LEPEWWG/.
2. TeV4LHC Higgs working group, http://maltoni.home.cern.ch/maltoni/TeV4LHC/SM.html.
3. D. Buskulic, *et al.* (ALEPH Collaboration), Phys. Lett. B **313**, 535 (1993).
4. The CDF Collaboration, *Phys. Rev. Lett.* **100**, 041801 (2008).
5. L. Lönnblad, C. Peterson, and T. Rögnvaldsson, Comp. Phys. Comm. 81 (1994) 185.

# STUDY OF VECTOR BOSON FUSION HIGGS IN ATLAS-LHC

D. VAROUCHAS
*LAL, Univ Paris-Sud, IN2P3/CNRS, Orsay, France*

Within the framework of Standard Model, the production mode of Higgs boson through the fusion of the vector bosons $W$ or $Z$ (*Vector Boson Fusion*) is one of the most important production mechanisms, providing a specific detection signature. A detailed study regarding this issue is being undergone for ATLAS detector in LHC and some general features of this analysis are being presented in this note emphasizing in the study of Central Jet Veto.

## 1 VBF Topology and its characteristics

The four different production mechanisms of a Standard Model Higgs boson [1] at the LHC are (Fig.1b): the $gg$ fusion, the Vector Boson Fusion, the Higgs boson production associated with vector bosons $W$ or $Z$ and the Higgs boson production associated with the production of a $t\bar{t}$ pair. Although VBF cross section is one order of magnitude lower than the dominant one of $gg$ fusion (Fig.1a), its topological characteristics provide a signature which makes it an important discovery channel for a low mass Higgs boson.

As it is illustrated in Fig.1b the VBF[a] Higgs (or $WZ$ Fusion) occurs when two quarks originating from the proton beam are being scattered through the exchange of a $W$ or $Z$ boson and their fusion produces the Higgs boson. The important aspect of this topology is the fact the two scattered quarks give two energetic jets highly separated in rapidity in the forward regions of the detector.

Because of the electroweak character of the VBF Higgs boson production ($W, Z$ colorless exchange), a low gluon radiation activity is expected which is translated in detection terms as a low jet activity. Consequently, no jets are expected in the central region of the detector above a certain $p_T$ limit, in addition to the Higgs boson decay products. This aspect is motivating a central jet veto: the event is rejected if a third jet is detected in the central region above a given threshold of $p_T$. This cut is efficient against the main backgrounds and especially against $t\bar{t}$ and can be a useful tool to the improvement of the S Vs B separation.

[a] Vector Boson Fusion

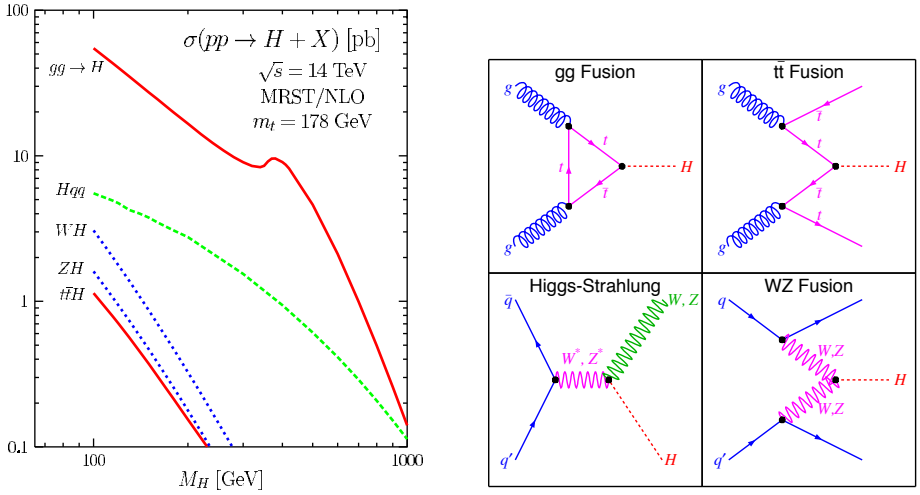


Figure 1: (a) Cross Section of Higgs boson for (b) the four different production mechanisms in LHC, within the frame of Standard Model.

## 2 VBF $H \to \tau^+\tau^-$ in ATLAS

The most promissing part of the VBF Higgs analysis is the one which studies its decay into a pair of $\tau^+\tau^-$ leptons. This channel was first studied in ref.[2] for ATLAS [3] and now, a more detailed study is being undergone using state of the art Monte Carlo generators and a fully detailed simulation of the detector.

Due to the weak branching ratio of Higgs boson decaying to $\tau^+\tau^-$ for masses $m_h > 140GeV/c^2$, the analysis is performed in the mass range of $110GeV/c^2 < m_h < 140GeV/c^2$ and it is divided into three different categories depending on the decays of $\tau$ leptons (leptonic or hadronic decay). As a consequence, three sub-channels are obtained at the end: The lepton-lepton channel with a B.R. $\simeq$ 12 %, the lepton-hadron channel with a B.R. $\simeq$ 46 % and the hadron-hadron channel with a B.R. $\simeq$ 42 %.

For the processes of background the generated events correspond to:

- $Z \to \tau^+\tau^- + jets$
- $t\bar{t}$
- $W^{\pm} + jets$

Among them the dominant background is the $Z \to \tau^+\tau^- + jets$ which has a quite similar topology with the signal and therefore is the most difficult to suppress.

The final goal is to reconstruct the invariant mass of the couple $\tau^+\tau^-$ which equals to the mass of Higgs boson. The existence of at least two neutrinos in the event, requires the use of a collinear approximation to estimate the $m_{\tau^+\tau^-}$ invariant mass from the measure of the missing $p_T$ vector and the $p_T$ of the visible tau decay products. This approximation implies that the tau decay products are collinear to the direction of taus. This is an acceptable assumption considering the hig Pt of the $\tau$ leptons. However it provides a good mass resolution only if the tau decay products are not back to back, which is the case if the parent Higgs boson has reasonably high Pt.

The first step of the analysis consists of the identification of leptons and hadrons following the general ATLAS methods. Then, several cuts are applied in order to separate background from signal. This cuts can be categorized in three groups. The first group is related to the tau decay and different constraints concerning the kinematic variables of leptons or jets originating from

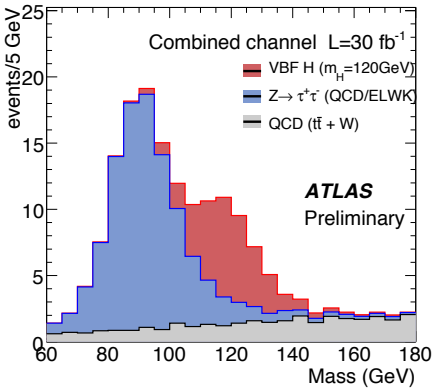


Figure 2: The reconstructed $\tau^+\tau^-$ invariant mass for a VBF Higgs boson signal of $120 GeV/c^2$ in the combined lepton-lepton and lepton-hadron channel above all backgrounds after application of all cuts. The number of signal and background events is shown for an integrated luminosity of $30 fb^{-1}$.

the hadronic decay of tau are being applied. These cuts differ in lepton-lepton, lepton-hadron and hadron-hadron cases. Next, the following set of cuts is based on collinear approximation method used for the mass reconstruction and finally, several constraints deriving from the special jet VBF behavior described in the previous paragraph are being applied such as, a given $p_T$ threshold for the two forward jets, a large separation in $\eta$, the decay products to lie between the forward jets in $\eta$, high invariant mass of the two forward jets and also a central jet veto.

At Fig.2 we see the mass distribution after having applied all the different cuts. It is obvious that the $Z \rightarrow \tau^+\tau^-$ is the dominant background as expected, but still there is a clear peak related to the mass of Higgs boson. Nevertheless, the importance of the mass resolution is highlighted through this plot, which shows that a worse resolution would result to a contamination of the signal by the $Z$ resonance.

## 3 Central Jet Veto

Jets play an important role in this channel and therefore, many studies have been done towards this issue. In this analysis, the jets are reconstructed with a cone algorithm of a radius of 0.4 and part of these jet studies related to VBF Higgs topology, is the optimization of the central jet veto cut. This cut rejects an event if a third jet is found in a region of $|\eta| < 3.2$ having a $p_T > 20 GeV/c$. Other alternatives of this cut are also studied by changing this $|\eta|$ region. A jet veto was studied without applying any constraints on $\eta$ and also applying the cut if a third jet is only found between the two forward jets in $\eta$. Another interesting feature seen, was that in many cases of signal events rejected by this cut, the vetoing jet was very close in $\Delta R$ [b] to one of the two forward jets. This was due to the splitting of the initial jet originating from the scattered parton. Using a larger jet reconstruction cone, such as 0.7 for instance which is the other alternative in ATLAS algorithms, the jet splitting effect might have been reduced but the overall signal significance would still be lower. Therefore, a better option is to introduce an additional constraint, which is to not take into consideration the third jet if it is close to one of the forward jets, and more precisely, if $\Delta R$ between these two jets is less than 1. In order to compare the three different approaches the cut efficiency is calculated for Signal and Background. The results are shown in Fig.3.

With the combination of the $\Delta R$ condition to eliminate the vetoing jets close to the forward jets and searching for a third jet between the two forwards jets in terms of $\eta$, a gain of $\sim$10%

[b] $\Delta R = \sqrt{\Delta\eta^2 + \Delta\phi^2}$

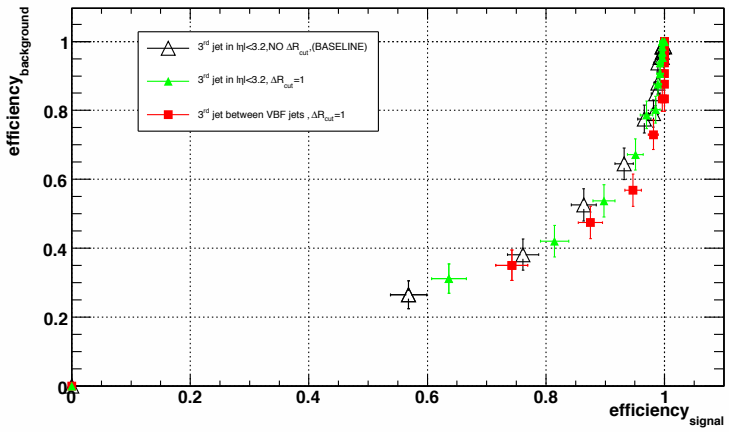


Figure 3: Jet veto cut efficiency for signal and background. The white triangles represent the primary jet veto method where no $\Delta R$ cut is applied and the third jet is searched in $|\eta| < 3.2$ . The green triangles represent the primary jet veto method but searching the third jet only between the two forward jets in term of $\eta$ and finally, the red squares represent the previous jet veto method having applied the $\Delta R$ cut as well. Every point in all curves corresponds to the efficiencies of a given $p_T$ threshold of the third jet starting from $10GeV/c$ with a step of $5GeV/c$.

for the signal jet veto cut efficiency is achieved, as it is seen in Fig.3.

## 4 Outlook

The main characteristics of VBF Higgs boson topology and some general aspects of the analysis of its decay in a couple of $\tau^+\tau^-$ in ATLAS were presented. An example of improving a cut efficiency was addressed and it was shown that a gain of 10 % is accomplished modifying the jet veto cut. This analysis is not yet finalized since many studies are still being undergone, in particular concerning the effect of $pile - up$, which causes the creation of more jets into both signal and background events for the high LHC luminosities. Nevertheless, it was shown that VBF Higgs boson is one of the most promising channels for a low mass Higgs boson.

## References

1. A. Djouadi, "The anatomy of electro-weak symmetry breaking" arXiv:hep-ph/0503173
2. Asai and al., Eur. Phys. J. C **32S2** (2004) 19 [arXiv:hep-ph/0402254]
3. ATLAS Collaboration, Detector and physics performance technical design report (volume ii) CERN-LHCC/99-15 (1999)

# Yukawa corrections to Higgs production associated with two bottom quarks at the LHC

Le Duc Ninh
*LAPTH, Université de Savoie, CNRS; BP 110, F-74941 Annecy-le-Vieux Cedex, France*

We investigate the leading one-loop Yukawa corrections to the process $pp \to b\bar{b}H$ in the Standard Model. We find that the next-to-leading order correction to the cross section is small about $-4\%$ if the Higgs mass is 120GeV. However, the appearance of leading Landau singularity when $M_H \geq 2M_W$ can lead to a large correction at the next-to-next-to-leading order level for a Higgs mass around 160GeV.

## 1 Introduction

The cross section for $b\bar{b}H$ production at the LHC is very small compared to the gluon fusion channel. However, it is important to study that because of the following reasons:

- It can provide a direct measurement of the bottom-Higgs Yukawa coupling ($\lambda_{bbH}$) which can be strongly enhanced in the MSSM.
- We can identify the final state in experiment by tagging b-jets with high $p_T$. This reduces greatly the QCD background.
- Theoretically, it is a $2 \to 3$ process at the LHC which is a good example of one-loop multi-leg calculations. Moreover, the process $gg \to b\bar{b}H$ is, to the best of our knowledge, the most beautiful example where the leading Landau singularity (LLS) occurs in an electroweak box Feynman diagram. Considering that one rarely encounters such a singularity, studying its effect is very important.

The next-to-leading order (NLO) QCD correction to the exclusive process $pp \to b\bar{b}H$ with high $p_T$ bottom quarks has been calculated by two groups [1]. The QCD correction is about $-22\%$ for $M_H = 120$GeV and $\mu = M_Z$ (renormalisation/factorisation scale). No leading Landau singularity occurs in any QCD one-loop diagrams.

The aim of our work is to calculate the Yukawa corrections, which are the leading electroweak corrections in this case, to the exclusive $bbH$ final state with high $p_T$ bottom quarks at the LHC [2]. These corrections are triggered by top-charged Goldstone loops whereby, in effect, an external $b$ quark turns into a top quark. Such type of transitions can even trigger $gg \to b\bar{b}H$ even with vanishing $\lambda_{bbH}$, in which case the process is generated solely at one-loop level.

## 2 Calculation and results

At the LHC, the entirely dominant contribution comes from the sub-process $gg \to b\bar{b}H$. The contribution from the light quarks in the initial state is therefore neglected in our calculation.

Typical Feynman diagrams at the tree and one-loop levels are shown in Fig. 1. All the relevant

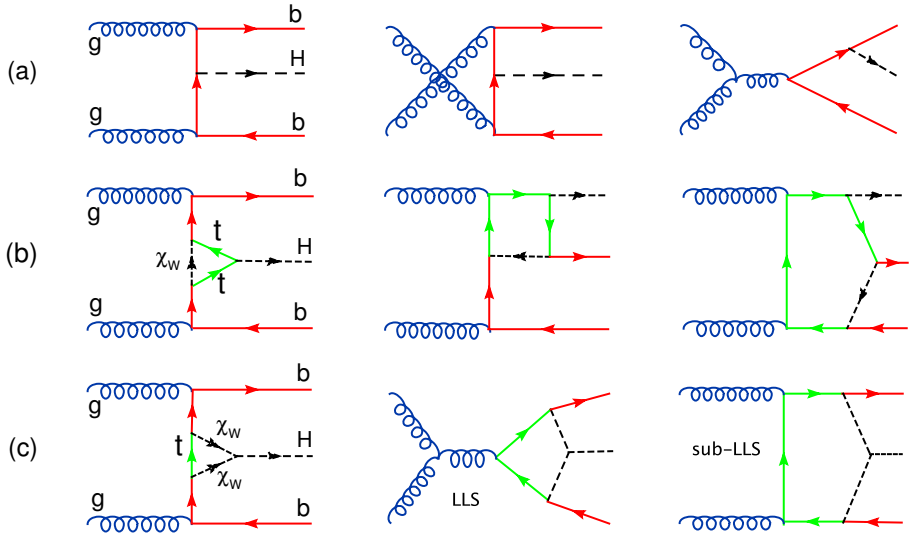


Figure 1: *Typical Feynman diagrams for the process* $gg \to b\bar{b}H$ *at tree [class (a)] and one-loop [classes (b) and (c)] levels. Loop particles are the charged Goldstone bosons* ($\chi_W$) *and the top quark. In the class (c): the box diagram has a LLS, the pentagon diagram has the sub-leading Landau singularity which is the same as the LLS of the box diagram. The LLS occurs when* $M_H \geq 2M_W$ *and* $\sqrt{s} \geq 2m_t$*, i.e. all the four particles in the loop can be simultaneously on-shell.*

couplings are:

$$\begin{aligned} \lambda_{bbH} &= -\frac{m_b}{\upsilon}, \quad \lambda_{ttH} = -\frac{m_t}{\upsilon}, \\ \lambda_{tb\chi} &= -i\sqrt{2}\lambda_{ttH}(P_L - \frac{m_b}{m_t}P_R), \quad \lambda_{\chi^+\chi^- H} = \frac{M_H^2}{\upsilon}, \end{aligned}$$

where $\upsilon$ is the vacuum expectation value and $P_{L,R} = (1 \mp \gamma_5)/2$. The cross section as a function of $\lambda_{bbH}$ can be written in the form

$$\begin{aligned} \sigma(\lambda_{bbH}) &= \sigma(\lambda_{bbH} = 0) + \lambda_{bbH}^2 \sigma'(\lambda_{bbH} = 0) + \cdots, \\ \lambda_{bbH}^2 \sigma'(\lambda_{bbH} = 0) &\approx \sigma_{NLO} = \sigma_{LO}[1 + \delta_{NLO}(m_t, M_H)], \end{aligned}$$

where $\sigma(\lambda_{bbH} = 0)$ is shown in Fig. 2 (right), $\sigma_{LO}$ and $\sigma_{NLO}$ are shown in the same figure on the left.

$\sigma(\lambda_{bbH} = 0)$ is generated solely at one-loop level and gets large when $M_H$ is close to $2M_W$. This is due to the leading Landau singularity related to the scalar loop integral associated to the box diagram in the class (c) of Fig. 1. This divergence, which occurs when $M_H \geq 2M_W$, is not integrable at the level of loop amplitude squared and must be regulated by introducing a width for the unstable particles in the loops. Mathematically, the width effect is to move the LLS into the complex plane so that they do not occur in the physical region. The solution is shown in Fig. 3. The important point here is that the LLS, even after being regulated, can lead to a large correction to the cross section, up to 49% for $M_H = 163$GeV, $\Gamma_W = 2.1$GeV and $\Gamma_t = 1.5$GeV.

## Acknowledgments

The author would like to acknowledge the financial support from EU Marie Curie Programme. This work has been done in collaboration with Fawzi Boudjema.

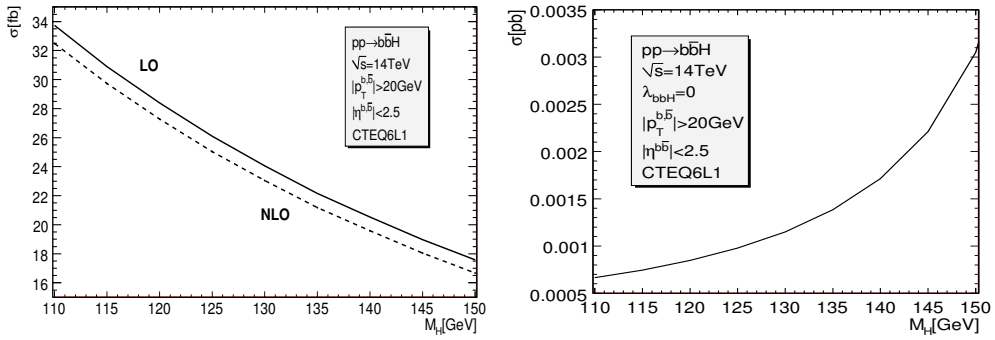


Figure 2: *Left: the leading order (LO) and NLO cross sections as functions of $M_H$. Right: the cross section in the limit of vanishing $\lambda_{bbH}$.*

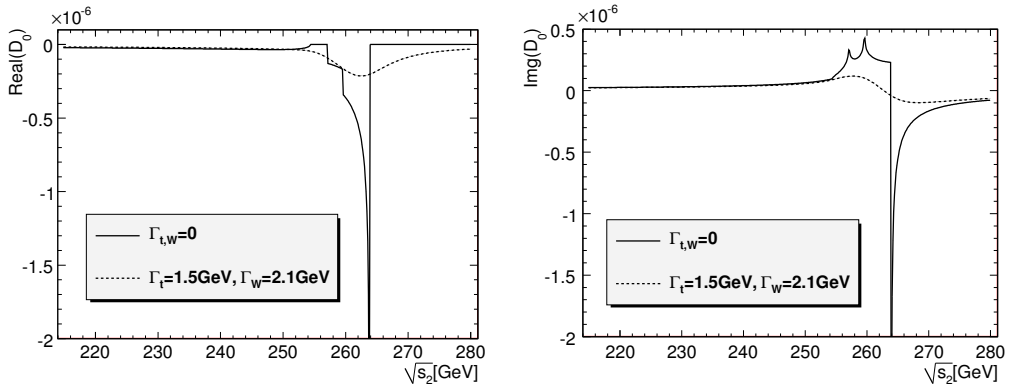


Figure 3: *The real and imaginary parts of the scalar box integral associated with the LLS diagram in the class (c) of Fig. 1.*

## References

1. S. Dittmaier, M. Krämer and M. Spira, Phys. Rev. D70, 074010 (2004); S. Dawson, C. B. Jackson, L. Reina and D. Wackeroth, Phys. Rev. D69, 074027 (2004).
2. F. Boudjema and Le Duc Ninh, Phys. Rev. D77, 033003 (2008).

# THE MSSM WITH DECOUPLED SCALARS AT THE LHC

E. TURLAY[a]
*Laboratoire de l'Accélerateur Linéaire*
*Université Paris-Sud 11, 91898 Orsay cedex, France*

The discovery potential for the MSSM with heavy scalars at the LHC in the case of light inos is examined. We discuss the phenomenology of the model and the observables to determine the parameters. We show that for light gauginos, the model parameters can be constrained with a precision of the order of 15%.

## 1 Introduction

Assuming a large soft–breaking scale for the MSSM scalars [1,2,3,4,5] pushes squarks, sfermions and heavy Higgses out of the kinematic reach of the LHC without affecting the gaugino sector. The hierarchy problem will not be solved without an additional logarithmic fine tuning of the Higgs sector. Nevertheless, a model can be constructed to provide a good candidate for dark matter and realize grand unification while minimizing proton decay and FCNCs. We investigate the LHC phenomenology of the model, where all scalars are decoupled from the low energy spectrum. We focus on gaugino–related signatures to estimate the accuracy with which its underlying parameters can be determined.

## 2 Phenomenology

The spectrum at the LHC is reduced to the gauginos, Higgsinos and the light Higgs. At the intermediate scale $M_S$ the effective theory is matched to the full theory and the usual MSSM renormalization group equations apply. The Higgsino mass parameter $\mu$ and the ratio $\tan\beta$ in the Higgs sector correspond to their MSSM counter parts. The gauginos masses $M_{1,2,3}$ and the Higgs-sfermion-sfermion couplings unify, and $M_S$ replaces the sfermion and the heavy Higgs'

[a] This work was done in collaboration with D. Zerwas (LAL-Orsay, Fr), N. Bernal and A. Djouadi (LPT-Orsay, Fr), M. Rauch and T. Plehn (U. of Edimburg, UK) and R. Lafaye (LAPP-Annecy, Fr)

| | | | |
|---|---|---|---|
| $\tilde{g}\tilde{g}$ | 68 pb | $\tilde{\chi}^{\pm}\tilde{g}$ | 311 fb |
| $\tilde{\chi}^{\pm}\tilde{\chi}^{0}$ | 12 pb | $\tilde{\chi}^{0}\tilde{g}$ | 223 fb |
| $\tilde{\chi}^{\pm}\tilde{\chi}^{\pm}$ | 6 pb | $\tilde{\chi}^{0}\tilde{\chi}^{0}$ | 98 fb |
| Total | | 87 pb | |

Table 1: NLO cross sections for SUSY pair production at the LHC.

mass parameters. This set resembles the mSUGRA parameter set except for $\tan\beta$ now playing the role of a matching parameter (with the heavy Higgses being decoupled) rather than that of an actual vev ratio [6].

We select our parameter point according to three constraints: first, we minimize the amount of fine tuning necessary to bring the light Higgs mass into the 100 to 200 GeV range and reduce $M_S$ to 10 TeV, still well outside the LHC mass range. The main reason for this low breaking scale is that we want the gluino to decay inside the detector (preferably at the interaction point) instead of being long–lived [8,4].

Secondly, we obtain the correct relic dark–matter density $\Omega h^2 = 0.111^{+0.006}_{-0.008}$ [10] by setting $\mu = 290$ GeV and $M_2(M_{\rm GUT}) = 132.4$ GeV or $M_2(M_{\rm weak}) = 129$ GeV. This corresponds to the light–Higgs funnel $m_{\rm LSP} \approx M_2/2 \approx M_h/2$, where the $s$-channel Higgs exchange enhances the LSP annihilation rate. And finally, $m_h$ needs to be well above the LEP limit, which we achieve by choosing $\tan\beta = 30$. We obtain $m_h = 129$ GeV, $m_{\tilde{g}} = 438$ GeV, chargino masses of 117 and 313 GeV, and neutralino masses of 60, 117, 296, and 310 GeV with a modified version of SuSpect [5,11], decoupling the heavy scalars from the MSSM RGEs. $\tilde{\chi}^0_2$ and $\tilde{\chi}^{\pm}_1$ as well as $\tilde{\chi}^0_4$ and $\tilde{\chi}^{\pm}_2$ are degenerate in mass. All supersymetric particles and most notably the gluino are much lighter than in the SPS1a parameter point It is important to note that this feature is specific to our choice of parameters and not generic in heavy–scalar models. As a consequence, all LHC production cross sections are greatly enhanced with respect to SPS1a.

Table 1 shows the main (NLO) cross sections at the LHC from Prospino2 [12,13,14]. The SUSY production is dominated by gluino pairs whose rate is eight times that of the SPS1a point: the lower gluino mass enlarges the available phase space, while in addition the destructive interference between $s$ and $t$–channel diagrams is absent. The second largest process is the $\tilde{\chi}^{\pm}_1\tilde{\chi}^0_2$ production, which gives rise to a 145 fb of hard-jet free, $e$ and $\mu$ trilepton signal, more than a hundred times that of the SPS1a point.

## 3 OBSERVABLES

The first obvious observable is the light Higgs mass $m_h$. Although slightly higher than in most MSSM points, $m_h$ can still be measured in the Higgs to two photons decay [15] ($m_h < 150$ GeV). The systematic error on this measurement is mainly due to the incertainty on the knowledge of the electromagnetic energy scale.

A measurement of the gluino pair production cross section appears feasible and could be very helpful to determine $M_3$. The branching ratio of gluinos decaying through a virtual squark into a chargino or a neutralino along with two jets is 85%. The chargino will in turn decay mostly into the LSP plus two leptons or jets. Such events would feature at least 4 high-$p_T$ jets, a large amount of missing energy due to the two $\tilde{\chi}^0_1$ in the final state and possibly leptons. The main backgrounds for such signatures are $t\bar{t}$ pairs, $W$+jets and $Z$+jets with respective production rates of 830 pb, 4640 pb and 220 pb [16]. Despite these large cross sections, most of the background can be eliminated by applying standard cuts on $\not{E}_T$, the number of high-$p_T$ jets as well as the effective mass[b] which we checked using a fast LHC-like simulation. The main

[b] $M_{\rm eff} = \not{E}_T + \sum p_T({\rm jets})$.

source of systematic errors for this observable is the 5% error on the knowledge of the luminosity. We take the theoretical error on the calculation of the cross section to be roughly 20%.

The next observable is the trilepton signal. After gluino pairs, the next dominant channel is the direct production of $\tilde{\chi}_1^\pm \tilde{\chi}_2^0$. 22% of $\tilde{\chi}_1^\pm$s decay through a virtual $W$ into an electron or muon and a neutrino and the LSP. Similarly, 7% of $\tilde{\chi}_2^0$s decay through a virtual $Z$ into an Opposite-Sign-Same-Flavour lepton pair (OSSF) and the LSP. The resulting signal features three leptons among which two are OSSF, a large amount of missing transverse energy due to the two LSPs plus the neutrino and no jet in the hard process. The background for this signature is mainly $WZ$ and $ZZ$ in which one of the leptons was non-identified or outside acceptance. According to `PYTHIA` the lepton production ($e$ and $\mu$) rates are 386 fb for $WZ$ and 73 fb for $ZZ$. The trilepton signal has a rate of 145 fb, using `SDECAY` [17] for the calculation of the branching ratios. Including identification efficiencies of 65% for electrons and of 80% for muons [18] gives rates of 110 to 211 fb for the background and 40 to 74 fb for the signal before any cut. A study with full detector simulation and reconstruction would provide a better understanding of signal and background. As in the previous case, the main source of systematic errors is the uncertainty on the luminosity. We also take the theoretical error on the value of the trilepton cross section to be roughly 20%.

Within this trilepton signal lies another observable. 10% of $\tilde{\chi}_2^0$s decay into an OSSF lepton pair and the LSP. The distribution of the invariant mass of the pair features a kinematic upper edge whose value is $m_{\tilde{\chi}_2^0} - m_{\tilde{\chi}_1^0}$. Such an observable gives precious information on the neutralino sector and hence on $M_1$. The systematic error is dominated by the lepton energy scale. The statistical error was extracted from a `ROOT` fit of the $M_{\ell\ell}$ distribution and we estimate the theoretical accuracy to be of the order of 1%.

The last observable we use in this study is the ratio of gluino decays including a $b$ quark to those not including a $b$. A systematic error of 5% due to the tagging of $b$-jets and a theoretical uncertainties of 20% are assumed.

| Observables | | Exp. systematic errors | | Statistical errors | Theoretical |
|---|---|---|---|---|---|
| | Value | Error | Source | 100 fb$^{-1}$ | |
| $m_h$ | 128.8 GeV | 0.1% | energy scale | 0.1% | 4% |
| $m_{\tilde{\chi}_2^0} - m_{\tilde{\chi}_1^0}$ | 57 GeV | 0.1% | energy scale | 0.3% | 1% |
| $\sigma(3\ell)$ | 145.2 fb | 5% | luminosity | 3% | 20% |
| $R(\tilde{g} \to b/!b)$ | 0.11 | 5% | $b$-tagging | 0.3% | 20% |
| $\sigma(\tilde{g}\tilde{g})$ | 68.2 pb | 5% | luminosity | 0.1% | 20% |

Table 2: Summary of the observables and the corresponding errors.

Table 2 summarises the value and error of the observables assumed in this study. The third and fourth columns give the experimental systematic errors and there source. The fifth column gives the statistical errors for an integrated luminosity of 100 fb$^{-1}$ corresponding to one year of data-taking at the LHC nominal luminosity. The last column gives an estimation of the theoretical uncertainties.

## 4 PARAMETER DETERMINATION

We use different sets of errors for the fits. First we determine the parameters in the low statistic scenario ignoring theoretical uncertainties. Second we assume an infinite statistic and therefore assume negligeable statistical errors to estimate the ultimate precision barrier imposed by experimental systematic errors. Finally the effect of theoretical uncertainties is estimated by including them into the previous set. We expect these to dominate.
With no information on the squark and sfermion sector at all, except for non-observation, we are

forced to fix $M_S$ and $A_t$ and set $M_2$ to be equal to $M_1$. We fit the parameters to the observables using the `Minuit` fitter. The minimum of the $\chi^2$ is found by `MIGRAD`. We start from a point far from the nominal values ($\{M_1, M_3, \tan\beta, \mu\} = \{100, 200, 10, 320\}$) and reach the values reported in table 3. Errors are determined with `MINOS`. Theoretical errors are treated as Gaussian.

| Parameter | Nom. values | Fit values | Low stat. | | $\infty$ stat. | | $\infty$ stat.+th | |
|---|---|---|---|---|---|---|---|---|
| $M_S$ | 10 TeV | | fixed | | | | | |
| $A_t$ | 0 | | fixed | | | | | |
| $M_1$ | 132.4 GeV | 132.8 GeV | $= M_2$ | | | | | |
| $M_2$ | 132.4 GeV | 132.8 GeV | 6 | 5% | 0.24 | 0.2% | 21.2 | 16% |
| $M_3$ | 132.4 GeV | 132.7 GeV | 0.8 | 0.6% | 0.16 | 0.1% | 5.1 | 4% |
| $\tan\beta$ | 30 | 28.3 | 60 | undet. | 1.24 | 4% | 177 | undet. |
| $\mu$ | 290 GeV | 288 GeV | 3.8 | 1.3% | 1.1 | 0.4% | 48 | 17% |

Table 3: Result of the fits. Errors on the determination of the parameter are given for the three error sets. Both absolute and relative values are given.

Table 3 shows the result of the fits in both absolute and relative values. It is interesting to note that $\tan\beta$ in undetermined except in the case of infinite statistical and theoretical accuracy. The quality of the trilepton and gluino signals gives very good precision on the determination of $M_1$ and $M_3$ even with low statisic. The inclusion of theoretical uncertainties indeed decreases the accuracy but still allows for a determination. $M_3$ only depends on the large gluino signal and its decays, explaining its relative stability. $M_1$ and $M_2$ see the largest impact of theoretical errors. This is because they depend on first order on the trilepton cross-section and on second order on the $b$ to non $b$ gluino decays ratio both of which bear a large theoretical error.

## 5 CONCLUSION

The MSSM with heavy scalars can very well satisfy current experimental and theoretical limits on physics beyond the standard model and also solve a good number of issues present in the traditionnal MSSM. We described its phenomenology at the LHC in the case of light inos and showed that such a simple and light spectrum could lead to very high production rates making the model discoverable. The main observable channels are gluino pairs and the trilepton channel whose hard-jet free channel makes it well distinct from SM and SUSY backgrounds. Other observables such as the light Higgs mass, the $|m_{\tilde{\chi}_2^0} - m_{\tilde{\chi}_1^0}|$ kinematic edge and the $b$ to non $b$ producing gluino decays could lead to a determination of most parameters to the level of a few percent with 100 fb$^{-1}$ ignoring theoretical errors. In a more realistic picture where we assumed non-zero theoretical errors, we saw that most parameters can be determined with a precision of 15%. We also saw that the scalar section including $\tan\beta$ could only be poorly determined if at all.
New complementary observables could help determine better the scalar sector. Equally, a look at other parameter points will provide a more complete view of the discovery potential of a MSSM with decoupled scalars at the LHC.

## References


1. N. Arkani-Hamed and S. Dimopoulos, *JHEP* **06** (2005) 073, `[hep-th/0405159]`.
2. G.F. Giudice and A. Romanino, *Nucl. Phys.* **B699** (2004) 64–89, `[hep-ph/0406088]`
3. J.D. Wells, *Phys. Rev.* **D71** (2005) 015013, `[hep-ph/0411041]`.
4. W. Kilian, T.Plehn, P. Richardson and E. Schmidt, *Eur. Phys. J.* **C39** (2005) 229–243, `[hep-ph/0408088]`.

5. N. Bernal, A. Djouadi and P. Slavich, *JHEP* **07** (2007) 016, [arXiv:0705.1496 [hep-ph]].
6. M. Drees [hep-ph/0501106].
7. S. Weinberg, *Phys. Rev. Lett.* **59** (1987) 2607.
8. A. C. Kraan, *Eur. Phys. J.* **C37** (2004) 91-104, hep-ex/0404001.
9. G. R. Farrar and P. Fayet, *Phys. Lett.* **B76** (1978) 575-579.
10. D. N. Spergel *et al.*, WMAP Collaboration, *Astrophys. J. Suppl.* **170** (2007) 377, astro-ph/0603449.
11. A. Djouadi, J.-L. Kneur and G. Moultaka, *Comput. Phys. Commun.* **176** (2007) 426-455, hep-ph/0211331.
12. W. Beenakker, R. Hopker, M. Spira and P. M. Zerwas, *Nucl. Phys* **B492** (1997) 51-103, hep-ph/9610490.
13. W. Beenakker *et al.*, *Phys. Rev. Lett.* **83** (1999) 3780-3783, hep-ph/9906298.
14. T. Plehn, (1998), hep-ph/9809319.
15. M. Bettinelli *et al.*, *ATL-PHYS-PUB-2007-013* (2007).
16. ATLAS Collaboration, TDR vol. 2 CERN-LHCC-99-15 (1999) 469.
17. M. Muhlleitner, *Acta Phys. Polon.* **B35** (2004) 2753-2766, hep-ph/0409200.
18. ATLAS Collaboration, Atlas Technical Paper.

# Search for the decay $K_S \to e^+e^-$

F. Archilli for KLOE collaboration[a]
*Dipartimento di Fisica dell'Università di Roma Tor Vergata & sezione INFN Roma Tor Vergata, Rome, Italy*

We present results of a direct search for the decay $K_S \to e^+e^-$ with the KLOE detector, obtained with a sample of $e^+e^- \to \phi \to K_S K_L$ events produced at DA$\Phi$NE, the Frascati $\phi$–factory, for an integrated luminosity of 1.9 fb$^{-1}$. The Standard Model prediction for this decay is BR($K_S \to e^+e^-$) $= 2 \times 10^{-14}$. The search has been performed by tagging the $K_S$ decays with simultaneous detection of a $K_L$ interaction in the calorimeter. Background rejection has been optimized by using both kinematic cuts and particle identification. At the end of the analysis chain we find BR($K_S \to e^+e^-$) $< 9.3 \times 10^{-9}$ at 90% CL, which improves by a factor of $\sim 15$ on the previous best result, obtained by CPLEAR experiment.

## 1 Introduction

The decay $K_S \to e^+e^-$, like the decay $K_L \to e^+e^-$ or $K_L \to \mu^+\mu^-$, is a flavour-changing neutral-current process, suppressed in the Standard Model and dominated by the two-photon intermediate state [1]. For both $K_S$ and$K_L$, the $e^+e^-$ channel is much more suppressed than the $\mu^+\mu^-$ one (by a factor of $\sim 250$) because of the $e-\mu$ mass difference. The diagram corresponding to the process $K_S \to \gamma^*\gamma^* \to \ell^+\ell^-$ is shown in Fig. 1. Using Chiral Perturbation Theory ($\chi$pT)

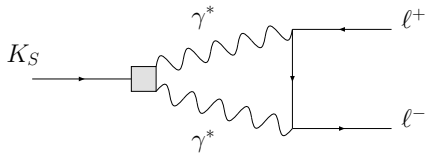


Figure 1: Long distance contribution to $K_S \to \ell^+\ell^-$ process, mediated by two-photon rescattering.

to order $\mathcal{O}(p^4)$, the Standard Model prediction BR($K_S \to e^+e^-$) is evaluated to be $\sim 2 \times 10^{-14}$. A value significantly higher than expected would point to new physics. The best experimental limit for $BR(K_S \to e^+e^-)$ has been measured by CPLEAR [2], and it is equal to $1.4 \times 10^{-7}$, at 90% CL. Here we present a new measurement of this channel, which improves on the previous result by a factor of $\sim 15$.

[a] F. Ambrosino, A. Antonelli, M. Antonelli, F. Archilli, P. Beltrame, G. Bencivenni, S. Bertolucci, C. Bini, C. Bloise, S. Bocchetta, F. Bossi, P. Branchini, P. Campana, G. Capon, T. Capussela, F. Ceradini, F. Cesario, P. Ciambrone, F. Crucianelli, E. De Lucia, A. De Santis, P. De Simone, G. De Zorzi, A. Denig, A. Di Domenico, C. Di Donato, B. Di Micco, M. Dreucci, G. Felici, M. L. Ferrer, S. Fiore, P. Franzini, C. Gatti, P. Gauzzi, S. Giovannella, E. Graziani, W. Kluge, V. Kulikov, G. Lanfranchi, J. Lee-Franzini, D. Leone, M. Martini, P. Massarotti, S. Meola, S. Miscetti, M. Moulson, S. Müller, F. Murtas, M. Napolitano, F. Nguyen, M. Palutan, E. Pasqualucci, A. Passeri, V. Patera, F. Perfetto, P. Santangelo, B. Sciascia, A. Sciubba, A. Sibidanov, T. Spadaro, M. Testa, L. Tortora, P. Valente, G. Venanzoni, R.Versaci

## 2 Experimental setup

The data were collected with KLOE detector at DAΦNE, the Frascati $\phi$–factory. DAΦNE is an $e^+e^-$ collider that operates at a center-of-mass energy of $\sim 1020\,\mathrm{MeV}$, the mass of the $\phi$ meson. $\phi$ mesons decay $\sim 34\%$ of the time into nearly collinear $K^0\bar{K}^0$ pairs. Because $J^{PC}(\phi) = 1^{--}$, the kaon pair is in an antisymmetric state, so that the final state is always $K_SK_L$. Therefore, the detection of a $K_L$ signals the presence of a $K_S$ of known momentum and direction, independently of its decay mode. This technique is called $K_S$ *tagging*. A total of $\sim 4$ billion $\phi$ were produced, yielding $\sim 1.4$ billion of $K_SK_L$ pairs.

The KLOE detector consists of a large cylindrical drift chamber (DC), surrounded by a lead/scintillating-fiber sampling calorimeter (EMC). A superconductig coil surrounding the calorimeter provides a $0.52\,\mathrm{T}$ magnetic field. The drift chamber [3], $4\,\mathrm{m}$ in diameter and $3.3\,\mathrm{m}$ long, is made of carbon-fibers/epoxy and filled with a light gas mixture, 90% He-10%i$C_4H_{10}$. The DC position resolutions are $\sigma_{xy} \approx 150\mu\mathrm{m}$ and $\sigma_z \approx 2\,\mathrm{mm}$. DC momentum resolution is $\sigma(p_\perp)/p_\perp \approx 0.4\%$. Vertices are reconstructed with a spatial resolution of $\sim 3\,\mathrm{mm}$.

The calorimeter [4] is divided into a barrel and two endcaps and covers 98% of the solid angle. The energy and time resolutions are $\sigma_E/E = 5.7\%/\sqrt{E(\mathrm{GeV})}$ and $\sigma_t = 57\,\mathrm{ps}/\sqrt{E(\mathrm{GeV})}\oplus 100\,\mathrm{ps}$, respectively.

To study the background rejection, a MC sample of $\phi$ decays to all possible final states has been used, for an integrated luminosity of $\sim 1.9\,\mathrm{fb}^{-1}$. A MC sample of $\sim 45000$ signal events has been also produced, to measure the analysis efficiency.

## 3 Data analysis

The identification of $K_L$-interaction in the EMC is used to tag the presence of $K_S$ mesons. The mean decay lenghts of $K_S$ and $K_L$ are $\lambda_S \sim 0.6\,\mathrm{cm}$ and $\lambda_L \sim 350\,\mathrm{cm}$, respectively. About 50% of $K_L$'s therefore reach the calorimeter before decaying. The $K_L$ interaction in the calorimeter barrel ($K_{\mathrm{crash}}$) is identified by requiring a cluster of energy greater than $125\,\mathrm{MeV}$ not associated with any track, and whose time corresponds to a velocity $\beta = r_{cl}/ct_{cl}$ compatible with the kaon velocity in the $\phi$ center of mass, $\beta^* \sim 0.216$, after the residual $\phi$ motion is considered. Cutting at $0.17 \leq \beta^* \leq 0.28$ we selected $\sim 650$ million $K_S$-tagged events ($K_{\mathrm{crash}}$ events in the following), which are used as a starting sample for the $K_S \to e^+e^-$ search.

$K_S \to e^+e^-$ events are selected by requiring the presence of two tracks of opposite charge with their point of closest approach to the origin inside a cylinder $4\,\mathrm{cm}$ in radius and $10\,\mathrm{cm}$ in length along the beam line. The track momenta and polar angles must satisfy the fiducial cuts $120 \leq p \leq 350\,\mathrm{MeV}$ and $30^\circ \leq \theta \leq 150^\circ$. The tracks must also reach the EMC without spiralling, and have an associated cluster. In Fig. 2, the two-track invariant mass evaluated in electron hypothesis ($M_{ee}$) is shown for both MC signal and background samples. A preselection cut requiring $M_{ee} > 420\,\mathrm{MeV}$ has been applied, which rejects most of $K_S \to \pi^+\pi^-$ events, for which $M_{ee} \sim 409\,\mathrm{MeV}$. The residual background has two main components: $K_S \to \pi^+\pi^-$ events, populating the low $M_{ee}$ region, and $\phi \to \pi^+\pi^-\pi^0$ events, spreading over the whole spectrum. The $K_S \to \pi^+\pi^-$ events have such a wrong reconstructed $M_{ee}$ because of track resolution or one pion decaying into a muon. The $\phi \to \pi^+\pi^-\pi^0$ events enter the preselection because of a machine background cluster, accidentally satisfying the $K_{\mathrm{crash}}$ algorithm. After preselection we are left with $\sim 5 \times 10^5$ events. To have a better separation between signal and background, a $\chi^2$-like variable is defined, collecting informations from the clusters associated to the candidate electron tracks. Using the MC signal events we built likelihood functions based on: the sum and the difference of $\delta t$ for the two tracks, where $\delta t = t_{cl} - L/\beta c$ is evaluated in electron hypothesis; the ratio $E/p$ between the cluster energy and the track momentum, for both charges; the

cluster depth, evaluated respect to the track, for both charges. In Fig. 2, the scatter plot of $\chi^2$ versus $M_{ee}$ is shown, for MC signal and background sources. The $\chi^2$ spectrum for background is concentrated at higher values respect to signal, since both $K_S \to \pi^+\pi^-$ and $\phi \to \pi^+\pi^-\pi^0$ events have pions in the final state.

A signal box to select the $K_S \to e^+e^-$ events can be conveniently defined in the $M_{ee} - \chi^2$ plane (see Fig. 2); nevertheless we investigated some more independent requirements in order to reduce the background contamination as much as possible before applying the $M_{ee}-\chi^2$ selection.

Charged pions from $K_S \to \pi^+\pi^-$ decay have a momentum in the $K_S$ rest frame $p^*_\pi \sim 206\,\mathrm{MeV}$. The distribution of track momenta in the $K_S$ rest frame, evaluated in the pion mass hypothesis, is shown in Fig. 2, for MC background and MC signal. For most of $K_S \to \pi^+\pi^-$ decays, at least one pion has well reconstructed momentum, so that the requirements

$$\min(p^*_\pi(1), p^*_\pi(2)) \geq 220\,\mathrm{MeV} \quad , \quad p^*_\pi(1) + p^*_\pi(2) \geq 478\,\mathrm{MeV} \tag{1}$$

rejects $\sim 99.9\%$ of these events, while retaining $\sim 92\%$ of the signal.

To reject $\phi \to \pi^+\pi^-\pi^0$ events we have applied a cut on the missing momentum, defined as:

$$P_{\mathrm{miss}} = \left| \vec{P}_\phi - \vec{P}_L - \vec{P}_S \right| \tag{2}$$

where $\vec{P}_{L,S}$ are the neutral kaon momenta, and $\vec{P}_\phi$ is the $\phi$ momentum. The distribution of $P_{\mathrm{miss}}$ is shown in Fig. 2, for MC background and for MC signal events. We require

$$P_{\mathrm{miss}} \leq 40\,\mathrm{MeV}\,, \tag{3}$$

which rejects almost completely the $3\pi$ background source which is distributed at high missing momentum.

A signal box is defined in the $M_{ee} - \chi^2$ plane as shown Fig. 2. The $\chi^2$ cut for the signal box definition has been chosen to remove all MC background events: $\chi^2 < 70$. The cut on $M_{ee}$ is practically set by the $p^*_\pi$ cut, which rules out all signal events with a radiated photon with energy greter than 20 MeV, correspondig to an invariant mass window: $477 < M_{ee} \leq 510\,\mathrm{MeV}$. The signal box selection on data gives $N_{obs} = 0$. The upper limit at 90% CL on the expected number of signal events is $UL(\mu_S) = 2.3$.

## 4 Results

The total selection efficiency on $K_S \to e^+e^-$ events is evaluated by MC, using the following parametrization:

$$\epsilon_{sig} = \epsilon(K_{crash}) \times \epsilon(sele|K_{crash})\,, \tag{4}$$

where $\epsilon(K_{crash})$ is the tagging efficiency, and $\epsilon(sele|K_{crash})$ is the signal selection efficiency on the sample of tagged events. The efficiency evaluation includes contribution from radiative corrections. The number of $K_S \to \pi^+\pi^-$ events $N_{\pi^+\pi^-}$ counted on the same sample of $K_S$ tagged events is used as normalization, with a similar expression for the efficiency. The upper limit on $\mathrm{BR}(K_S \to e^+e^-)$ is evaluated as follows:

$$UL(BR(K_S \to e^+e^-)) = UL(\mu_s) \times \mathcal{R}_{tag} \times \frac{\epsilon_{\pi^+\pi^-}(sele|K_{crash})}{\epsilon_{sig}(sele|K_{crash})} \times \frac{BR(K_S \to \pi^+\pi^-)}{N_{\pi^+\pi^-}}, \tag{5}$$

where $\mathcal{R}_{tag}$ [5] is the tagging efficiency ratio, corresponding to a small correction due to the $K_{\mathrm{crash}}$ algorithm dependence on $K_S$ decay mode, and it is equal to 0.9634(1).Using $\epsilon_{sig}(sele|K_{crash}) = 0.465(4)$, $\epsilon_{\pi^+\pi^-}(sele|K_{crash}) = 0.6102(5)$ and $N_{\pi^+\pi^-} = 217,422,768$, we obtain

$$UL(BR(K_S \to e^+e^-(\gamma))) = 9.3 \times 10^{-9},\ \text{at } 90\%\,\mathrm{CL}\,. \tag{6}$$

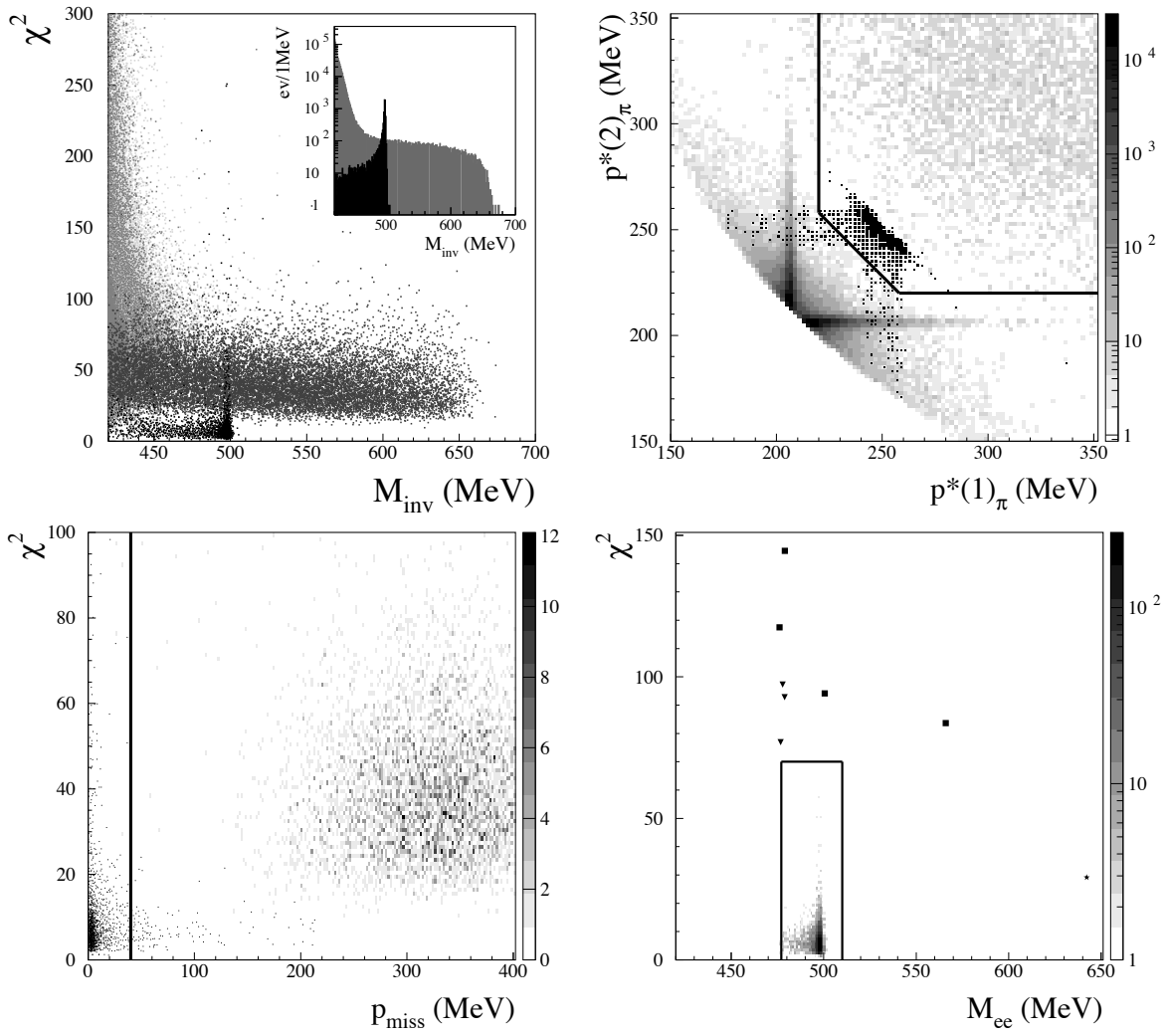


Figure 2: Top left: $\chi^2$ vs $M_{ee}$ distributions for MC signal (black), MC backgrounds $K_S \to \pi^+\pi^-$ and $\phi \to \pi^+\pi^-\pi^0$ (light and dark grey respectively), $M_{ee}$ distributions for MC signal (black) and MC backgrounds (grey) is shown in the inset; top right: $p^*_\pi$ distributions for MC signal (black) and MC background (grey scale); bottom left: $\chi^2$ vs $P_{\rm miss}$ distributions for MC signal (black) and MC background (grey scale); bottom right: $\chi^2$ vs $M_{ee}$ distributions for MC signal (grey scale), data (■), $K_S \to \pi^+\pi^-$ (▼) and $\phi \to \pi^+\pi^-\pi^0$ (★) after background rejection cuts.

Our measurement improves by a factor of $\sim$ 15 on the CPLEAR result [2], for the first time including radiative corrections in the evaluation of the upper limit.

## References

1. G. Ecker and A. Pich, Nucl. Phys. **B 366** (1991) 189.
2. A. Angelopoulos et al., Phys. Lett. **B 413** (1997) 232.
3. KLOE collaboration, M. Adinolfi *et al.*, Nucl. Istrum. Meth. **A 488** (2002) 51.
4. KLOE collaboration, M. Adinolfi *et al.*, Nucl. Istrum. Meth. **A 482** (2002) 363.
5. KLOE collaboration, F. Ambrosino *et al.*, Eur. Phys. J. C **48** (2006) 767

# CP ASYMMETRIES FROM NON-UNITARY LEPTONIC MIXING

J. LÓPEZ-PAVÓN
*Departamento de Física Teórica and Instituto de Física Teórica UAM/CSIC, Universidad Autónoma de Madrid, 28049 Cantoblanco, Madrid, Spain*

A low-energy non-unitary leptonic mixing matrix is a generic effect of some theories of new physics accounting for neutrino masses. We show how the extra CP-phases of a general non-unitary matrix allow for sizeable CP-asymmetries in the $\nu_\mu \to \nu_\tau$ channel. This CP-asymmetries turns out to be an excellent probe of such new physics.

.

## 1 Introduction

Non-zero neutrino masses constitutes one of the main evidence for physics beyond the Standard Model of particle physics (SM). In the complete theory accounting for them and encompassing the SM the complete mixing matrices should be unitary, as mandated by probability conservation. However, the effective $3 \times 3$ submatrices describing the mixing of the light fermionic fields need not to be unitary, since these known fields in the theory may mix with other degrees of freedom. We will assume that the full theory is indeed unitary, whereas, low-energy non-unitarity may result from BSM physics contributing to neutrino propagation, when the physical measurements are described solely in terms of SM fields [1]. Specifically, the tree-level exchange of heavy fermions (scalars) will (not) induce low-energy non-unitary contributions through dimension six effective operators [2].

In Ref. [1] the so-called MUV (minimal unitarity violation) was developed and the *absolute* values of the elements of the matrix N were determined. However, no information on the phases of the mixing matrix is available, neither on the standard phases nor on the new non-unitary ones, as present oscillation data correspond mainly to disappearance experiments. Here we will explore the future sensitivity to the new CP-odd phases of the leptonic mixing matrix associated to non-unitary. In particular, it will be shown that CP-asymmetries in the $\nu_\mu \to \nu_\tau$ channel are an excellent probe of such new physics. Notice that CP-odd effects in that channel are negligible in the standard unitary case, in which the golden channel for CP-violation is $\nu_e \to \nu_\mu$.

## 2 Formalism

We start from the parametrization of the general non-unitary matrix $N$, which relates flavor and mass fields, as the product of an hermitian and a unitary matrix, defined by

$$\nu_\alpha = N_{\alpha i}\, \nu_i \equiv [(1+\eta)U]_{\alpha i}\, \nu_i \,, \tag{1}$$

with $\eta^\dagger = \eta$. Since $NN^\dagger = (1+\eta)^2 \approx 1+2\eta$, the bounds derived in Ref.[1] for the modulus of the elements of $NN^\dagger$ can also be translated into constraints on the elements of $\eta$. It follows that

$$|\eta| = \begin{pmatrix} < 5.5 \cdot 10^{-3} & < 3.5 \cdot 10^{-5} & < 8.0 \cdot 10^{-3} \\ < 3.5 \cdot 10^{-5} & < 5.0 \cdot 10^{-3} & < 5.1 \cdot 10^{-3} \\ < 8.0 \cdot 10^{-3} & < 5.1 \cdot 10^{-3} & < 5.0 \cdot 10^{-3} \end{pmatrix}, \tag{2}$$

at the 90% confidence level. The bounds have been updated with the latest experimental bound on $\tau \to \mu\gamma$ [3]. Eq. (2) shows that the matrix $N$ is constrained to be unitary at the per cent level accuracy or better. Therefore, the unitary matrix $U$ in Eq. (1) can be identified with the usual unitary mixing matrix $U = U_{PMNS}$, within the same accuracy. The flavor eigenstates can then be conveniently expressed as [a]

$$|\nu_\alpha> = \frac{(1+\eta^*)_{\alpha\beta} U^*_{\beta i}}{[1+2\eta_{\alpha\alpha} + (\eta^2)_{\alpha\alpha}]^{1/2}} \, |\nu_i> \equiv \frac{(1+\eta^*)_{\alpha\beta}}{[1+2\eta_{\alpha\alpha} + (\eta^2)_{\alpha\alpha}]^{1/2}} \, |\nu^{SM}_\beta> . \tag{3}$$

So the neutrino oscillation amplitude, neglecting terms quadratic in $\eta$, is given simply by

$$< \nu_\beta | \nu_\alpha(L) > = A^{SM}_{\alpha\beta}(L) \, (1 - \eta_{\alpha\alpha} - \eta_{\beta\beta}) + \sum_\gamma \left( \eta^*_{\alpha\gamma} A^{SM}_{\gamma\beta}(L) + \eta_{\beta\gamma} A^{SM}_{\alpha\gamma}(L) \right) , \tag{4}$$

with

$$A^{SM}_{\alpha\beta}(L) \equiv < \nu^{SM}_\beta | \nu^{SM}_\alpha(L) > \tag{5}$$

being the usual oscillation amplitude of the unitary analysis.

In order to study the posible new CP-violation signals arising from the new phases in $\eta$, one has to consider appearance channels, $\alpha \neq \beta$. The best sensitivities to such phases will be achieved in a regime where the first term in Eq. (4) is suppressed. This is possible at short enough baselines, where the standard appearance amplitudes are very small while $A^{SM}_{\alpha\alpha}(L) \simeq 1$. In that case the total amplitude is well approached by

$$< \nu_\beta | \nu_\alpha(L) > = A^{SM}_{\alpha\beta}(L) + 2\eta^*_{\alpha\beta} + \mathcal{O}(\eta\, A), \tag{6}$$

where $\mathcal{O}(\eta\, A)$ only includes appearance amplitudes and $\eta$ components with flavor indices other than $\alpha\beta$. Then, at short enough baselines, each oscillation probability in a given flavor channel, $P_{\alpha\beta}$, is mostly sensitive to the corresponding $\eta_{\alpha\beta}$. The rest of the elements of the $\eta$ matrix can be safely disregarded in the analysis below, without implying to assume zero values for them. That is, their effect is subdominant, a fact that has been numerically checked for the main contributions.

For instance, within the above-described approximation, the oscillation probability for two families would read:

$$P_{\alpha\beta} = \sin^2(2\theta) \sin^2\left(\frac{\Delta L}{2}\right) - 4|\eta_{\alpha\beta}| \sin\delta_{\alpha\beta} \sin(2\theta) \sin(\Delta L) + 4|\eta_{\alpha\beta}|^2, \tag{7}$$

where $\Delta = \Delta m^2/2E$ and $\eta_{\alpha\beta} = |\eta_{\alpha\beta}| e^{-i\delta_{\alpha\beta}}$. The first term in the above equation is the standard oscillation probability. The third term is associated to the zero-distance effect stemming from the non-orthogonality of the flavor eigenstates [1]. Finally, the second term is the CP-violating interference between the other two which we are interested in. Notice that, even in two families, there is CP-violation due to the non-unitarity.

[a] The handy superscript $SM$ is an abuse of language, to describe the flavor eigenstates of the standard unitary analysis.

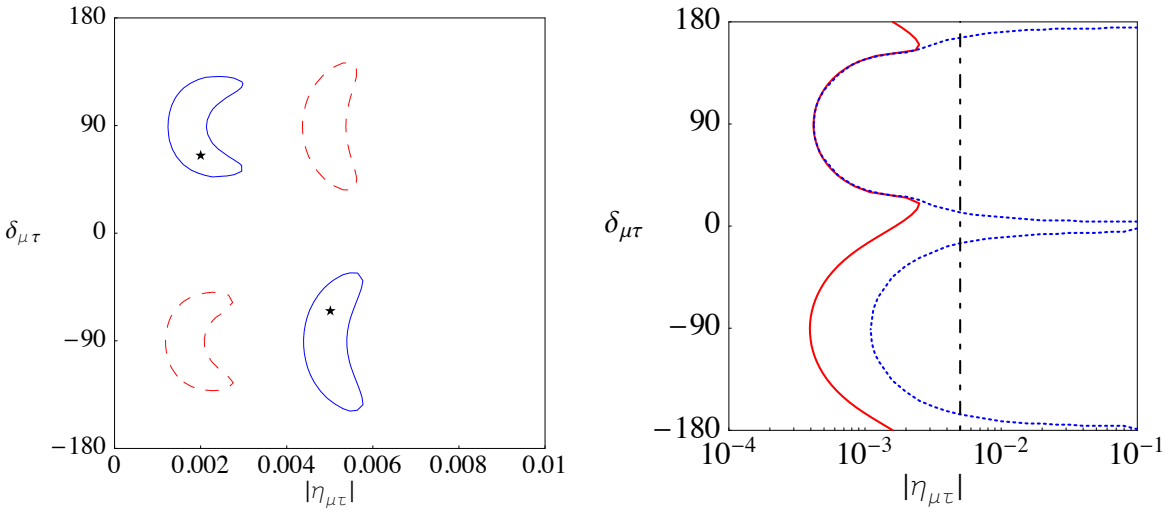


Figure 1: *Left: $3\sigma$ contours for two input values of $|\eta_{\mu\tau}|$ and $\delta_{\mu\tau}$ represented by the stars. Right: the solid line represents the $3\sigma$ sensitivity to $|\eta_{\mu\tau}|$ as a function of $\delta_{\mu\tau}$, the dotted line the $3\sigma$ sensitivity to $\delta_{\mu\tau}$ and the dotted-dashed line represents the present bound from $\tau \to \mu\gamma$.*

## 3 Sensitivity to the new CP-odd phases: the $\nu_\mu \to \nu_\tau$ channel

This channel is the best option to study the CP-violation comming from non-unitarity. This is because present constraints on $\eta_{e\mu}$ are too strong to allow a signal in the $\nu_e \to \nu_\mu$ one (see Eq. (2)), and $\nu_e \to \nu_\tau$ has extra supressions by small standard parameters such as $\sin\theta_{13}$ or $\Delta_{12}$ [4]. In the numerical computation of $P_{\mu\tau}$, the only approximation performed is to neglect all $\eta$ elements but $\eta_{\mu\tau}$. They should be indeed subdominant (see Eq. (6)). This approximation has been checked numerically.

Eq. (7) suggests us that the best sensitivities to CP-violation will be achieved at short baselines and high energies, where the standard term is suppressed by $\sin^2(\frac{\Delta L}{2})$. Therefore, we will study a Neutrino Factory beam [5] resulting from the decay of 50 GeV muons, to be detected at a 130 Km baseline, which matches for example the CERN-Frejus distance. For this set-up, $\sin(\frac{\Delta_{31}L}{2}) \simeq 1.7 \cdot 10^{-2}$ and $\sin(\frac{\Delta_{21}L}{2}) \simeq 6 \cdot 10^{-4}$, where $\Delta_{jk} \equiv (m_j^2 - m_k^2)/2E$. Then, if the $\eta_{\mu\tau}$ value is close to their experimental limit in Eq. (2), all terms in the oscillation probability given in Eq. (7) can be of similar order for the channel $\nu_\mu \to \nu_\tau$. On the experimental side, we will assume $2 \cdot 10^{20}$ useful decays per year and five years running with each polarity, consider a 5 Kt Opera-like detector and, finally, sensitivities and backgrounds a factor 5 larger [4] than those used for the $\nu_e \to \nu_\tau$ channel in Ref. [6].

Since this channel is not suppressed by small standard parameters such as $\sin\theta_{13}$ or $\Delta_{12}$, the two family approximation in Eq. (7), with $\theta = \theta_{23}$ and $\Delta = \Delta_{31}$, is very accurate to understand the results [b]. This equation indicates that the CP-odd interference term is only suppressed linearly in $|\eta_{\mu\tau}|$. This can indeed be observed in the result of the complete numerical computation, Fig. 1, which shows the sensitivities to $|\eta_{\mu\tau}|$ and $\delta_{\mu\tau}$ obtained. The left panel represents two fits to two different input values of $|\eta_{\mu\tau}|$ and $\delta_{\mu\tau}$ (depicted by stars). The dashed lines correspond to fits done assuming the *wrong* hierarchy, that is the opposite sign for $\Delta_{31}$ to that with which the number of events were generated. As expected from Eq. (7), a change of sign for the mass difference can be traded by a change of sign for $\delta_{\mu\tau}$. Nevertheless, this does not spoil the potential for the discovery of CP violation, since a non-trivial value for $|\delta_{\mu\tau}|$ is enough

[b] The complete expanded expression for $P_{\mu\tau}$ can be found in Ref [4].

to indicate CP violation. Furthermore, the sinusoidal dependence implies as well a degeneracy between $\delta_{\mu\tau} \to 180^\circ - \delta_{\mu\tau}$, as reflected in the figure.

The right panel in Fig. 1 depicts the $3\sigma$ sensitivities to $|\eta_{\mu\tau}|$ (solid line) and $\delta_{\mu\tau}$ (dotted line), while the present bound from $\tau \to \mu\gamma$ is also shown (dashed line). The poorest sensitivity to $|\eta_{\mu\tau}|$, around $10^{-3}$, is found in the vicinity of $\delta_{\mu\tau} = 0$ and $\delta_{\mu\tau} = 180^\circ$, where the CP-odd interference term vanishes and the bound is placed through the subleading $|\eta_{\mu\tau}|^2$ term. The latter is also present at zero distance and its effects were already considered in Ref.[1], obtaining a bound of similar magnitude. The sensitivity to $|\eta_{\mu\tau}|$ peaks around $|\eta_{\mu\tau}| \simeq 4{\cdot}10^{-4}$ for $\delta_{\mu\tau} \simeq \pm 90^\circ$, where $\sin\delta_{\mu\tau}$ is maximum. That is, for non-trivial values of $\delta_{\mu\tau}$ not only CP-violation could be discovered, but values of $|\eta_{\mu\tau}|$ an order of magnitude smaller could be probed.

## 4 Conclusions

The flavour mixing matrix present in leptonic weak currents may be generically non-unitary, as a result of new physics responsible for neutrino masses. Even if the effects are expected to be extremely tiny in the simplest models of neutrino masses, it is important to analyze the low-energy data without assuming a unitary leptonic mixing matrix, since it is a generic window of new physics.

A non-unitary matrix has more moduli and phases than a unitary one. The last ones may lead to new signals of CP-violation. In particular, we have shown that an asymmetry between the strength of $\nu_\mu \to \nu_\tau$ oscillations versus that for $\bar{\nu}_\mu \to \bar{\nu}_\tau$ results to be a beautiful and excellent probe of new physics, considering short-baselines ($\sim 100$ km.) and a Neutrino Factory beam of energy $\mathcal{O}(20GeV)$. Non-trivial values of the new phases can also allow to probe the absolute value of the moduli down to $10^{-4}$, an improvement of an order of magnitude over previous analyzes of future facilities.

## Acknowledgments

We acknowledge illuminating discussions with Florian Bonnet and Adolfo Guarino during a recent brief stay in Paris. We are also indebted for stimulating comments to Beatriz Cañadas and F. Jimenez-Alburquerque. This work was partially supported by the European Union through the "Marie Curie" grant, the author also acknowledges financial support from the MEC through the FPU grant with ref. AP2005-1185.

## References

1. S. Antusch, C. Biggio, E. Fernandez-Martinez, M. B. Gavela and J. Lopez-Pavon, JHEP **0610** (2006) 084 [arXiv:hep-ph/0607020].
2. A. Abada, C. Biggio, F. Bonnet, M. B. Gavela and T. Hambye, arXiv:0707.4058 [hep-ph].
3. [Belle Collaboration], arXiv:hep-ex/0609049.
4. E. Fernandez-Martinez, M. B. Gavela, J. Lopez-Pavon and O. Yasuda, Phys. Lett. B **649** (2007) 427 [arXiv:hep-ph/0703098].
5. S. Geer, Phys. Rev. D **57** (1998) 6989 [Erratum-ibid. D **59** (1999) 039903] [arXiv:hep-ph/9712290]; A. De Rujula, M. B. Gavela and P. Hernandez, Nucl. Phys. B **547** (1999) 21 [arXiv:hep-ph/9811390].
6. D. Autiero *et al.*, Eur. Phys. J. C **33** (2004) 243 [arXiv:hep-ph/0305185].

# DETERMINATION OF THE $B_s$ LIFETIME USING HADRONIC DECAYS

A.J. Deisher on behalf of the CDF Collaboration

*Lawrence Berkeley National Laboratory, 1 Cyclotron Road, Mail Stop 50B-5239, Berkeley, CA 94720, USA*

We present a measurement of the $B_s^0$ meson lifetime using fully and partially reconstructed hadronic decays $B_s^0 \to D_s^- \pi^+(X)$ followed by $D_s^- \to \phi\pi^-$. The data sample was recorded with the CDF II detector at the Fermilab Tevatron and corresponds to an integrated luminosity of 1.3 fb$^{-1}$ from $p\bar{p}$ collisions at $\sqrt{s} = 1.96$ TeV.

## 1 Introduction

For hadrons containing the heavy $b$ quark, one might assume that the light quark is only a spectator to the decay of the $b$, and the lifetimes of all the $b$ hadrons are the same regardless of the light quark's flavor. However, the spectator quarks do participate in the decay, and the hierarchy $\tau(B_c) < \tau(\Lambda_b) < \tau(B_s) \cong \tau(B_d) < \tau(B_u)$ has been both theoretically predicted and experimentally observed. The ratio of lifetimes is often quoted so some systematic uncertainties cancel. Recent theoretical calculations predict $\tau(B_u)/\tau(B_d) = 1.06 \pm 0.02$, $\tau(B_s)/\tau(B_d) = 1.00 \pm 0.01$, and $\tau(\Lambda_b)/\tau(B_d) = 0.86 \pm 0.05$. [1] The world averages for the corresponding experimental numbers are $1.071 \pm 0.009$, $0.939 \pm 0.021$, and $0.921 \pm 0.036$, respectively. [2] The experimental uncertainties are smaller than the theoretical uncertainties for all but the $B_s$ ratio. As $\tau(B_d)$ is already well measured, further improvements must come from reducing the uncertainty on $\tau(B_s)$.

In this Proceeding we present the most precise flavor-specific measurement of the $B_s$ lifetime to date. The data come from $p\overline{p}$ collisions at $\sqrt{s} = 1.96$ TeV produced at the Fermilab Tevatron. This analysis is based on an integrated luminosity of $\sim$1.3 fb$^{-1}$ collected by the CDF II detector [3] between February 2002 and November 2006. After trigger and analysis selection criteria have been applied, the sample yields more than 1100 fully reconstructed $B_s \to D_s^- \pi^+$ candidates with $D_s \to \phi\pi^-$ and $\phi \to (K^+K^-)$ .[a] In addition, the sample reconstructed as $B_s \to D_s^- \pi^+$ includes a similar number of partially reconstructed $B_s$ candidates, for example, $B_s \to D_s^- \rho^+$ followed by $\rho^+ \to \pi^+\pi^0$ where the $\pi^0$ is not reconstructed, that can contribute to the lifetime measurement and double the number of events available for analysis. The increase comes with an uncertainty due to missing particles or incorrect mass assumptions, but the uncertainty can be properly accounted for and folded into the likelihood formulation.

[a] Charge conjugation is implied throughout this Proceeding.

## 2 Analysis Method

A data sample rich in hadronic $B$ decays was selected with a three-level trigger system that searches for tracks displaced from the primary vertex. The trigger level requirements preferentially select longer lived particles, shaping the proper time distribution. Thus the exponential distribution of lifetimes no longer extends down to $ct = 0$. Instead there is a visible "trigger turn-on" in the distribution, which is visible in Figure 2.

The lifetime of the $B_s$ meson is determined from two sequential fits. The first fit is a maximum likelihood fit to the invariant mass distribution of candidates reconstructed as $D_s^-(\phi\pi^-)\pi^+$ with $m(D_s^-(\phi\pi^-)\pi^+) \in [4.85,\ 6.45]$ GeV/$c^2$ This fit determines the relative fractions of various decay modes and backgrounds in the data sample. Using the fractions determined in the mass fit as inputs, the second fit is to the proper decay time distributions for the $B_s$.

The lifetime of the $B_s$ meson is determined from an unbinned likelihood fit to the $B_s$ candidates with invariant masses in [5.00, 5.45] GeV/$c^2$. We use separate probability distribution functions (PDFs) for the fully reconstructed (FR) modes, partially reconstructed (PR) modes, and the backgrounds. For the lifetime fit the variable of interest is the proper decay time, defined as $ct \equiv \frac{L_{xy} \cdot m_B^{rec}}{p_{T_B}}$ where $L_{xy}$ is the decay length projected along the transverse momentum of the $B_s$, $p_{T_B}$. Notice that the reconstructed mass is used instead of the world average $B_s$ mass. A salient feature of this analysis is the treatment of partially reconstructed $B_s$ mesons as signal events that contribute to the lifetime measurement. Since in the partially reconstructed cases $L_{xy}$, $m_B^{rec}$, and $p_{T_B}$ are extracted from candidates that are missing tracks after reconstruction or have the wrong mass assignment for a single daughter particle, a multiplicative correction factor $K$ to the decay length is needed. $K$ is defined as $K = \frac{1}{\cos\theta_{\rm PR}} \cdot \frac{p_T(\rm PR)}{p_T(\rm true)} \cdot \frac{m_B(\rm true)}{m_{rec}(\rm PR)}$ where $\theta_{PR}$ is the angle in the $x-y$ plane between the true momentum of the $B_s$ and the momentum of the partially reconstructed $B_s$.

There are separate PDFs for the three categories of proper time distributions. How each component is treated depends on its decay structure and whether it can provide information about the $B_s$ lifetime. The FR and PR PDFs depend on $\tau_B$, the $B_s$ lifetime, while the background PDFs have fixed shapes.

- **Fully Reconstructed:** The only fully reconstructed mode is the $D_s\pi$. The root functional form of the FR PDF (given in Equation 1) is an exponential with decay constant $\tau(B_s)$ convoluted with a Gaussian resolution function with width $\sigma$. A multiplicative "efficiency curve" of the form given in Equation 2 accounts for the trigger and analysis selection criteria. The shape parameters ($\sigma$, $\beta_i$, $N_i$ and $\tau_i$) of the PDF come from a fit to a simulated $B_s$ sample where the lifetime used for generation is known. All the parameters for the PDF except for $\tau(B_s)$ are then fixed in the final fit to data. Note that although $\sigma$ is intended to be a detector resolution, it floats along with the efficiency curve parameters during the fits to the Monte Carlo. During this process it becomes correlated with the other parameters describing the overall PDF shape and loses some of its physical meaning.

$$P_{\rm FR}(ct) = \left[ \frac{1}{c\tau} e^{\frac{-ct'}{c\tau}} \otimes_{t'} \frac{1}{\sqrt{2\pi}\sigma} e^{\frac{-(ct-ct')^2}{2\sigma^2}} \right] \cdot {\rm eff}(ct) \tag{1}$$

$${\rm eff}(ct) = \begin{cases} 0 & \text{if } ct \le \beta_i \\ \sum_{i=1}^{3} N_i \cdot (ct-\beta_i)^2 \cdot e^{\frac{-ct}{\tau_i}} & \text{if } ct > \beta_i \end{cases} \tag{2}$$

- **Partially Reconstructed:** As they also come from $B_s$ mesons, the $D_sK$, $D_s\rho$, $D_s^*\pi$, and other partially reconstructed modes can contribute to the $B_s$ lifetime measurement. However, a multiplicative correction factor $K$ to the decay length is needed. The PR PDF

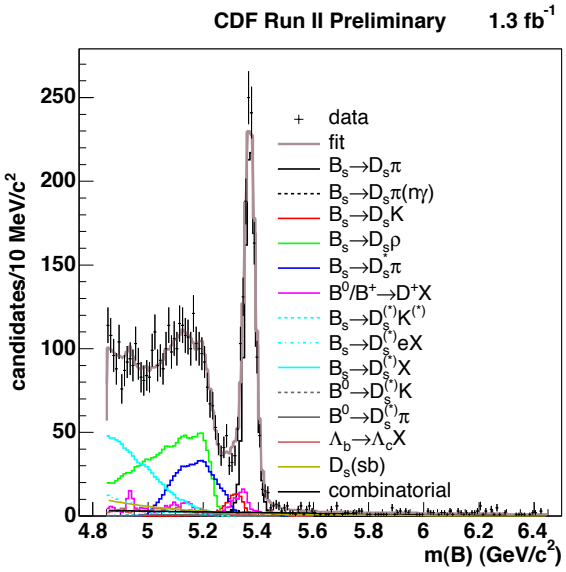


Figure 1: Mass distribution of events reconstructed as $B_s \to D_s^-(\phi\pi^-)\pi^+$ with fit projections overlaid.

given in Equation 3 is similar to the FR PDF with an additional convolution with the $K$ factor distribution for each mode. There are separate efficiency curve parameters for each mode, again determined from fits to simulation.

$$P_{\rm PR}(ct) = \left[\frac{1}{c\tau}e^{\frac{-ct'}{c\tau}} \otimes_{t'} \frac{1}{\sqrt{2\pi}K\sigma}e^{\frac{-(K\cdot ct-ct')^2}{2K^2\sigma^2}} \otimes_K p(K)\right] \cdot \text{eff}(ct) \qquad (3)$$

- **Background:** The backgrounds can either come from single-$B$ modes (*e.g.*, $B^0/B^- \to D^-X$, $B^0 \to D_sX$, and $\Lambda_b \to \Lambda_cX$), or they can be combinatorial in nature. There are two combinatorial background proxies available: the $B_s$ upper sideband taken from the $m_B$ interval [5.7, 6.4] GeV/$c^2$ and the $D_s$ sidebands. Both proxies contains a mixture of real $D_s$+track and fake $D_s$+track events. The background PDFs come from fits to simulated samples(for $b$-hadron backgrounds) or from the combinatorial background proxies. All the background shape parameters are fixed in the final lifetime fit.

## 3 Fit Results

The fit procedure was tested extensively on three control samples: $B^0 \to D^-\pi^+$ with $D^- \to K^+\pi^-\pi^-$, $B^0 \to D^{*-}\pi^+$ with $D^{*-} \to \overline{D}^0\pi^-$ and $\overline{D}^0 \to K^+\pi^-$, and $B^+ \to \overline{D}^0\pi^+$ with $\overline{D}^0 \to K^+\pi^-$ before performing a blinded $B_s$ fit. Good agreement with the PDG values of the $B^0$ and $B^+$ lifetimes was found.

The projection of the $B_s$ mass fit is shown in Figure 1. The lifetime of $c\tau_{B_s} = 455.0 \pm 12.2(\text{stat.})\mu$m is obtained from the full fit. The $ct$ projection of the fit result is plotted in Figure 2.

We consider several sources of systematic uncertainty: combinatorial background fraction, modeling simulated backgrounds from single-$B$ decays, effect of reweighting the Monte Carlo to match the data's $p_T$ and trigger distributions, impact parameter correlation, and detector alignment. The largest contribution to the systematic uncertainty comes from the uncertainty on the total amount of combinatorial background and the relative amount of promptly-produced real-$D_s$ background (the component with the lowest mean lifetime). The invariant mass shapes

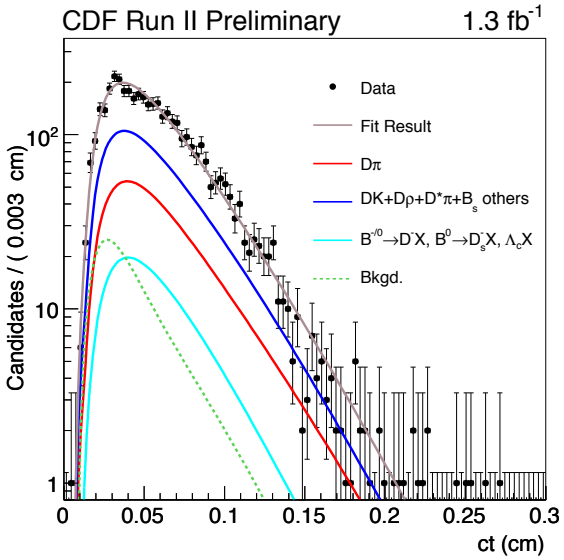


Figure 2: ct projection of lifetime fit results for events reconstructed as $B_s \to D_s^-(\phi\pi^-)\pi^+$

for the real-$D_s$ and fake-$D_s$ combinatorial backgrounds are very similar, and several mass fit configurations that are equally valid from first principles yield dissimilar background fractions. The variations in the fractions returned from these mass fits are used to evaluate the systematic uncertainty.

## 4 Conclusions

A fit for the $B_s$ lifetime in $\sim$1.3 fb$^{-1}$ of data reconstructed as $B_s \to D_s^-\pi^+$ is performed. The fit utilizes both fully and partially reconstructed modes. We measure

$$\begin{aligned} c\tau(B_s) &= 455.0 \pm 12.2(\text{stat.}) \pm 7.4(\text{syst.})\mu\text{m} \\ &= 1.518 \pm 0.041(\text{stat.}) \pm 0.025(\text{syst.})ps \end{aligned}$$

The ratio of this single result and the world average $B^0$ lifetime yields $\tau(B_s)/\tau(B_d) = 0.99 \pm 0.03$. This agrees well with the theoretical prediction of $\tau(B_s)/\tau(B_d) = 1.00 \pm 0.01$. More information about this analysis can be found on its public webpage. [4]

## References

1. F. Gabbiani, A. I. Onishchenko and A. A. Petrov, *Phys. Rev.* D **70**, 094031 (2004) [arXiv:hep-ph/0407004].
2. W.-M. Yao, *et al.* (Particle Data Group), *J. Phys.* G **33**, 1 (2006) and 2007 partial update for the 2008 edition.
3. D. Acosta, *et al.*, *Phys. Rev.* D **71**, 032001 (2005).
4. http://www-cdf.fnal.gov/physics/new/bottom/080207.blessed-bs-lifetime

# Searching for Higgs Decaying to $H \to WW^* \to \mu + \tau_{had}$ and $H \to WW^* \to ee$ at $D\emptyset$

Björn Penning
*Institute of Physics, Hermann-Herder-Str.3,*
*D-79104 Freiburg, Germany*

A search for the Higgs boson in $H \to WW^* \to ee$ and $H \to WW \to \mu\tau_{had}$ decays in $p\overline{p}$ collisions at a center-of-mass energy of $\sqrt{s} = 1.96$ TeV is presented. The data have been collected by the Run II $D\emptyset$ detector. In order to maximize the sensitivity multivariate techniques such as artificial neural networks (NN), matrix element methods and likelihoods are used. No excess above the *Standard Model* background is observed and limits on the production cross section times branching ratio $\sigma \times BR(H \to WW^* \to ee)$ for Higgs masses between 115 and 200 GeV are set.

## 1 Introduction

Two searches for the Higgs boson decaying to the $WW^*$ final state are presented. The dileptonic decay mode with two electrons in the final state and $H \to WW \to \mu + \tau_{had}^{1-prong}$ leading to final states with one muon, a jet originating from a hadronically decaying tau and missing transverse momentum have been studied. The $\mu + \tau_{had}$ analysis has been performed using an integrated luminosity of about $\sim 1$ fb$^{-1}$ of RunII data recorded between 2001 and 2006, known as RunIIa. The $ee$ analysis is performed using data from June 2006 until August 2007, known as RunIIb, corresponding to an integrated luminiosity of 1.2 fb$^{-1}$. These decay modes in combination with other dileptonic decay modes provide the best sensitivity to a Standard Model (SM) Higgs boson search at the Tevatron at a mass of $m_{\mathrm{H}} \sim 160\ GeV/c^2$ [1,2,3]. In order to maximize the signal to background separation multivariate techniques are used. If combined with searches exploiting the $WH$ and $ZH$ associated production, these decay modes increase the sensitivity for the Higgs boson searches.

## 2 Event Selection

The signal is characterized by two leptons, missing transverse momentum ($p_T$) and little jet activity. For the $\mu + \tau_{had}$ selection one isolated muon with $p_T^{\mu} > 12$ GeV and one isolated tau with $p_T^{\tau} > 10$ GeV are required. A hadronically decaying tau lepton is characterized by a narrow isolated jet with low track multiplicity. Three tau types are distinguished:

- $\tau$-type I: A single track with a calorimeter cluster without any electromagnetic subclusters (1-prong, $\pi$-like).
- $\tau$-type II: A single track with a calorimeter cluster and electromagnetic subclusters (1-prong, $\rho$-like).
- $\tau$-type III: Two or three tracks with an invariant mass below 1.1 or 1.7 GeV, respectively (3-prong).

Due to the large background contamination $\tau$-type III is neglected in the analysis.
For the dielectron analysis the leading electron is required to have $p_T^{e_1} > 20$ GeV and the trailing electron to fulfill $p_T^{e_2} > 15$ GeV. Subsequently most of the $QCD$ background is removed by selection requirements on the missing transverse energy $\not\!\!E_{\mathrm{T}}$ and the scaled missing transverse energy $\not\!\!E_T^{\mathrm{Scaled}}$ , defined as $\not\!\!E_T^{\mathrm{Scaled}} = \dfrac{\not\!\!E_{\mathrm{T}}}{\sqrt{\sum_{jets} \sigma^2_{E_T^j || \not\!\!E_{\mathrm{T}}}}}$, which is the $\not\!\!E_{\mathrm{T}}$ divided by the $\not\!\!E_{\mathrm{T}}$ resolution. This quantity is particularly sensitive to events where the missing energy could be a result of mismeasurements of jet energies in the transverse plane. A requirement on the minimal transverse mass, $M_T^{min} = \sqrt{2 \cdot \not\!\!E_{\mathrm{T}} \cdot p_T^l \cdot (1 - \cos(\Delta\phi))}$, between one of the leptons and $\not\!\!E_{\mathrm{T}}$ reduces further the various background processes. Most of the $\mathrm{Z}/\gamma^* \to \ell\ell$ events are rejected by requiring the sum of the momentum of $p_T^{\mu} + p_T^{\tau} + \not\!\!E_{\mathrm{T}}$ to be within given lower and upper boundaries and by requiring the invariant mass to be less than the $Z$ peak. The $\mathrm{t\bar{t}}$ contribution is reduced by requiring low values $H_T$ which is defined as the scalar sum of the transverse momenta of all jets in the event. A large fraction of remaining back-to-back $\mathrm{Z}/\gamma^* \to \ell\ell$ is reduced by rejecting events with a wide opening angle between the leptons. Since the signal kinematics change as a function of the Higgs mass the selection is applied in a mass dependent way.

## 3 $W + jet/\gamma$ and Multijet background estimation

The background contribution from QCD multijet production where jets are misidentified as leptons is estimated from the data by using like-sign lepton events of each analysis which were selected by inverting calorimeter isolation criteria[4]. The samples are normalized to data as function of the lepton $p_T^i$ $(i = 1, 2)$ in a region of phase space which is dominated by multijet production. In the $\mu + \tau_{had}$ analysis the shape of the $W + jet/\gamma$ background is taken from MC, the normalization however is estimated using data.

## 4 Multivariate Techniques

At the final stage of the selection as described in Section 2 the remaining background is dominated by electroweak $W + jets/\gamma$ and diboson production. To improve the background reduction further multivariate techniques have been used, in the $\mu\tau_{had}$-analysis a likelihood approach and for the $ee$ final state artificial neural networks. For the likelihood approach two different likelihoods sensitive to different event properties are used. One likelihood is based on input distributions associated with the selected tau and the second one on kinematical properties of the particular event. All likelihoods are constructed according to formula (1). A non-negligible

fraction of the tau-candidates are electrons misreconstructed as taus which is taken into account by further constructing both classes of likelihoods for that particular events.

$$\mathcal{L} = \frac{\mathcal{P}_{Sig}(x_1, x_2, \ldots)}{\mathcal{P}_{Sig}(x_1, x_2, \ldots) + \mathcal{P}_{Bkgd}(x_1, x_2, \ldots} \approx \frac{\prod_i \mathcal{P}^i_{Sig}}{\prod_i \mathcal{P}^i_{Sig} + \prod_i \mathcal{P}^i_{Bkgd}} = \frac{\prod_i \mathcal{P}^i_{Sig}/\mathcal{P}^i_{Bkgd}}{\prod_i \mathcal{P}^i_{Sig}/\mathcal{P}^i_{Bkgd} + 1} \quad (1)$$

Where $\mathcal{P}^i_{Sig}$ represents the signal and $\mathcal{P}^i_{Bkgd}$ the background value for a given bin $i$. The value of the input distributions for bin $i$ are given by the variables $x_i$. $\mathcal{P}^i_{Sig} \equiv \mathcal{P}_{Sig}(x_i)$ and $\mathcal{P}^i_{Sig} \equiv \mathcal{P}_{Sig}(x_i)$ represents the probability density functions for the topological variables. These likelihoods are constructed for each Higgs boson mass point and both tau-types. The resulting likelihood distribution for $m_{\mathrm{H}} = 160$ GeV and tau-type I is displayed in Fig. 1. Using both likelihood classes a further selection requirement is applied. These selections have been optimized for each sample, tau type and Higgs mass. For the dielectron analysis the separation of signal from background is done using an artificial neural network. A separate NN is trained for each Higgs boson mass tested. A list of input variables has been derived based on the separation power of the various distributions. Those variables can be divided into three classes, object kinematics, event kinematics and angular variables. An additional input variable is a discriminant constructed using the matrix element (ME) method. Leading-order parton states for either signal or $WW$ background are integrated over, with each state weighted according to its probability to produce the observed measurement.

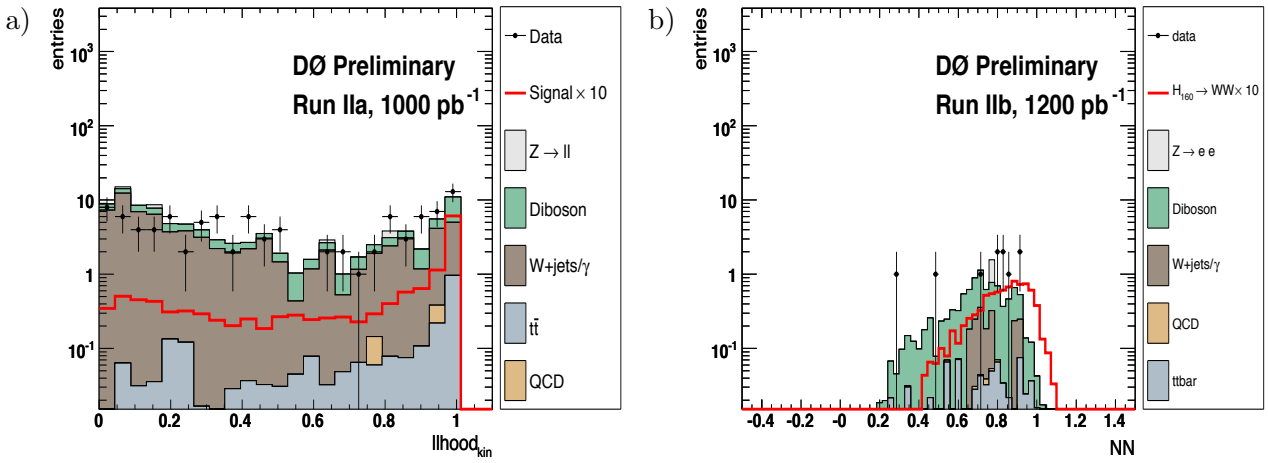


Figure 1: Distribution of (a) the kinematical likelihood distribution after all selection requirements (b) the neural network ouput after all selection requirements for data (points with error bars), background simulation (histograms, complemented with the QCD expectation) and signal expectation for $m_H = 160$ GeV (empty histogram).

The various signal contributions $H \to WW \to ee$ and $H \to WW \to \mu\tau_{had}$ are given by the solid red line.

## 5 Results and Conclusion

Limits on the cross section for Higgs boson production times the branching fraction into the discussed final states are derived at the 95% Confidence Level (CL). Whereas the number of expect signal events, expected background events and observed data is used in the $\mu + \tau_{had}$ analysis, for the dielectron analysis the shape of the NN output distributions are taken into account as well.

There are various sources of systematic uncertainties included in the calculation of the expected and observed limits: Lepton identification and reconstruction efficiencies (0.3–13%), trigger efficiencies (5%), jet energy scale calibration in signal and background events($< 2\%$),

track momentum calibration (4%), detector modeling (1% for signal, 5-10% for background), PDF uncertainties (4%), modeling of multijet background (30%) and theoretical cross section (di-boson 7%, $t\bar{t}$ 16%). The uncertainty on the modeling of the electroweak $W + jet/\gamma$ production has been estimated to be 2.5-17.5%. The systematic uncertainty on the luminosity is mainly a combination of the PDF uncertainty, uncertainty on the NNLO Z cross section (4%) and data/MC normalization.
The total uncertainty on the background is approximately 20% and for the signal efficiency is 10%. The effects of these uncertainties on the NN output distribution shapes were also studied and included as additional systematic uncertainties. The expected and observed limits as function of the Higgs mass are shown in Fig. 2. After all selection requirements both the neural network output distribution and the likelihood distributions agree with data within their uncertainties with the expected backgrounds. Thus limits are set on the production cross section times branching ratio $\sigma \times BR(H \rightarrow WW^*)$. We calculate the limits for each channel using a modified frequentist approach CLs method with a log-likelihood ratio (LLR) test statistic. To minimize the degrading effects of systematics on the search sensitivity, the individual background contributions are fitted to the data observation by maximizing a profile likelihood function for each hypothesis [5].

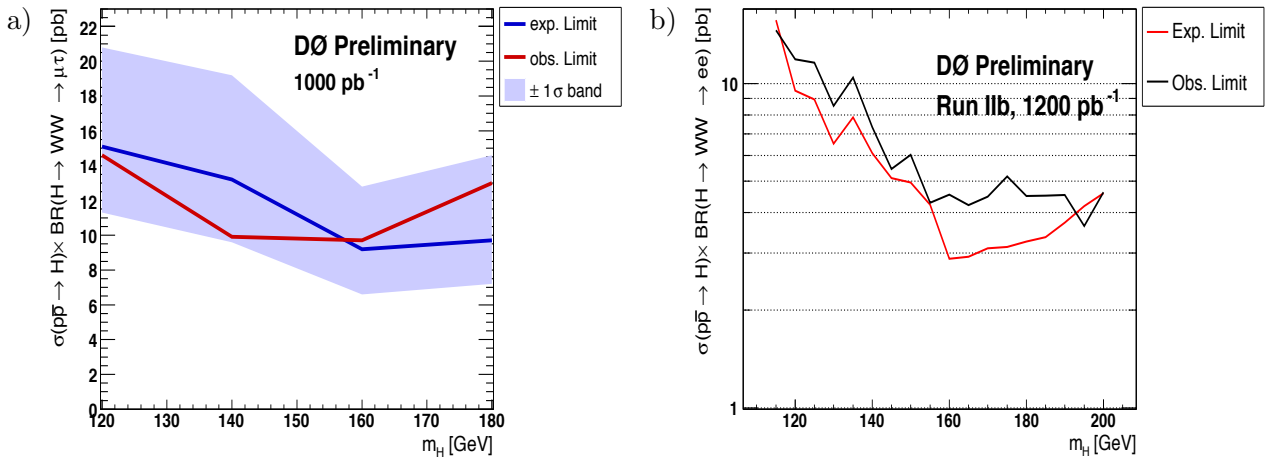


Figure 2: (a) Expected and observed limit for the $\mu + \tau_{had}$ analysis (b) Expected and observed limit for the dielectron analysis

A search has been performed for the $H \rightarrow WW \rightarrow \ell\ell$ decay signature from the gluon-gluon fusion production of the Standard Model Higgs boson in leptonic channels with either muons and taus or two electrons, using data corresponding to an integrated luminosity altogether of $\approx$ 2.2 fb$^{-1}$. No evidence for the Higgs particle is observed and no region of the SM Higgs can be excluded.

## References

1. T. Hao, A. Turcot, R-J. Yang, Phys. Rev. D. 59, 093001 (1999).
2. M. Carena *et al.* [Higgs Working Group Collaboration], "Report of the Tevatron Higgs working group", hep-ph/0010338.
3. K. Jakobs, W. Walkowiak, ATLAS Physics Note, ATL-PHYS-2000-019.
4. Search for $H \rightarrow WW \rightarrow$ dileptons, 300-325 pb$^{-1}$, hep-ex/0508054
5. M.L. Mangano, M. Moretti, F. Piccinini, R. Pittau, A. Polosa, hep-ph/0206293.

# SEARCH FOR WMAP-COMPATIBLE SIMPLE $SO(10)$ SUSY GUTs

SEZEN SEKMEN
*Department of Physics, Middle East Technical University,*
*TR-06531, Ankara, Turkey*

Unification of GUT-scale $t-b-\tau$ Yukawa couplings is a significant feature of simple $SO(10)$ SUSY GUTs. Here we present the results of a search that used the Markov Chain Monte Carlo technique to investigate regions of Yukawa unification and WMAP-compatible dark matter relic density in $SO(10)$-like MSSM parameter spaces. We mention the possible LHC signatures of Yukawa unified scenarios and discuss the consequences for dark matter.

## 1 Introduction

Grand Unification is regarded as an inspirational ingredient of models that claim to explain the fundamental laws of nature. A highly motivated scenario in this context originates from grand unification via the $SO(10)$ gauge group [1]. Simple supersymmetric implementations of $SO(10)$ GUTs unify all matter fields in each generation within a 16-dimensional irreducible representation and two Higgs doublets of the MSSM within a 10-dimensional irreducible representation. Such a formalism automatically includes heavy right-handed neutrino states and the resulting structure of the neutrino sector implies a successful theory of baryogenesis via intermediate scale leptogenesis. Moreover the $SO(10)$ models are left-right symmetric and this enables them to provide a solution to the strong CP problem and to naturally induce R-parity conservation.

Besides gauge coupling unification, $SO(10)$ SUSY GUTs additionally require the unification of 3rd generation Yukawa couplings at the GUT scale ($M_{GUT}$). This is explicitly seen from the expression of the superpotential above $M_{GUT}$, which takes the form $\hat{f} \ni f\hat{\psi}_{16}\hat{\psi}_{16}\hat{\phi}_{10} + \cdots$. An exact unification occurs at tree level while several percent corrections arise at the loop level. As a result we can assume that any sign of Yukawa unification from observations could be a hint to the existence of $SO(10)$ SUSY GUTs.

Our aim in the study is to investigate the characteristics that arise in a SUSY model when GUT scale Yukawa unification is imposed and to determine the experimental signatures that would distinguish such Yukawa-unified models from the others. In this context we assume a theoretical framework where nature is explained by an $SO(10)$ symmetry above $M_{GUT}$. Then at $M_{GUT}$, $SO(10)$ breaks to MSSM plus some heavy right-handed neutrino states. At the weak scale, the content of the theory is equivalent to that of the MSSM.

The GUT scale soft SUSY breaking parameters are constrained by the requirement of the $SO(10)$ symmetry. Unified representations would favor common SSB masses "$m_{16}$" for the scalars and "$m_{10}$" for the Higgses, but in order to achieve REWSB, SSB Higgs masses should be split, satisyfing $m_{H_d} > m_{H_u}$. Here we examine two different methods to generate the necessary Higgs splitting: The first approach defines the Higgs masses as $m^2_{H_{u,d}} = m^2_{10} \mp 2M^2_D$. Here splitting is parametrized by $M_D$, which is the magnitude of the D-terms in the scalar potential

of the extra $U(1]$ group that is a by-product of the $SO(10)$ breaking. The parameters of this GUT scale Higgs input (GSH) scenario are

$$m_{16},\, m_{10},\, M_D^2,\, m_{1/2},\, A_0,\, \tan\beta,\, sgn(\mu) \tag{1}$$

The socond approach was put forward in order to generate Yukawa unified solutions with low $\mu$ parameter and low $m_A$. Such solutions were found to exist by Blaszek, Dermisek and Raby at a study where they assumed perfect Yukawa unification at $M_{GUT}$ and made a fit to the weak scale observables [2]. In order to seek similar solutions, we start with GSH parameters at GUT scale, but additionally provide $\mu$ and $m_A$ as inputs. We run $m_{H_{u,d}}$ down, and at $Q = M_{SUSY}$ we compute what $m_{H_u}$, $m_{H_d}$ should have been in order to give our input $\mu$ and $m_A$, and run back up using these new boundary conditions. This weak scale Higgs (WSH) scenario has the parameters

$$m_{16},\, m_{10},\, M_D^2,\, m_{1/2},\, \tan\beta,\, m_A,\, \mu \tag{2}$$

We take the GSH and WSH scenarios and search in their parameter spaces for regions having a good Yukawa unification where Yukawa unification is parametrized by $R = \frac{max(f_t,f_b,f_\tau)}{min(f_t,f_b,f_\tau)}$. Additionally we seek sub-regions that are consistent with the WMAP measurements of dark matter relic density $\Omega h^2$ [3]. There have been previous searches using the GSH input based on random scans and they were able to achieve less than few percent of Yukawa unification for $\mu > 0$ [4]. However the dark matter relic densities for these solutions were always much higher than the WAMP upper bound. Here we implement the Markov Chain Monte Carlo (MCMC) technique which enables a much more efficient scanning of multi-dimensional parameter spaces. The following two sections summarize the MCMC technique, the characteristics of the regions found by utilizing it, and dark matter-related consequences of the $SO(10)$ SUSY GUTs.

## 2 The MCMC Search and the Yukawa-unified Solutions

A Markov Chain is a discrete time, random process where given the present state, the future state only depends on the present state, but not on the past states [5]. The MCMC samples from a given parameter space as follows: It takes a starting point, and it generates a candidate point $x^c$ from the starting point $x^t$ using a proposal density $Q(x^t; x^c)$. The candidate point is accepted to be the next state $x^{t+1}$ if the ratio $p = \frac{P(x^c)Q(x^t;x^c)}{P(x^t)Q(x^c;x^t)}$ (where $P(x)$ is the probability calculated for the point $x$) is greater than a uniform random number $a = U(0,1)$. If the candidate is not accepted, the present point $x^t$ is retained and a new candidate point is generated. By repeating this procedure continuously the Markov Chain eventually converges at a target distribution around a point with the highest probability.

Our MCMCs were directed to approach regions with $R \sim 1.0$ and $0.094 \leq \Omega h^2 \leq 0.136$. Here we used a Gaussian distribution for the proposal density $Q$, and approximated the likelihood of a state to $e^{-\chi^2_{R,\Omega}}$. We also chose multiple starting points ($\sim 10$) in order to search a wider range of the parameter space. We used `ISAJET 7.75` for sparticle mass computations and `micrOMEGAs 2.0.7` for DM relic density calculations. The MCMCs successfully located some regions with good $R$ and $\Omega h^2$. Here we will mostly emphasize the results from the GSH scenario.

Figure 1 shows the compatible regions in $m_{16} - m_{10}$ and $m_{16} - m_{16}/A_0$ planes. The light blue dots have $R \leq 1.1$, the dark blue dots have $R \leq 1.05$, the orange dots have $R \leq 1.1$ plus $\Omega h^2 \leq 0.136$ and the red dots have $R \leq 1.05$ plus $\Omega h^2 \leq 0.136$. We see that Yukawa unification occurs only at the regions where the input parameters are strongly correlated, having $m_{10} \simeq 1.2 m_{16}$ and $A_0 \simeq -(2 - 2.1) m_{16}$. A good DM relic density is achieved only at the constrained regions that have $m_{16} \sim 3 - 4$ TeV. Further search showed that $m_{1/2}$ takes the lowest possible values for a given $m_{16}$, generally giving $\sim 100$ GeV, and decreases steadily with increasing $m_{16}$.

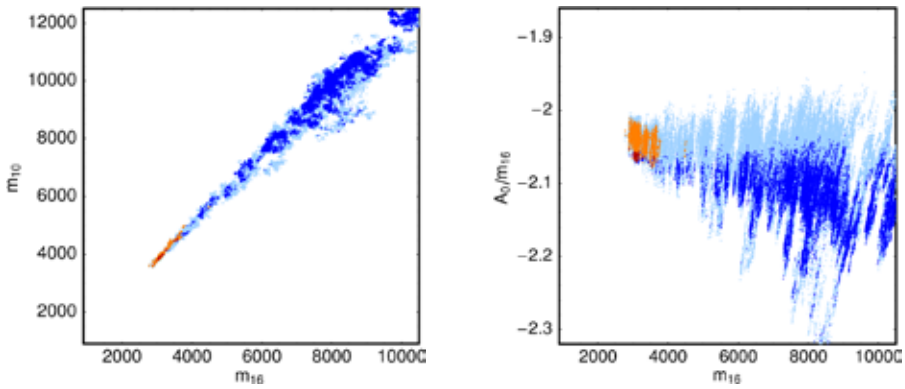


Figure 1: Yukawa-unified GSH points found by MCMC in the $m_{10}$ vs. $m_{16}$ plane (left) and the $A_0/m_{10}$ vs. $m_{16}$ plane (right); the light-blue (dark-blue) points have $R < 1.1$ (1.05), while the orange (red) points have $R < 1.1$ (1.05) plus $\Omega h^2 < 0.136$.

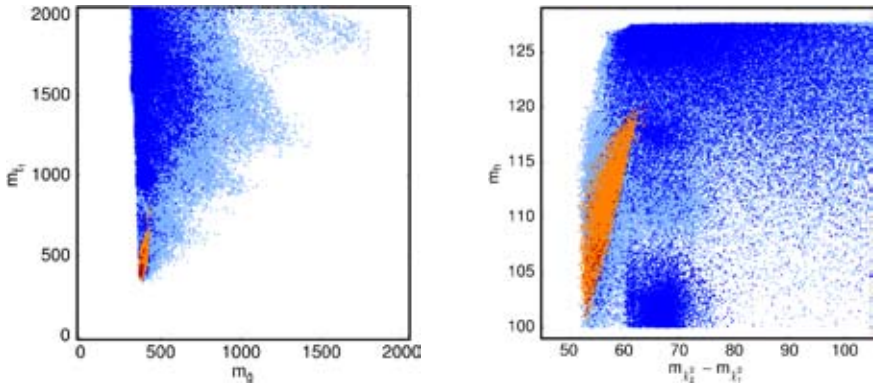


Figure 2: Yukawa-unified GSH points found by MCMC in the $m_{\tilde{t}_1}$ vs $m_{\tilde{g}}$ plane (left) and $m_{h^0}$ vs. $m_{\tilde{\chi}_2^0} - m_{\tilde{\chi}_1^0}$ plane (right); color code as in Figure 1.

These highly confined parameter regions lead to strongly constrained mass spectra, and hence to significant LHC signatures. We see that Yukawa-unified solutions are distinguished by their heavy 1st/2nd generation scalars ($> 2$ TeV), lighter 3rd generation scalars ($\sim$TeV) and light gauginos (few hundred GeV). All Higgses except $h^0$ are about $1-3$ TeV. Figure 2 shows the distribution of selected points on $m_{\tilde{t}_1}$ vs $m_{\tilde{g}}$ plane (left), and on $m_{h^0}$ vs $m_{\tilde{\chi}_2^0} - m_{\tilde{\chi}_1^0}$ plane (right) for the GSH scenario. The requirement of $\Omega h^2 < 0.136$ favors a gluino mass range around $350-450$ GeV, which means we would expect a large amount of gluino pair production at the LHC with cross sections about $\sim 100$ pb. The gluinos decay via 3-body channels such as $\tilde{g} \to \tilde{\chi}_1^0 b\bar{b}, \tilde{\chi}_2^0 b\bar{b}, \tilde{\chi}_1^{\pm} t\bar{b}/b\bar{t}$, since 2-body channels are closed due to the high squark masses. On the other hand favored $\tilde{\chi}_2^0 \simeq \tilde{\chi}_1^{\pm}$ mass range is $100-150$ GeV, which leads to gaugino pair production cross sections about $\sim 10$ pb, while $m_{\tilde{\chi}_1^0} \sim 50-75$ GeV. The preferred mass difference $m_{\tilde{\chi}_2^0} - m_{\tilde{\chi}_1^0}$ is $52-65$ GeV which is smaller than $m_{Z,h^0}$, therefore $\tilde{\chi}_2^0$ decays are dominated again by 3-body channels as $\tilde{\chi}_2^0 \to b\bar{b}\tilde{\chi}_1^0, q\bar{q}\tilde{\chi}_1^0, l\bar{l}\tilde{\chi}_1^0$.

As a result we expect the $SO(10)$ models to manifest themselves as multi b-jet plus low missing $E_T$ final states at the LHC. Additionally it would be possible to investigate the OS/SF dilepton channels where the dilepton invariant mass is bound by $m_{\tilde{\chi}_2^0} - m_{\tilde{\chi}_1^0}$ and try to reconstruct the $\tilde{g} \to b\bar{b}\tilde{\chi}_2^0 \to b\bar{b}l\bar{l}\tilde{\chi}_1^0$ cascades.

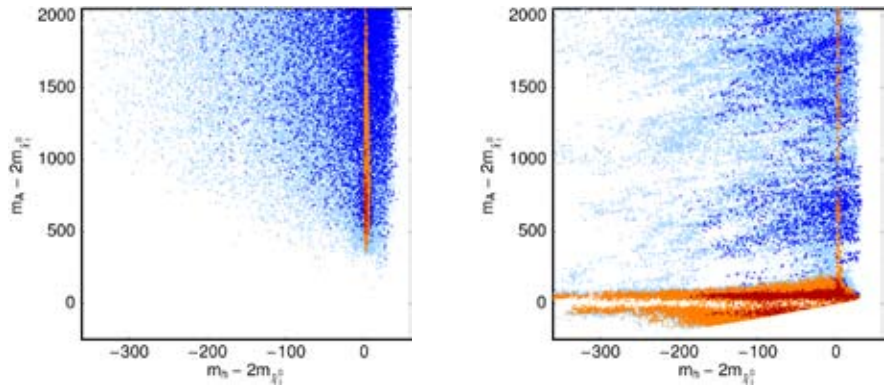


Figure 3: Yukawa-unified points found by MCMC on the $m_A - 2m_{\tilde{\chi}_1^0}$ vs. $m_{h^0} - 2m_{\tilde{\chi}_1^0}$ plane for GSH (left) nd WSH (right) scenarios; color code as in Figure 1.

## 3 Consequences for Dark Matter

The majority of solutions shown in Figures 1 and 2 have excess DM relic density, while only a small portion of them gives $\Omega h^2 < 0.136$. To investigate the mechanism that provides the efficient annihilation in the DM-allowed solutions, we check the behavior of solutions in $m_{h^0}$ and $m_A$ mass resonances. Figure 3 shows the distribution of Yukawa-unified points on the $m_A - 2m_{\tilde{\chi}_1^0}$ vs. $m_{h^0} - 2m_{\tilde{\chi}_1^0}$ plane for GSH (left) and WSH (right) scenarios. In the GSH plot all DM-allowed solutions are on the $m_{h^0} \simeq 2m_{\chi_1^0}$ line, which shows that the relic density is reduced by annihilation via a light Higgs resonance. On the other hand $m_A > 2m_{\tilde{\chi}_1^0}$, so there are no A resonance solutions. Turning to the WSH scenario we see that annihilation via both $h^0$ and A resonances are at work. Actually the majority of solutions are generated by the latter due to the relatively small A masses allowed within the WSH scenario. However all of these solutions have $B_s \to \mu\mu$ branching ratios higher than the latest reported CDF upper limit $5.8 \times 10^{-8}$. So these A resonance points are ruled out, leaving us with only the $h^0$ resonance solutions.

One could also devise alternative methods for reducing the excess DM relic density. One way could be to assume that $\tilde{\chi}_1^0$ is not the LSP, but can decay to other candidates such as gravitino or axino via the mode $\tilde{\chi}_1^0 \to \gamma\tilde{G}/\tilde{a}$. Lifetime of $\tilde{\chi}_1^0$ would be long enough to let it escape the detectors. The resulting relic density would be $\Omega_{\tilde{G},\tilde{a}} = (m_{\tilde{G},\tilde{a}}/m_{\tilde{\chi}_1^0})\Omega_{\tilde{\chi}_1^0}$ since the $\tilde{G}s/\tilde{a}s$ inherit the thermally produced neutralino relic number density. $\tilde{G}$ LSP can only reduce the relic density a few times, which is not satisfactory for our case, but axinos with $m_{\tilde{a}} \leq 1$ MeV would allow for a mixed cold/warm DM solution which can reduce the relic density below the WMAP bound [6].

Another method to reconcile $\Omega h^2$ is to relax some universalities in the GUT scale SSB terms. For example, increasing the $U(1)$ gaugino mass term $M_1$ (while keeping $M_{2,3} = m_{1/2}$) brings $m_{\tilde{\chi}_1^0}$ close to $m_{\tilde{\chi}_1^\pm}$, hence making $\tilde{\chi}_1^0$ more wino-like and inducing bino-wino coannihilation. A further possibility is to lower the 1st/2nd generation masses $m_{16}(16)$ (while keeping $m_{16}(3) = m_{16}$), which enables neutralinos to annihilate via light $\tilde{q}_R$ exchange and leads to neutralino-squark coannihilation.

## 4 Conclusions

By performing scans on the parameter space of simple $SO(10)$ SUSY GUT scenarios using the MCMC technique, we showed that solutions with both $5-10\%$ Yukawa unification and WMAP-compatible $\Omega h^2$ can exist around $m_{16} \sim 3-4$ TeV. These regions defined by strictly constrained relations among the GUT scale inputs generate special sparticle mass relations that lead to distinguishable signatures at the LHC. With multi-TeV scalars, $350 - 450$ GeV gluinos and

$50 - 150$ GeV light gauginos, we expect dominant gluino production followed by 3-body cascade decays which will end up in b-rich multijet final states, occasionally including OS/SF lepton pairs from $\tilde{\chi}_2^0$ decays. Moreover the possibility to lower $\Omega h^2$ by assuming $\tilde{a}$ LSP or introducing SSB non-universalities marks wider parameter space regions as compatible. So we can conclude that $SO(10)$ SUSY GUTs provide motivated scenarios with robust signatures relevant to be tested soon at the turn-on of the LHC.

**Acknowledgments**

I thank the organizers of XLIIIrd Rencontres de Moriond for a fulfilling conference and gratefully acknowledge the financial support by the EU Marie Curie Actions project.

**References**

1. H. Georgi, in *Proceedings of the American Institue of Physics*, ed. C. Carlson (1974); H. Fritzsch and P. Minkowski, *Ann. Phys.* **93**, 193 (1975); M. Gell-Mann, P. Ramond and R. Slansky, *Rev. Mod. Phys.* **50**, 721 (1978). For recent reviews, see R. Mohapatra, hep-ph/9911272 (1999) and S. Raby, *Rept. Prog. Phys.* **67**, 755 (2004).
2. T. Blazek, R. Dermisek and S. Raby, *Phys. Rev. Lett.* **88**, 111804 (2002); T. Blazek, R. Dermisek and S. Raby, *Phys. Rev.* D **65**, 115004 (2002).
3. H. Baer, S. Kraml, S. Sekmen and H. Summy, *JHEP* **0803**, 056 (2003)
4. D. Auto, H. Baer, C. Balazs, A. Belyaev and J. Ferrandis and X. Tata, *JHEP* **0306**, 023 (2003); D. Auto, H. Baer, A. Belyaev and T. Krupovnickas, *JHEP* **0410**, 066 (2004).
5. A. A. Markov, *Extension of the limit theorems of probability theory to a sum of variables connected in a chain*, reprinted in Appendix B of: R. Howard, *Dynamic Probabilistic Systems, volume 1: Markov Chains*, John Wiley and Sons, 1971.
6. H. Baer and H. Summy, arXiv:0803.0510.

# TOWARDS AN ESTIMATION OF THE MUON MULTIPLICITY IN ANTARES

C. PICQ
*CEA Saclay/IRFU/SPP, 91191 Gif-Sur-Yvette, France*
*Laboratoire APC Paris 7, Bâtiment Condorcet*
*10 rue Alice Domon et Lonie Duquet, 75205 Paris Cedex 13, France*

Antares in an underwater neutrino telescope under completion in the Mediterranean Sea. The telescope consists of a 3D network of photomultipliers able to detect the Cherenkov light emitted by relativistic charged particles. From January to December 2007 the Antares detector was composed of 5 lines and since December $7^{\text{th}}$ 2007, it comprises 10 lines. The 12 line detector is being completed in 2008. In this paper we present a study with Monte-Carlo and data to estimate the muon multiplicity of atmospheric bundles, which are the most intense source of background to the signal of up-going muons.

## 1 Introduction

Antares is a high energy neutrino telescope located at 40 km off Toulon. The main goal of Antares is to detect neutrinos as a new probe to study the sky at energies greater than 1 TeV. Neutrinos are indeed neither deflected by the magnetic fields, nor absorbed by the interstellar dust. This enables them to travel on cosmological distances through the Universe. They can also emerge from regions of very high matter density, bringing us information on the core of astrophysical objects where catastrophic phenomena can happen. This work describes the characterization of atmospheric muons bundles which are the most intense background for neutrino detection.

## 2 Detection method

High energy cosmic muon neutrinos can interact with the surrounding detection medium and produce a muon. In water this muon travels faster than light and emit Cherenkov light in a cone whose angle is defined by:

$$\cos\theta = \frac{1}{\beta n} \Rightarrow \theta \approx 42^{\circ}$$

Antares detects this dim light with a three-dimensional network of photomultipliers housed in glass spheres (called Optical Modules - OM).

Antares is installed at 2475 m depth. The final detector is constituted of 12 vertical lines, measuring 450 m of which 350 m are instrumented. Lines lay 60 m apart from each other. Each line is connected to a junction box through an interlink cable and the junction box is connected to shore via a 40 km long electro-optic cable for power and data transmission. The lines are composed of 25 floors of 3 optical modules each pointing downwards at 45° from the vertical [1].

The Antares PMT network is optimized to look downwards, i.e. to detect upward-going muons induced by neutrinos that have interacted in the Earth. Contrarily to these neutrinos, muons originating from atmospheric showers cannot travel through the Earth.

Because of the weak cross section and the low emission flux of the sources, few cosmic neutrinos are expected to be detected. This small signal has to be disentangled from two kinds of physical backgrounds:
Up-going atmospheric neutrinos created by interaction of primary cosmic rays in the atmosphere which can interact near the detector, giving an up-going muon.
Down-going muons that are sometimes mis-reconstructed as up-going ones. Due to the intensity of the atmospheric muon flux, this remains as the most intense source of background.

In this analysis, we will focus on the muon multiplicity, defined as the number of muons crossing the detector simultaneously, as a possible variable to reject this background. In our simulation, a "muon" is further considered as such if it produces at least 6 hits (minimum requisite for the reconstruction) in the detector.

## 3 Goal of the multiplicity study

When a primary cosmic ray (mostly proton) collides with a nitrogen or an oxygen nucleus, it produces an atmospheric cascade of secondary particles (called "shower" or "bundle" of particles), as illustrated in figure 1. During its development, the shower produces charged mesons which decay into muons and neutrinos.

Produced muons propagate to the sea level. Only the most energetic ones (E> 500 GeV) can go through more than two kilometres of water and reach the detector. As shown in figure 2, the down-going flux is dominated by the atmospheric muons by six orders of magnitude compared to the muons from the atmospheric neutrinos, for muon energies above 1 TeV at the detector.

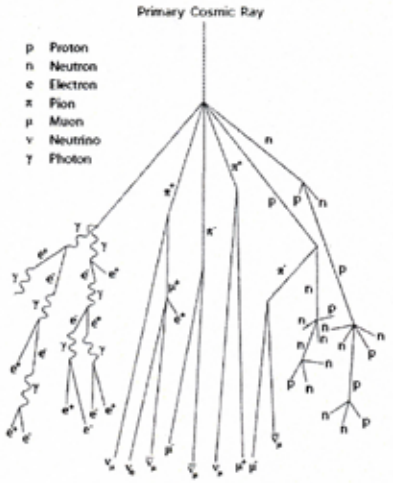


Figure 1: Bundle of secondary particles produced by a cosmic ray interaction.

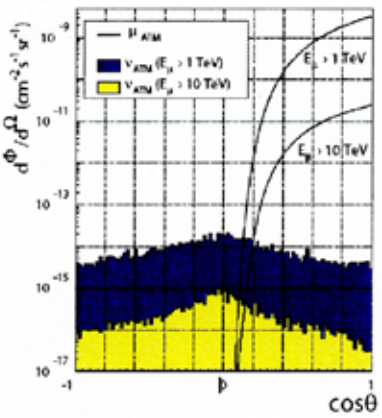


Figure 2: Muon flux versus zenith angle. $\cos\theta = 1$ represents the down-going muons ans $\cos\theta = -1$ the up-going muons.

The reconstruction algorithm used in the Antares data analysis is optimised for a single (up-going) muon passing through the detector. However 90% of the down-going events comprise several muons (see muon multiplicity in figure 3). These down-going multi-muons can produce some tricky effects in the reconstruction and in the understanding of the detector. This study is an attempt to separate single muons from multi-muons using appropriate variables with the aim of studying multi muon effects in the detector. Muon multiplicity depends on the primary energy and the thickness of water that the muons traverses (i.e. the incidence angle). Multi-muon events, when reconstructed as a single muon, are expected to produce bad quality fits. The study presented here is based on a variable relying on the time residuals after reconstruction.

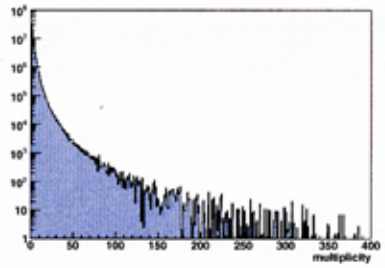


Figure 3: Multiplicity distribution in the 5 line detector. A muon has to give at least 6 hits to be considered as a physical muon.

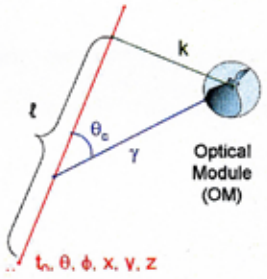


Figure 4: Schematic view of the kinematics related to the photon arrival time on the OM. The red line represents the muon, while the blue line represents the photon.

## 4 Method

As illustrated in figure 4, the muon propagates in a straight line at the speed of light (in vacuum). The arrival time of a direct Cherenkov photon at the optical module is determined by [2]:

$$t_{\text{direct}} = t_0 + \frac{1}{c}\left(l - \frac{k}{\tan\theta_C}\right) + \frac{1}{v_g}\left(\frac{k}{\sin\theta_C}\right) \quad (1)$$

where $v_g$ is the group speed of light in water, $t_0$, x, y , z define an arbitrary point on the muon trajectory, $l$ and $k$ are defined in figure 4 and $\theta_C$ is the Cherenkov angle. The first term in equation (1) accounts for the muon travel time, from $t_0$ to the moment when it emits a detectable Cherenkov photon, while the last term represents the time needed by this photon to reach in a straight line the photomultiplier. Photons can however diffuse in the water before hitting a photomultiplier, this diffusion inducing some delay with respect to a direct hit. Moreover at high energy (above $\approx 500$ GeV) the muon energy loss begins to be dominated by catastophic losses producing secondary electromagnetic showers. These particles produce additional Cherenkov light leading to further delays. These delays create larger time residuals, defined as the difference between the arrival time on the photomultiplier and the computed hit time of a direct photon emitted by the reconstruced muon.

If a bundle of muons distant from each other by a few meters is reconstructed as a single muon, the time residual distribution will be broader than the one of isolated single muons. Therefore we introduce the variable Small Residual Fraction (SRF) which is the ratio of the number of hits with time residuals between $-5$ ns and 5 ns over the number of hits with residuals between $-50$ ns and 100 ns.

## 5 Analysis

The simulation was done using the CORSIKA[3] code for a 5-line detector.

The time residual distribution is shown in figure 5. As expected, the peak is narrower for single muons than for multi muons. The mean value of SRF is 0.39 (figure 6). For single muons it is 0.46 and is smaller for multi-muons. The single muon content increases with a cut on SRF, as shown in figure 7. For example with SRF$> 0.5$, we have 36.2% of single muons contaminated by 4.45% of multi-muons. The mean multiplicity decreases from 2.8 to 1.3 and single muons represent 53% of the muons in the events. Fig. 8 shows a comparison of the SRF distribution between the Monte-Carlo sample and one month of real data (June 2007 - 18 days effective live time). By comparing with an other Monte-Carlo[4], we find that one reason of disagreement is that the multiplicity of Corsika is lower than the observed one in data.

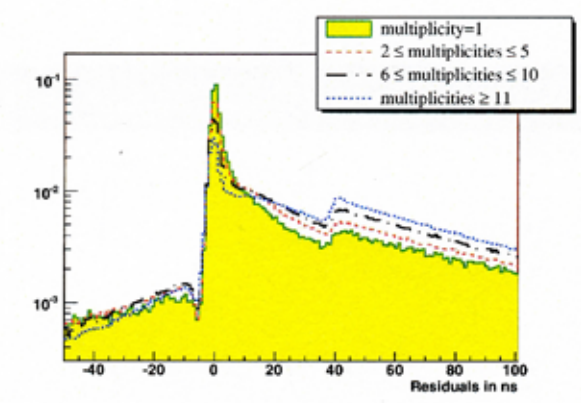


Figure 5: Time Residual distribution for different ranges of multiplicities

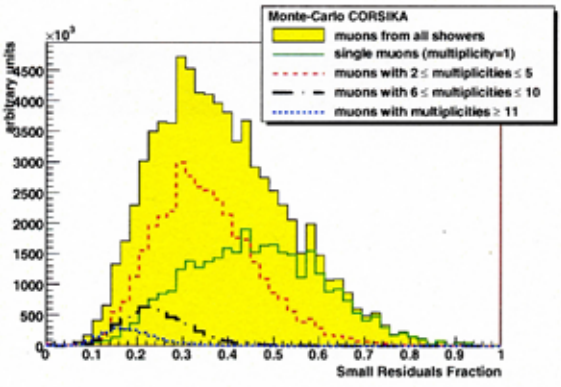


Figure 6: Small Residual Fraction distribution for all multiplicities and for ranges of multiplicities

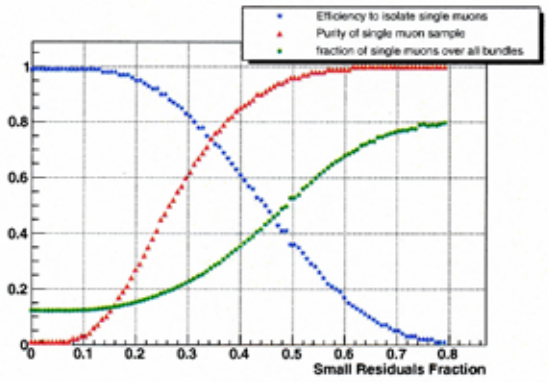


Figure 7: Efficiency, purity and composition of lower SRF cut.

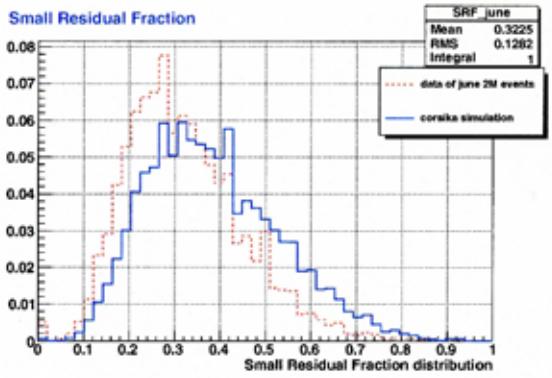


Figure 8: Small Residual Fraction distribution for data (red dotted line) and simulation (blue line)

## 6 Conclusion

In Antares, the neutrino signal is polluted by a fraction of the muons coming from atmospheric bundles. In this study we have shown that using a simple discriminating variable based on time residuals, the single muon sample can be substantially enriched. We increase the purity of the single muon sample and decrease the mean multiplicity. The separation of single from multiple muons allows a better understanding of reconstruction and event selection.

## References

1. P.Amram et al., "The ANTARES optical module" Nucl. Instr. and Methods A484 (2002) 369
2. Antares Collaboration Proceedings of ICRC 2007, arXiv:0711.2683v1 [astro-ph]
3. D. Heck, J. Knapp, J.N. Capdevielle, G. Schatz, T. Thouw, Forschungszentrum Karlsruhe Report FZKA 6019 (1998)
4. G. Carminati, A. Margiotta, M. Spurio, "Atmospheric MUons from PArametric formulas: a fast GEnerator for neutrino telescopes(MUPAGE)" to be published in Computer Physics Communications, arXiv:0802.0562 [physics.ins-det]

# Coincidence analysis in ANTARES: Potassium-40 and muons

D. Zaborov on behalf of the Antares collaboration
*Institute for Theoretical and Experimental Physics*
*Moscow, 117218, Russia*

A new calibration technique using natural background light of sea water has been recently developed for the ANTARES experiment. The method relies on correlated coincidences produced in triplets of optical modules by Cherenkov light of $\beta$ particles originated from $^{40}$K decays. A simple but powerful approach to atmospheric muon flux studies is currently being developed based on similar ideas of coincidence analysis. This article presents the two methods in certain detail and explains their role in the ANTARES experiment.

## 1 Introduction

ANTARES is a large water Cherenkov detector operating in Mediterranean sea 40 km offshore Toulon (France) at the depth of 2470 m.[1,2] An ANTARES storey includes a triplet of optical modules[3] oriented at $45^o$ downwards and outwards of the vertical axis. Twenty five storeys, chained together with a step of 14.5 m, form a detector line. Several calibration systems and techniques ensure a sub-nanosecond precision of the Cherenkov pulse measurements, which is required to achieve the high angular resolution of the neutrino telescope. Important roles are played by in situ measurements using LED Beacons[4] and Potassium-40.

Potassium-40 is a $\beta$-radioactive isotope naturally present in sea water. The energy freed in $^{40}$K decays amounts to 1.3 MeV, that well exceeds Cherenkov threshold for electrons in water (0.26 MeV) and is sufficient to produce up to 150 Cherenkov photons. If the decay occurs in the vicinity of a detector storey, a coincident signal may be seen by two of the three optical modules constituting the triplet (local coincidence). This effect and its use in the ANTARES experiment are explained in section 2. In the case of two modules located on different storeys the probability of a genuine coincidence from $^{40}$K is negligibly small. Instead, a signal originated from atmospheric muons could become dominating, if was not overwhelmed by the random background from $^{40}$K and bioluminescence. In order to reduce the random background we

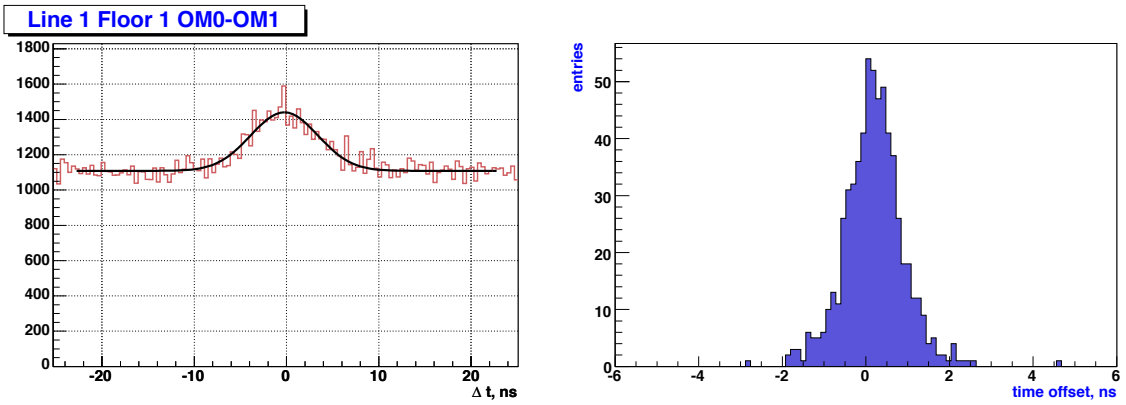


Figure 1: Left: time delay between hits in two optical modules of the same detector storey (example). Coincidence peak from Potassium-40 is evident (see text). Right: time offset of the coincidence peak (Line 1-10 data).

require a local coincidence (within 20 ns time window) at each of the two storeys rather than just a hit. Section 3 presents such an analysis for the case of adjacent storeys.

For the purpose of detailed $^{40}$K measurements a dedicated type of calibration runs is defined in ANTARES (K40 runs). During a K40 run (typically 20 minutes) all local coincidences detected in any OM triplet of ANTARES are selected by a dedicated data filter algorithm, so-called K40 trigger, and saved on disk for later processing. Importantly, this type of runs is also perfectly suitable for the adjacent floor coincidence studies.

## 2 Calibration with Potassium-40

Due to the difference in positions of the optical modules (the distance between OM centers is 1.0 m) the signals are detected by the two OMs with a noticeable delay. When averaging over many events (locations of decayed nucleus) this results in a time spread of 4.0 ns (RMS), that is experimentally observed (see Fig. 1). This value is in excellent accordance with Monte Carlo simulations. As one can see from Fig. 1, the coincidence peak is comparable in amplitude with the pedestal of random coincidences, which are composed of truly uncorrelated background photons (from $^{40}$K or bioluminescent emission). Ideally, if the optical modules are all identical, perfectly calibrated, and arranged in triplets symmetrically, the coincidence peak must be aligned with zero. Experimental measurements (see Fig. 1) show a small spread of the offsets (0.68 ns RMS), that confirms the high accuracy of timing calibration in ANTARES and gives a measure of disagreement between the $^{40}$K data and currently used calibration set. The present results refer to so-called Dark Room calibration, which is performed on shore before line deployment. An improvement is foreseen with the in-situ LED Beacon calibration, which is currently in progress.

The rate of correlated coincidences can be defined as the integral under the coincidence peak (excluding pedestal) normalized to the effective duration of observation period, and properly corrected for dead time of the electronics and data acquisition. We rely on a Gaussian fit to compute the rate. The observed average value amounts to 14 Hz (see Fig. 2, left), that is in good agreement with MC simulations. It has been checked experimentally that the coincidence rate is not affected by variations of the bioluminescent background. This important observation suggests that the $^{40}$K measurements can be used as a robust calibration tool. In addition, it also provides a confirmation of single-photon character of the bioluminescent emission. Indeed, if a bioluminescent process produced bunches of photons, correlated in nanosecond scale, an increase of the correlated coincidence rate would be observed for high-background runs.

It can be shown by Monte Carlo simulation that the rate of correlated coincidences is proportional to the detection efficiencies of both the optical modules involved. Thus, for a triplet

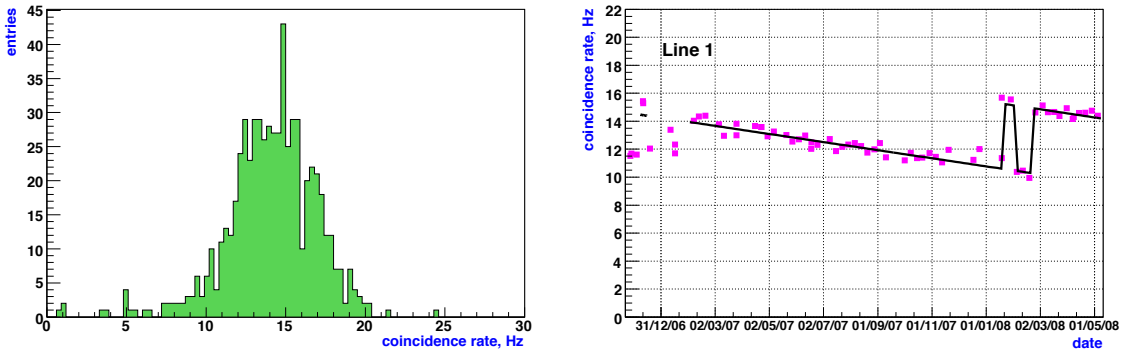


Figure 2: Left: rate of correlated coincidences produced in ANTARES storeys by $^{40}$K decays in sea water (Line 1-10 data). Right: evolution of average rate of correlated coincidences with time (Line 1 data). Continuous degradation of OM sensitivity is noticeable, as well as the effects of changing hardware thresholds.

one can write three equations as follows:

$$\begin{aligned} r_{12} &= k s_1 s_2 \\ r_{23} &= k s_2 s_3 \\ r_{31} &= k s_3 s_1 \end{aligned} \qquad (1)$$

where $s_{1(2,3)}$ is the sensitivity of OM1(2,3) in arbitrary units, $r_{12(23,31)}$ is the rate of correlated coincidences between OM1 and OM2 (OM2 and OM3, OM3 and OM1), and $k$ is a normalization factor. We will assume $k$ constant, i.e. not varying from module to module or with time. For a triplet of optical modules one can unambiguously solve system (1) and extract the three sensitivity coefficients $s_{1(2,3)}$. Note that the absolute normalization of the OM sensitivities requires precise knowledge of the OM angular acceptance (alternatively, OM angular acceptance can be constrained by the $^{40}$K measurements).

So far, OM sensitivity measurements have been done with $^{40}$K for ten detector lines of ANTARES, helping to locate mistuned and degraded modules. A significant drop of sensitivity was observed for some optical modules during first months of operation. In average a decrease of coincidence rates by 2.5% per month has been observed, that corresponds to about 1.2% decrease in OM sensitivity per month (see Fig. 2, right). These measurements agree qualitatively with observations of counting rates, which are continuously monitored in ANTARES (but can be affected by bioluminescence). The present method also allowed to measure the effect of tuning of hardware thresholds, recently performed in ANTARES in order to compensate the sensitivity drop. It was found that the adjustment of pulse-height discrimination thresholds allowed to effectively recover the initial detector sensitivity (see Fig. 2, right). This supports the hypothesis that the sensitivity drop occurs due to a continuous decrease of gain of the photomultiplier tubes. Further measurements with $^{40}$K are being performed to better investigate the observed phenomena and maintain high accuracy of the OM sensitivity calibration.

## 3 Low energy atmospheric muons

An experimental plot of adjacent floor coincidences (A2 coincidences) exhibits a prominent peak shifted toward positive values (see Fig. 3). This is the most basic signal of (downward-going) atmospheric muons detected so far in ANTARES. A Monte Carlo simulation performed using MUPAGE[5] agrees with the observations. The rate of correlated A2 coincidences (A2 rate), which can be defined as the integral under the peak, is directly linked to the atmospheric muon flux. One should note however that a good knowledge of absolute efficiency of the optical modules, as well as their angular response, is needed to accurately convert the A2 rate into the flux. Interestingly, some important information on the angular response curve can be extracted from

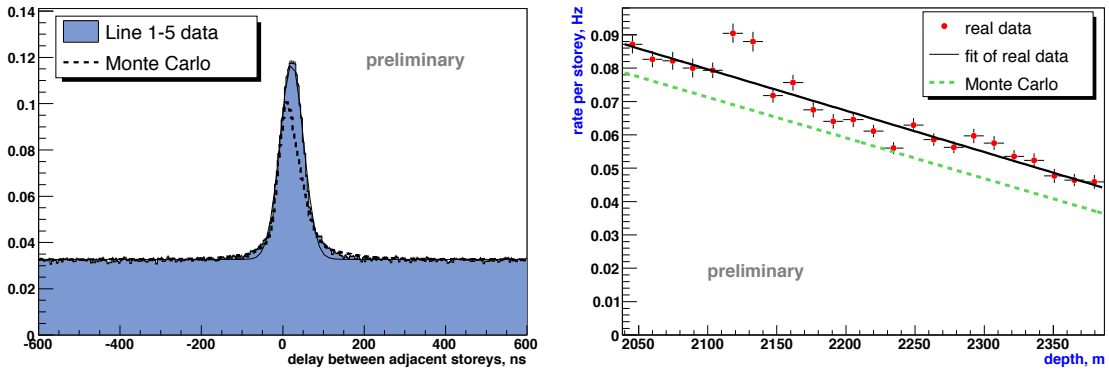


Figure 3: Left: time delay between two local coincidences detected in adjacent detector storeys (A2 coincidence plot, example). Right: depth dependence of A2 coincidence rate (Line 1-5 data). Each of the 24 points corresponds to a pair of adjacent detector floors. Both plots are preliminary.

the shape of the A2 plot. A detailed study trying to exploit this possibility is currently ongoing. Importantly, the analysis can be repeated for each detector floor separately, thus providing access to the depth-intensity relation of the muon flux. A preliminary analysis (see Fig. 3, right) has demonstrated the effect of muon absorption with depth. A dedicated effort is currently ongoing to develop the necessary corrections for the different sensitivities of the optical modules (and therefore storeys), and further develop this technique.

Clearly this analysis does not allow to determine the properties of each event (e.g. muon zenith angle). However, certain collective properties of the muon flux might well be accessible. Moreover, any systematic errors and inefficiencies of likelihood maximization and event selection procedures are also avoided in this case. In addition, the energy threshold of the coincidence study is much lower, thanks to the use of highly-efficient K40 trigger and very low requirements imposed on the number of signal hits by the analysis itself. Thus the coincidence study can not only provide a redundancy to muon flux measurements but also deliver a lot of useful and complementary information concerning the detector response and atmospheric muon flux.

## 4 Outlook

A new calibration technique grew up from an academic study of local coincidences in an ANTARES storey. The method represents a unique tool for measurements of optical module sensitivities in situ, and a valuable tool for time calibration in ANTARES. Thanks to this method the effect of OM efficiency drop was precisely measured, and a preliminary time calibration of ANTARES was confirmed in an independent way. Presently the method is used on a regular basis to control the sensitivities of the optical modules. A new approach to atmospheric muon flux studies with ANTARES was suggested, which also relies on a simple coincidence analysis. The method allows to measure the muon flux and, more importantly, its depth dependence. Some preliminary results were presented in this paper, further analysis is ongoing.

## References

1. ANTARES collaboration. *A Deep Sea Telescope for High Energy Neutrinos (Proposal).* (1999), http://antares.in2p3.fr.
2. T. Pradier. *These proceedings.*
3. ANTARES collaboration. *Nucl. Instrum. Methods* A **484**, 369 (2002).
4. ANTARES collaboration. *Nucl. Instrum. Methods* A **578**, 498 (2007), astro-ph/0703355..
5. G. Carminati, A. Margiotta, M. Spurio. arXiv:0802.0562.

# SNEUTRINO COLD DARK MATTER IN EXTENDED MSSM MODELS

C. ARINA
*Department of Theoretical Physics, Università di Torino, 1 Via Pietro Giuria, 10125 Torino, Italy*

A thorough analysis of sneutrinos as dark matter candidates is performed, in different classes of supersymmetric models, as is typically done for the neutralino dark matter. First in the Minimal Supersymmetric Standard Model, sneutrinos are marginally compatible with existing experimental bounds, including direct detection, provided they compose a subdominant component of dark matter. Then supersymmetric models with the inclusion of right-handed fields and lepton-number violating terms are presented. These models are perfectly viable: they predict sneutrinos which are compatible with the current direct detection sensitivities.

## 1 Sneutrino in the Minimal Standard Supersymmetric Model

We wish to reconsider in a consistent way sneutrino as a cold relic from the early Universe and study its phenomenology relevant both for Cosmology and for relic–particle detection in low–energy supersymmetric extensions of the Standard Model, which does not (necessarily) invoke mSUGRA relations. We first review the phenomenology of the sneutrino as Cold Dark Matter (CDM) candidate in the case of the Minimal Supersymmetric extension of the Standard Model (MSSM). This model, not very appealing for sneutrino CDM and actually already almost excluded by direct detection searches sets the basis for the extended models described in the next section. In the MSSM, sneutrinos are the scalar partners of the left–handed neutrinos and are described by the usual superpotential and soft breaking terms, leading to the mass-term $m_1 = \left[m_L^2 + \frac{1}{2} m_Z^2 \cos 2\beta\right]$, where $m_L$ is the soft–mass for the left–handed SU(2) doublet $\tilde{L}$, $\beta$ is defined as usual from the relation $\tan\beta = v_2/v_1$, where $v_2$ is the vacuum expectation value of the neutral component of the $H^2$ Higgs field and $m_Z$ is the $Z$–boson mass. First of all, we have calculated the sneutrino relic abundance, by taking into account all the relevant annihilation channels and co–annihilation processes which may arise when the sleptons are close in mass to the sneutrinos, as described in Ref. [1]. In this minimal MSSM models, the three neutrinos are degenerate in mass: they therefore must be considered jointly in the calculation of the relevant


Figure 1: Left: Sneutrino relic abundance $\Omega h^2$ as a function of the sneutrino mass $m_1$. The horizontal solid and dotted lines delimit the WMAP interval for CDM. Right: Sneutrino–nucleon scattering cross section $\xi\sigma_{\rm nucleon}^{\rm (scalar)}$ vs. the sneutrino mass $m_1$. The dashed–dotted curve shows the DAMA/NaI region, compatible with the annual modulation effect observed by the experiment. The vertical line denotes the lower bound on the sneutrino mass coming from the invisible $Z$–width. The solid (dashed) curves refer to models with (without) gaugino universality.

processes. An example of sneutrino relic abundance $\Omega h^2$ for the minimal MSSM is plotted in Fig. 1 as a function of the sneutrino mass. The sneutrino relic abundance is typically very small [2], much lower than the cosmological range for cold dark matter derived by the WMAP analysis[3], which is $0.092 \leq \Omega_{\rm CDM} h^2 \leq 0.124$. For all the mass range from the experimental lower bound of about $m_{\rm Z}/2$ up to 600–700 GeV sneutrinos as the LSP are cosmologically acceptable but they are typically underabundant. This means that sneutrinos in the minimal version of MSSM are not good dark matter candidates, except for masses in a narrow range which we determine to be 600–700 GeV. Dark matter direct search, which relies on the possibility to detect the recoil energy of a nucleus due to the elastic scattering of the dark matter particle off the nucleus of a low–background detector, is known to be a strong experimental constraint for sneutrino dark matter. The dependence of the direct detection rate on the DM particle rests into the particle mass and the scattering cross section. For sneutrinos, see Ref. [1] for details and references, coherent scattering arises due to $Z$ and Higgs exchange diagrams in the $t$–channel, therefore the relevant cross section on nucleus is given by $\sigma_{\mathcal{N}} = \sigma_{\mathcal{N}}^{Z} + \sigma_{\mathcal{N}}^{h,H}$. Comparisons with experimental results are more easily and typically performed by using the cross section on a single nucleon $\xi\sigma_{\rm nucleon}^{\rm (scalar)}$. We have to consider that, whenever the dark matter particle is subdominant in the Universe, also its local density $\rho_0$ in the Galaxy is very likely reduced with respect to the total dark matter density. This means that the dominant component of dark matter is not the sneutrino, but still sneutrinos form a small amount of dark matter and may be eventually detectable. In this case we rescale the local sneutrino abundance by means of the usual factor $\xi = \min(1, \Omega h^2/0.092)$. When compared with the DAMA/NaI annual modulation region [4] in Fig. 1 we see that direct detection is indeed a strong constraint on sneutrino dark matter in the minimal MSSM [2], but some very specific configurations are still viable and could explain the annual modulation effect.

## 2 Non minimal supersymmetric models

The models which we will be considering are natural and direct extensions of the MSSM which incorporate at the same time the new physics required to explain two basic problems of astro–particle physics: the origin of neutrino masses and the nature of dark matter. The first class of models (LR models), enlarge the neutrino/sneutrino sector by the inclusion of sterile right–handed superfields $\hat{N}^I$ [5,6]. The relevant terms in the superpotential and in the soft breaking potential are:

$$\begin{aligned} W &= \epsilon_{ij}(\mu \hat{H}_i^1 \hat{H}_j^2 - Y_l^{IJ} \hat{H}_i^1 \hat{L}_j^I \hat{R}^J + Y_\nu^{IJ} \hat{H}_i^2 \hat{L}_j^I \hat{N}^J) \\ V_{\rm soft} &= (M_L^2)^{IJ}\, \tilde{L}_i^{I*} \tilde{L}_i^J + (M_N^2)^{IJ}\, \tilde{N}^{I*} \tilde{N}^J - [\epsilon_{ij}(\Lambda_l^{IJ} H_i^1 \tilde{L}_j^I \tilde{R}^J + \Lambda_\nu^{IJ} H_i^2 \tilde{L}_j^I \tilde{N}^J) + \text{h.c.}] \end{aligned} \quad (1)$$

where $Y_\nu^{IJ}$ is a matrix, which we choose real and diagonal, from which the Dirac mass of neutrinos are obtained $m_D^I = v_2 Y_\nu^{II}$, as we do for the matrices $M_N^2$, $\Lambda_\nu^{IJ}$, $M_L^2$ and $\Lambda_l^{IJ}$. The parameter which mixes the left– and right–handed sneutrino fields may naturally be of the order of the other entries of the matrix, and induce a sizeable mixing of the lightest sneutrino in terms of left–handed and right–handed fields. The lightest mass eigenstate is therefore $\tilde{\nu}_1 = -\sin\theta\ \tilde{\nu}_L + \cos\theta\ \tilde{N}$, where $\theta$ is the LR mixing angle. Sizeable mixings reduce the coupling to the $Z$–boson, which couples only to left–handed fields, and therefore have relevant impact on all the sneutrino phenomenology: the lightest sneutrino may be lighter than $m_Z/2$ and the $\tilde{\nu}_1$ annihilation and scattering cross sections which involve $Z$ exchange are reduced, see Ref [1] for details. A supersymmetric model which can accommodate a Majorana mass–term for neutrinos and explain the observed neutrino mass pattern, may be built by adding to the minimal MSSM right–handed fields $\tilde{N}^I$ and allowing for lepton number violating ($\not{L}$) terms (Majorana models). The most general form of the superpotential [5,6] and of the soft breaking potential [7], which accomplishes this conditions is:

$$\begin{aligned} W &= \epsilon_{ij}(\mu \hat{H}_i^1 \hat{H}_j^2 - Y_l^{IJ} \hat{H}_i^1 \hat{L}_j^I \hat{R}^J + Y_\nu^{IJ} \hat{H}_i^2 \hat{L}_j^I \hat{N}^J) + \frac{1}{2} M^{IJ} \hat{N}^I \hat{N}^J \\ V_{\rm soft} &= (M_L^2)^{IJ}\, \tilde{L}_i^{I*} \tilde{L}_i^J + (M_N^2)^{IJ}\, \tilde{N}^{I*} \tilde{N}^J - \\ &\quad [(m_B^2)^{IJ} \tilde{N}^I \tilde{N}^J + \epsilon_{ij}(\Lambda_l^{IJ} H_i^1 \tilde{L}_j^I \tilde{R}^J + \Lambda_\nu^{IJ} H_i^2 \tilde{L}_j^I \tilde{N}^J) + \text{h.c.}] \end{aligned} \quad (2)$$

where we again use the same assumptions of diagonality in flavour space for all the matrices as we already did before. For the $\not{L}$ parameters we therefore assume: $M^{IJ} = M\ \delta^{IJ}$, in order to reduce the number of free parameters. The Dirac mass of the neutrinos is obtained as: $m_D^I = v_2 Y_\nu^{II}$, while $M^I$ represent a Majorana mass–term for neutrinos. The Dirac–mass parameter is derived by the condition that the neutrino mass is determined by the see-saw mechanism: $m_\nu^I = m_D^I / M^2$. Sneutrinos now are a superpositions of two complex fields: the left–handed field $\nu_L$ and the right–handed field $\tilde{N}$. Since we introduced $\not{L}$ terms, it is convenient to work in a basis of CP eigenstates, where the $\tilde{\nu} - Z$ coupling is off diagonal. The non-diagonal nature of the $Z$–coupling leads to important consequences: first of all annihilation processes through Z channel become co–annihilation processes, thus reducing the annihilation cross sections; moreover the elastic scattering off nucleon becomes an inelastic scattering via $t$–channel Z exchange and under certain kinematics condition may be suppressed, leading to a lower value of the direct detection rate of the sneutrino dark matter. The lightest state, which is our dark matter candidate, may now exhibit the non–diagonal nature of the $Z$–coupling with respect of the CP eigenstates, $\tilde{\nu}_-, \tilde{\nu}_+$, which are also mass eigenstates, and a mixing with the right–handed field $\tilde{N}$: $\tilde{\nu}_i = Z_{i1}\tilde{\nu}_+ + Z_{i2}\tilde{N}_+ + Z_{i3}\tilde{\nu}_- + Z_{i4}\tilde{N}_-$ with $i = 1, 2, 3, 4$.

In LR models sneutrinos may represent the dominant dark matter component for a wide mass range. The most relevant new feature is that for the full supersymmetric scan, the mass range allowed by the cosmological constraints is enlarged up to 800 GeV, and all the mass interval above the $Z$–pole may lead to strongly subdominant sneutrinos. From Fig. 2 we can conclude that after all experimental and theoretical constraints are imposed, sneutrino dark matter is perfectly viable, both as a dominant and as a subdominant component, for the whole mass range 15 GeV $\lesssim m_1 \lesssim$ 800 GeV. The lower limit of 15 GeV represents therefore a cosmological bound on the sneutrino mass in LR models, under the assumption of $R$–parity conservation. The sneutrino–nucleon cross section is shown in the right top in Fig. 2. Only points which are accepted by the cosmological constraint are shown. We see that the presence of the mixing with the right–handed $\tilde{N}$ fields opens up the possibility to have viable sneutrino cold dark matter. A fraction of the configurations are excluded by direct detection, but now, contrary to the minimal MSSM case, a large portion of the supersymmetric parameter space is compatible with the direct detection bound, both for cosmologically dominant ([red] crosses) and subdominant ([blue] points) sneutrinos. The occurrence of sneutrinos which are not in conflict

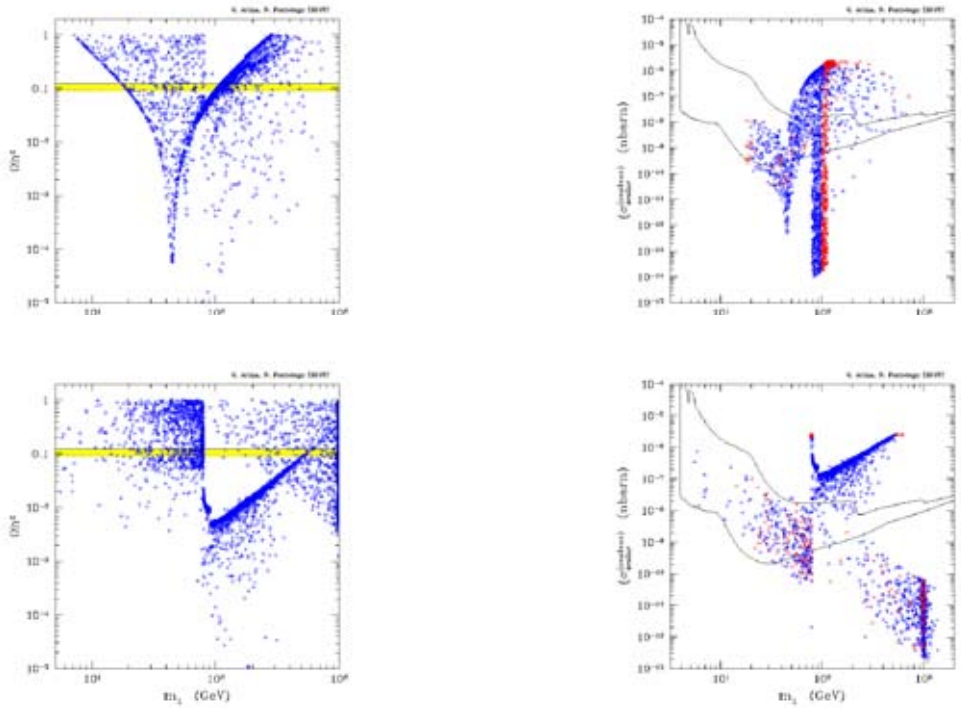

Figure 2: Top – LR models – Left: Sneutrino relic abundance $\Omega h^2$ vs. the sneutrino mass $m_1$. Right: Sneutrino–nucleon scattering cross section $\xi\sigma^{(\mathrm{scalar})}_{\mathrm{nucleon}}$ vs. the sneutrino mass $m_1$. Bottom – Majorana mass parameter $M = 1$ TeV – Left: Sneutrino relic abundance $\Omega h^2$ vs. the sneutrino mass $m_1$. Right: Sneutrino–nucleon scattering cross section $\xi\sigma^{(\mathrm{scalar})}_{\mathrm{nucleon}}$ vs. the sneutrino mass $m_1$. [Red] crosses refer to models with sneutrino relic abundance in the WMAP range; [blue] open circles refer to subdominant sneutrinos. The experimental regions are defined in Fig. 1.

with direct detection limits and, at the same time, are the dominant dark matter component, is a very interesting feature of this class of models. The relic abundance of the Majorana models at low–mass scale is shown on the left bottom in Fig. 2. It is remarkable that in the whole mass range from 5 GeV to 1 TeV sneutrinos can explain the required amount of CDM in the Universe. For the same mass range, sneutrinos may as well be a subdominant component. Direct detection is shown on the right bottom in Fig. 2. We see that three different populations arise: configurations on the upper right are clearly excluded by direct detection searches. Most of them refer to subdominant sneutrinos. Configurations on the lower right part of the plot are allowed but well below current direct detection sensitivity. Configurations on the center and left part of the plot all fall inside the current sensitivity region: a large fraction are cosmologically dominant and could explain the annual modulation effect observed by the DAMA/NaI experiment.

**Acknowledgments**

I acknowledge the European "Marie Curie" Programme for the support grant.

**References**

1. C. Arina and N. Fornengo, *JHEP* **0711**, 029 (2007).
2. T. Falk, K. A. Olive and M. Srednicki, *Phys. Lett.* B **339**, 248 (1994).
3. D. N. Spergel *et al*, *Astrophys. J. Suppl.* **170**, 377 (2007).
4. R. Bernabei *et al*, *Nuovo Cimento* **26N1**, 1 (2003)
5. N. Arkani-Hamed *et al*, *Phys. Rev.* D **64**, 115011 (2001).
6. Y. Grossman and H. E. Haber, *Phys. Rev. Lett.* **78**, 3438 (1997).
7. A. Dedes, H. A. Haber and J. Rosiek, *JHEP* **0711**, 059 (2007).

# EFFECTS OF LIGHTEST NEUTRINO MASS IN LEPTOGENESIS

E. MOLINARO [1,a], S. T. PETCOV [1,3,b], T. SHINDOU [2], Y. TAKANISHI [1]

[1)] *SISSA and INFN-Sezione di Trieste, Trieste I-34014, Italy*

[2)] *Deutsches Elektronen Synchrotron DESY, Notkestrasse 85, 22607 Hamburg, Germany*

[3)] *IPMU, University of Tokyo, Tokyo, Japan*

The effects of the lightest neutrino mass in "flavoured" leptogenesis are investigated in the case when the CP-violation necessary for the generation of the baryon asymmetry of the Universe is due exclusively to the Dirac and/or Majorana phases in the neutrino mixing matrix $U$. The type I see-saw scenario with three heavy right-handed Majorana neutrinos having hierarchical spectrum is considered. The "orthogonal" parametrisation of the matrix of neutrino Yukawa couplings, which involves a complex orthogonal matrix $R$, is employed. Results for light neutrino mass spectrum with normal and inverted ordering (hierarchy) are obtained. It is shown, in particular, that if the matrix $R$ is real and CP-conserving and the lightest neutrino mass $m_3$ in the case of inverted hierarchical spectrum lies the interval $5 \times 10^{-4}$ eV $\lesssim m_3 \lesssim 7 \times 10^{-3}$ eV, the predicted baryon asymmetry can be larger by a factor of $\sim 100$ than the asymmetry corresponding to negligible $m_3 \cong 0$. As consequence, we can have successful thermal leptogenesis for $5 \times 10^{-6}$ eV $\lesssim m_3 \lesssim 5 \times 10^{-2}$ eV even if $R$ is real and the only source of CP-violation in leptogenesis is the Majorana and/or Dirac phase(s) in the neutrino mixing matrix.

## 1 Introduction

We investigate the effects of the lightest neutrino mass in thermal leptogenesis [1,2] where lepton flavor effects [3–8] play an important role in the generation of the observed baryon asymmetry of the Universe and the CP-violation required for the baryogenesis mechanism to work is due exclusively to the Dirac and/or Majorana CP-violating phases in the Pontecorvo-Maki-Nakagawa-Sakata (PMNS) [9] neutrino mixing matrix. A detailed analysis of these effects has been performed in reference [10].

The minimal scheme in which leptogenesis can be implemented is the non-supersymmetric version of the type I see-saw [11] model with two or three heavy right-handed (RH) Majorana neutrinos. Taking into account the lepton flavour effects in leptogenesis it was shown [12] (see also [4,13,14]) that if the heavy Majorana neutrinos have a hierarchical spectrum, the observed baryon asymmetry $Y_B$ can be produced even if the only source of CP-violation is the Majorana and/or Dirac phase(s) in the PMNS matrix $U_{\rm PMNS} \equiv U$. In this case the predicted value of

[a] Talk given at Recontres de Moriond EW 2008, La Thuile, 1-8 March 2008, based on the paper: E. M., S. T. Petcov, T. Shindou and Y. Takanishi, "Effects of Lightest Neutrino Mass in Leptogenesis," Nucl. Phys. B **797** (2008) 93 [arXiv:0709.0413 [hep-ph]].

[b] Also at: Institute of Nuclear Research and Nuclear Energy, Bulgarian Academy of Sciences, 1784, Sofia, Bulgaria.

the baryon asymmetry depends explicitly (i.e. directly) on $U$ and on the CP-violating phases in $U$. The results quoted above were demonstrated to hold both for normal hierarchical (NH) and inverted hierarchical (IH) spectrum of masses of the light Majorana neutrinos. In both these cases they were obtained for negligible lightest neutrino mass and CP-conserving elements of the orthogonal matrix $R$, present in the "orthogonal" parametrisation [15] of the matrix of neutrino Yukawa couplings. The CP-invariance constraints imply that the matrix $R$ could conserve the CP-symmetry if its elements are real or purely imaginary[c]. We remark that for a CP-conserving matrix $R$ and at temperatures $T \sim M_1 \gtrsim 10^{12}$ GeV, the lepton flavours are indistnguishible (one flavour approximation) and the total CP asymmetry is always zero. In this case no baryon asymmetry is produced. One can prove [12] that, for NH spectrum and negligible lightest neutrino mass $m_1$ successful thermal leptogenesis can be realised for a real matrix $R$. In contrast, in the case of IH spectrum and negligible lightest neutrino mass ($m_3$), the requisite baryon asymmetry was found to be produced for CP-conserving matrix $R$ only if certain elements of $R$ are purely imaginary: for real $R$ the baryon asymmetry $Y_B$ is strongly suppressed and leptogenesis cannot be successful for $M_1 \lesssim 10^{12}$ GeV (i.e. in the regime in which the lepton flavour effects are significant [5,6,7]).

In the present work we have analysed the effects of the lightest neutrino mass on "flavoured" (thermal) leptogenesis. We considered the case when the CP-violation necessary for the generation of the observed baryon asymmetry of the Universe is due exclusively to the Dirac and/or Majorana CP-violating phases in the PMNS matrix $U$. Our study is performed within the simplest type I see-saw scenario with three heavy RH Majorana neutrinos $N_j$, $j = 1, 2, 3$. The latter are assumed to have a hierarchical mass spectrum, $M_1 \ll M_{2,3}$. As a consequence, the generated baryon asymmetry $Y_B$ depends linearly on the mass of $N_1$, $M_1$, and on the elements $R_{1j}$ of the matrix $R$, $j = 1, 2, 3$, present in the neutrino Yukawa couplings of $N_1$. Throughout the present study we employ the "orthogonal" parametrisation of the matrix of neutrino Yukawa couplings. As was already mentioned previously, this parametrisation involves an orthogonal matrix $R$, $R^T R = R R^T = \mathbf{1}$. Although, in general, the matrix $R$ can be complex, i.e. CP-violating, in the present work we are primarily interested in the possibility that $R$ conserves the CP-symmetry. We consider the two types of light neutrino mass spectrum allowed by the data [17]: i) with normal ordering ($\Delta m^2_{\rm A} > 0$), $m_1 < m_2 < m_3$, and ii) with inverted ordering ($\Delta m^2_{\rm A} < 0$), $m_3 < m_1 < m_2$. The case of inverted hierarchical (IH) spectrum and real (and CP-conserving) matrix $R$ is investigated in detail.

Our analysis is performed for negligible renormalisation group (RG) running of $m_j$ and of the parameters in the PMNS matrix $U$ from $M_Z$ to $M_1$. This possibility is realised for sufficiently small values of the lightest neutrino mass $\min(m_j)$ [18,19], e.g., for $\min(m_j) \lesssim 0.10$ eV. The latter condition is fulfilled for the NH and IH neutrino mass spectra, as well as for spectrum with partial hierarchy [20]. Under the indicated condition $m_j$, and correspondingly $\Delta m^2_{\rm A}$ and $\Delta m^2_{\odot}$, and $U$ can be taken at the scale $\sim M_Z$, at which the neutrino mixing parameters are measured.

## 2 Light Neutrino Mass Spectrum with Inverted Ordering and Real $R_{1j}$

The case of inverted hierarchical (IH) neutrino mass spectrum, $m_3 \ll m_1 < m_2$, $m_{1,2} \cong \sqrt{|\Delta m^2_{\rm A}|}$, is of particular interest since, as was already mentioned, for real $R_{1j}$, $j = 1, 2, 3$, IH spectrum and negligible lightest neutrino mass $m_3 \cong 0$, it is impossible to generate the observed baryon asymmetry $Y_B \cong 8.6 \times 10^{-11}$ in the regime of "flavoured" leptogenesis [12], i.e. for $M_1 \lesssim 10^{12}$ GeV, if the only source of CP violation are the Majorana and/or Dirac phases in the

[c] The case in which CP-violation arises from the combined effect between the "low energy" Majorana and/or Dirac phases in $U_{\rm PMNS}$ and the "high energy" CP-violating phases in a complex orthogonal matrix $R$, in thermal "flavoured" leptogenesis scenario, has recently been addressed [16].

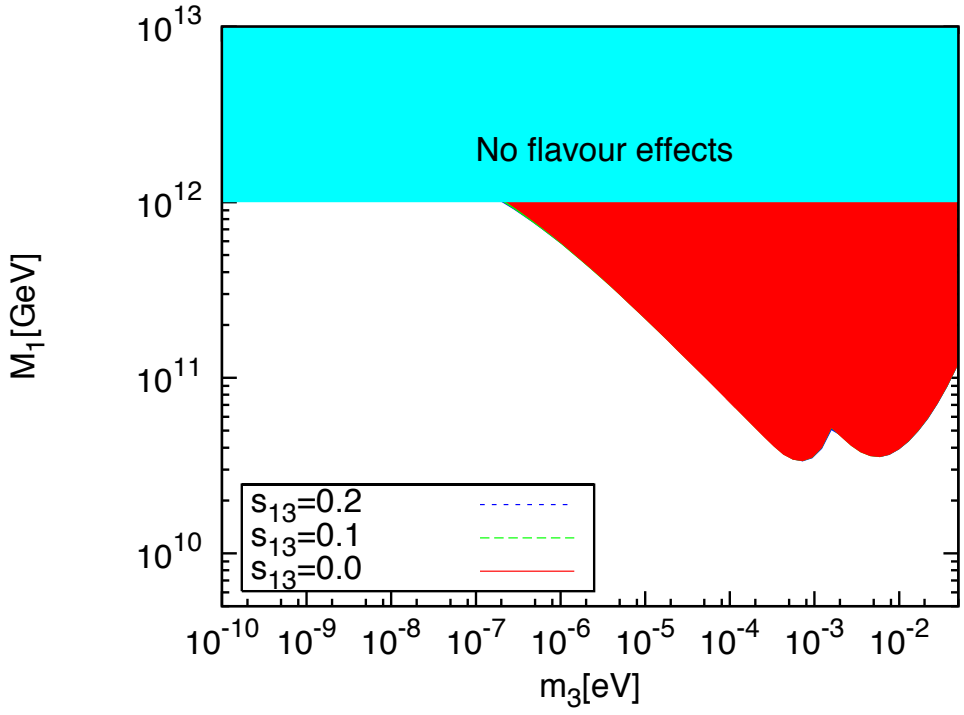


Figure 1: Values of $m_3$ and $M_1$ for which the "flavoured" leptogenesis is successful, generating baryon asymmetry $|Y_B| = 8.6 \times 10^{-11}$ (red/dark shaded area). The figure corresponds to hierarchical heavy Majorana neutrinos, light neutrino mass spectrum with inverted ordering (hierarchy), $m_3 < m_1 < m_2$, and real elements $R_{1j}$ of the matrix $R$. The results shown are obtained using the best fit values of neutrino oscillation parameters: $\Delta m^2_{\odot} = 8.0 \times 10^{-5}$ eV$^2$, $\Delta m^2_{\rm A} = 2.5 \times 10^{-3}$ eV$^2$, $\sin^2\theta_{12} = 0.30$ and $\sin^2 2\theta_{23} = 1$.

PMNS matrix. It can be proved that for $m_3 = 0$ and $R_{13} = 0$, the resulting baryon asymmetry is always suppressed by the factor $\Delta m^2_{\odot}/(2\Delta m^2_{\rm A}) \cong 1.6 \times 10^{-2}$. We analyse the generation of the baryon asymmetry $Y_B$ for real $R_{1j}$, $j = 1, 2, 3$, when $m_3$ is non-negligible. We assume that $Y_B$ is produced in the two-flavour regime, $10^9$ GeV $\lesssim M_1 \lesssim 10^{12}$ GeV.

In Fig. 1 we show the correlated values of $M_1$ and $m_3$ for which one can have successful leptogenesis in the case of neutrino mass spectrum with inverted ordering and CP-violation due to the Majorana and Dirac phases in $U_{\rm PMNS}$. The figure was obtained by performing, for given $m_3$ from the interval $10^{-10}$eV $\leq m_3 \leq 0.05$ eV, a thorough scan of the relevant parameter space searching for possible enhancement or suppression of the baryon asymmetry with respect to that found for $m_3 = 0$. The real elements of the $R-$matrix of interest, $R_{1j}$, $j = 1, 2, 3$, were allowed to vary in their full ranges determined by the condition of orthogonality of the matrix $R$: $R^2_{11} + R^2_{12} + R^2_{13} = 1$. The Majorana phases $\alpha_{21,31}$ were varied in the interval $[0, 2\pi]$. The calculations were performed for three values of the CHOOZ angle $\theta_{13}$, corresponding to $\sin\theta_{13} = 0;\ 0.1;\ 0.2$. In the cases of $\sin\theta_{13} \neq 0$, the Dirac phase $\delta$ was allowed to take values in the interval $[0, 2\pi]$. The heavy Majorana neutrino mass $M_1$ was varied in the interval $10^9$ GeV $\leq M_1 \leq 10^{12}$ GeV. For given $m_3$, the minimal value of the mass $M_1$, for which the leptogenesis is successful, generating $|Y_B| \cong 8.6 \times 10^{-11}$, was obtained for the values of the other parameters which maximise $|Y_B|$. We have found that in the case of IH spectrum with non-negligible $m_3$, $m_3 \ll \sqrt{|\Delta m^2_{\rm A}|}$, the generated baryon asymmetry $|Y_B|$ can be strongly enhanced in comparison with the asymmetry $|Y_B|$ produced if $m_3 \cong 0$. The enhancement can be by a factor of $\sim 100$, or even by a larger factor. As a consequence, one can have successful leptogenesis for IH spectrum with $m_3 \gtrsim 5 \times 10^{-6}$ eV even if the elements $R_{1j}$ of $R$ are real and the requisite CP-violation is provided by the Majorana or Dirac phase(s) in the PMNS matrix. As a consequence, successful thermal leptogenesis is realised for $5 \times 10^{-6}$ eV $\lesssim m_3 \lesssim 5 \times 10^{-2}$ eV. The results of our analysis show that for Majorana CP-violation from $U_{\rm PMNS}$, successful

leptogenesis can be obtained for $M_1 \gtrsim 3.0 \times 10^{10}$ GeV. A somewhat larger values of $M_1$ are typically required if the CP-violation is due to the Dirac phase $\delta$: $M_1 \gtrsim 10^{11}$ GeV. The requirement of successful "flavoured" leptogenesis in the latter case leads to the following lower limits on $|\sin\theta_{13}\sin\delta|$, and thus on $\sin\theta_{13}$ and on the rephasing invariant $J_{\rm CP}$ which controls the magnitude of CP-violation effects in neutrino oscillations: $|\sin\theta_{13}\sin\delta|, \sin\theta_{13} \gtrsim (0.04 - 0.09)$, $|J_{\rm CP}| \gtrsim (0.009 - 0.020)$, where the precise value of the limit within the intervals given depends on the $\mathrm{sgn}(R_{11}R_{13})$ (or $\mathrm{sgn}(R_{12}R_{13})$) and on $\sin^2\theta_{23}$.

The results we have obtained for light neutrino mass spectrum with normal ordering, $m_1 < m_2 < m_3$, can vary significantly if one of the elements $R_{1j}$ is equal to zero. In particular, if $R_{11} \cong 0$, we did not find any significant enhancement of the baryon asymmetry $|Y_B|$, generated within "flavoured" leptogenesis scenario with real matrix $R$ and CP-violation provided by the neutrino mixing matrix $U_{\rm PMNS}$, when the lightest neutrino mass was varied in the interval $10^{-10}$ eV $\leq m_1 \leq 0.05$ eV. If, however, $R_{12} \cong 0$, the dependence of $|Y_B|$ on $m_1$ exhibits qualitatively the same features as the dependence of $|Y_B|$ on $m_3$ in the case of neutrino mass spectrum with inverted ordering (hierarchy), although $\max(|Y_B|)$ is somewhat smaller than in the corresponding IH spectrum cases. As a consequence, it is possible to reproduced the observed value of $Y_B$ if the CP-violation is due to the Majorana phase(s) in $U_{\rm PMNS}$ provided $M_1 \gtrsim 5.3 \times 10^{10}$ GeV.

The analysis we have performed shows that within the thermal "flavoured" leptogenesis scenario, the value of the lightest neutrino mass can have non negligibile effects on the magnitude of the baryon asymmetry of the Universe in the cases of light neutrino mass spectrum with inverted and normal ordering (hierarchy). In particular, as regards the IH spectrum, one can have an enhancement of the baryon asymmetry by a factor of $\sim 100$ with respect to the value corresponding to $m_3 \cong 0$, thus allowing for the generation of a matter-antimatter asymmetry compatible with the experimental observation.

## Acknowledgements

This work was supported in part by the INFN under the program "Fisica Astroparticellare", and by the Italian MIUR (Internazionalizzazione Program) and Yukawa Institute of Theoretical Physics (YITP), Kyoto, Japan, within the joint SISSA - YITP research project on "Fundamental Interactions and the Early Universe" (S.T.P.).

## References

1. M. Fukugita and T. Yanagida, Phys. Lett. B **174** (1986) 45.
2. V.A. Kuzmin, V.A. Rubakov and M.E. Shaposhnikov, Phys. Lett. B **155** (1985) 36.
3. R. Barbieri, P. Creminelli, A. Strumia and N. Tetradis, Nucl. Phys. B **575** (2000) 61.
4. H. B. Nielsen and Y. Takanishi, Nucl. Phys. B **636** (2002) 305.
5. A. Abada *et al.*, JCAP **0604** (2006) 004.
6. E. Nardi, Y. Nir, E. Roulet and J. Racker, JHEP **0601** (2006) 164.
7. A. Abada *et al.*, JHEP **0609** (2006) 010.
8. S. Antusch, S. F. King and A. Riotto, JCAP **0611** (2006) 011.
9. B. Pontecorvo, Zh. Eksp. Teor. Fiz. **33** (1957) 549, **34** (1958) 247 and **53** (1967) 1717; Z. Maki, M. Nakagawa and S. Sakata, Prog. Theor. Phys. **28** (1962) 870.
10. E. Molinaro, S. T. Petcov, T. Shindou and Y. Takanishi, Nucl. Phys. B **797** (2008) 93 [arXiv:0709.0413 [hep-ph]].
11. P. Minkowski, Phys. Lett. B **67** (1977) 421; M. Gell-Mann, P. Ramond and R. Slansky, *Proceedings of the Supergravity Stony Brook Workshop*, New York 1979, eds. P. Van Nieuwenhuizen and D. Freedman; T. Yanagida, *Proceedinds of the Workshop on Unified*

*Theories and Baryon Number in the Universe*, Tsukuba, Japan 1979, ed.s A. Sawada and A. Sugamoto; R. N. Mohapatra and G. Senjanovic, Phys. Rev. Lett. **44** (1980) 912.
12. S. Pascoli, S.T. Petcov and A. Riotto, Phys. Rev. D **68** (2003) 093007; Nucl. Phys. B **739** (2006) 208.
13. G. C. Branco, R. Gonzalez Felipe and F. R. Joaquim, Phys. Lett. B **645** (2007) 432.
14. S. Blanchet and P. Di Bari, JCAP **0703** (2007) 018.
15. J. A. Casas and A. Ibarra, Nucl. Phys. B **618** (2001) 171.
16. E. Molinaro and S. T. Petcov, arXiv:0803.4120 [hep-ph].
17. S.T. Petcov, Nucl. Phys. B (Proc. Suppl.) **143** (2005) 159 (hep-ph/0412410).
18. J. A. Casas, J. R. Espinosa, A. Ibarra and I. Navarro, Nucl. Phys. B **573** (2000) 652; S. Antusch *et al.*, Phys. Lett. B **519** (2001) 238; T. Miura, T. Shindou and E. Takasugi, Phys. Rev. D **66** (2002) 093002.
19. S. T. Petcov, T. Shindou and Y. Takanishi, Nucl. Phys. B **738** (2006) 219.
20. S. M. Bilenky, S. Pascoli and S. T. Petcov, Phys. Rev. D **64** (2001) 113003.

# SEARCH FOR NEUTRINOLESS DOUBLE BETA DECAY WITH NEMO-3 USING $^{150}$ND

Y. LEMIERE
*LPC Caen, ENSICAEN, Université de Caen, CNRS/IN2P3, Caen, France*

The NEMO-3 detector looks for neutrinoless double beta decay from 10 kg of enriched $\beta\beta$ emiters. Using 440 days of data, background measurements give activities from each contribution from Neodinium foil. During the same period of data acquisition, preliminary study gives the half-life of the $2\nu\beta\beta$ process : $T_{1/2}(2\nu) = (9.75 \pm 0.35(stat.) \pm 0.85(syst.))10^{18} years$. Up to now, no evidence of lepton number violation has been observed. A limit on the half-life of the neutrinoless process has been obtained : $T_{1/2}(0\nu) > 8.0 \quad 10^{21}$ y at 90% CL.

## 1 Neutrinoless double beta decay

The goal of the NEMO-3 (Neutrino Ettore Majorana Observatory) detector is to search for evidence of lepton number violation in neutrinoless double beta decay ($0\nu\beta\beta$):

$$(A, Z) \rightarrow (A, Z + 2) + 2e^{-} \tag{1}$$

The decay may be explained by the exchange of a light massive Majorana neutrino. Also (V+A) coupling or Majoron emission could describe the $0\nu\beta\beta$ decay. These processes, forbidden in the framework of the standard model, are the only experimental opportunity to prove the Majorana nature of the neutrino.

The half-life of the $0\nu\beta\beta$ process by light Majorana neutrino exchange can be written as :

$$(T^{0\nu}_{1/2})^{-1} = G^{0\nu}(Z, Q_{\beta\beta})|M^{0\nu}_{GT} - (\frac{g_V}{g_A})^2 M^{0\nu}_{F}|^2 \langle m_{\beta\beta}\rangle^2 \tag{2}$$

Where $G^{0\nu}(Z, Q_{\beta\beta})$ is the phase space factor proportional to the $Q^5_{\beta\beta}$, $M^{0\nu}_{\chi}$ are the nuclear matrix elements (NME) and $\langle m_{\beta\beta}\rangle$ is the effective mass of neutrino given by :

$$< m_{\nu_{\beta\beta}} >= |\cos^2\theta_{13}(|m_1|\cos^2\theta_{12} + |m_2|e^{2i\phi_1}\sin^2\theta_{12}) + |m_3|e^{2i\phi_2 - \delta}\sin^2\theta_{12}| \tag{3}$$

| Isotopes | $Q_{\beta\beta}$ (keV) | Mass d'isotope (g) |
|---|---|---|
| $^{130}Te \rightarrow {}^{130}Xe$ | 2533±4 | 454 |
| $^{116}Cd \rightarrow {}^{116}Sn$ | 2802±4 | 405 |
| $^{82}Se \rightarrow {}^{82}Kr$ | 2995±6 | 932 |
| $^{100}Mo \rightarrow {}^{100}Ru$ | 3034±6 | 6914 |
| $^{96}Zr \rightarrow {}^{96}Mo$ | 3350±3 | 9,4 |
| $^{150}Nd \rightarrow {}^{150}Sm$ | 3367±2 | 37 |
| $^{48}Ca \rightarrow {}^{48}Ti$ | 4271±4 | 6,99 |

Table 1: $\beta\beta$ emitters in the NEMO-3 detector.

The measurement of the $0\nu\beta\beta$ process half-life, given the NME, determines the absolute Majorana neutrino scale.

## 2 Searching for golden events in the NEMO-3 detector

The NEMO-3 [1] detector is designed to detect and identify neutrinoless double beta decays using 10 kg of enriched $\beta\beta$ emiters (Cf. table 1).

Isotopes are spread on thin foils at the center of a drift chamber formed by 6180 open Geiger cells to reconstruct charged particles tracks. An ultra pure calorimeter made of 1940 plastic scintillators encloses the drift chamber to measure energy and time of flight of particles coming from the source foils. NEMO-3 is able to identify $0\nu\beta\beta$ candidate events (golden events) with some dedicated criteria.

In figure 1-(b) a partial top view of the detector shows a $0\nu\beta\beta$-like event in NEMO-3 detector. There are two $\beta$ tracks with negative curvature with a common vertex on the source foil. The time of flight is compatible with an event coming from the foil ($\delta t_{TOF} \approx 0$). The total energy deposit in the calorimeter is equal to 3222 keV ($Q_{\beta\beta}$=3367 keV for $^{150}$Nd and energy resolution : 14 % at 1 MeV). This event from 37 g of $^{150}$Nd is a typical golden event ($\Delta$L=2 process).

## 3 Analysis and results

The golden event showed in figure 1-(b) is simulated from possible background contribution. Each process which is able to produce two electrons with a total energy around $Q_{\beta\beta}$ is considered as a dangerous background for the neutrinoless double beta decay investigation. For example, a $\beta\beta$-like event can be generated by a $\beta - \gamma$ emiter, the second electron being produced by Compton or photoelectric effect.

Typically the most important background comes from natural radioactive chain ($^{238}$U and $^{232}$Th). That brings to light the crucial importance of the extreme radio-purity one needs to achieve in order to reach a sensitivity to the half-life of up to $10^{24-25}$ years. The NEMO-3 detector is hosted in the Frejus underground laboratory under 4800 m.w.e. to reduce the cosmic ray flux. More the allowed process ($2\nu\beta\beta$) is the ultimate background which cannot be suppressed due to the energy resolution (Cf. figure 1-(a)).

### *3.1 Background studies*

The so-called *tracko-calo* technology used in NEMO-3 is able to measure and control the background sources using dedicated channels and to localize possible contaminations. The channels of interest are defined by the decay scheme from natural radioactive isotopes (Cf figure 2).

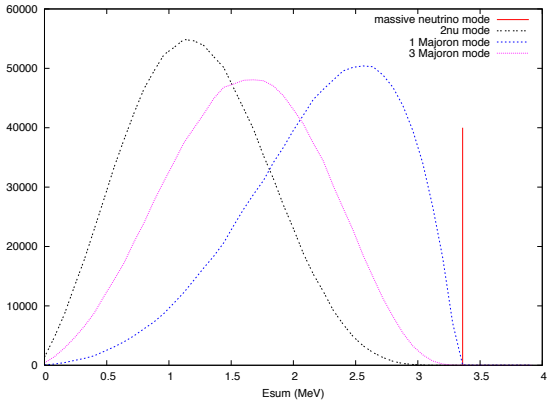


(a) Theorical spectrum of the total energy for $\beta\beta$ processes in $^{150}$Nd. The standard model allowed process ($2\nu\beta\beta$) is observed in NEMO-3. Due to the energy resolution, the continuous energy spectrum is a significant source of background for the $0\nu\beta\beta$ search.

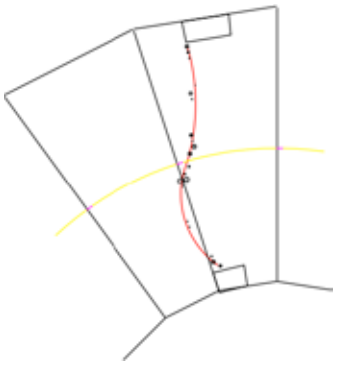

(b) Top view of a typical $0\nu\beta\beta$ event in NEMO-3 from $^{150}$Nd.

Figure 1:

- $^{208}$Tl from the $^{232}$Th chain is a $\beta$ emiter with $Q_\beta$ at 4.99 MeV. The most efficient signature to study this background consists in the measurement of one electron and several photons from dexecitation from the daughter nucleus. The corresponding channel is defined by an electron in coincidence with at least $\gamma$ rays. The $^{208}$Tl activity in $^{150}$Nd foil using such techniques has been measured at 17 $\mu$Bq.

- $^{214}$Bi from $^{238}$U chain is a $\beta$ emiter at $Q_\beta$=3.27 MeV followed by the $\alpha$ ($T_{1/2}$=164 $\mu$s) from $^{214}$Po decay in $^{210}$Pb. Dedicated electronics have been developped to identify the delayed $\alpha$ particle in the tracking chamber. The main channel to measure the BiPo cascade contamination is a prompt $\beta$ decay in coincidence with a delayed $\alpha$. $^{214}$Bi contamination has been measured on the Nd foil at the level of 90 $\mu$Bq.

These results are compatible with independant measurements using HPGe detector.

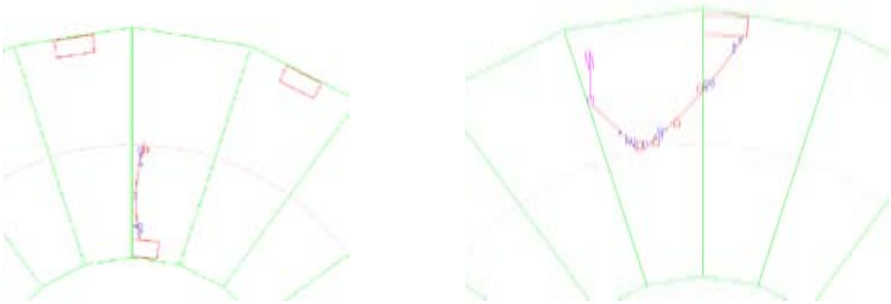

(a) (b)

Figure 2: Vizualisation of some channels studied to measure background contamination in NEMO-3 detector. a) Typical event in the e$\gamma\gamma$ channel used to identify the $^{208}$Tl contamination. b) Typical event in the e$\gamma\alpha$ channel used in case of $^{214}$Bi contamination.

*3.2 Double beta decay analysis*

The total energy spectra from two internal electron channel is split into two main parts. The [0-3] MeV region is used to measure the $2\nu\beta\beta$ process and the [3-3.6] MeV energy range is used to search for $0\nu\beta\beta$ signal. Contaminations of this channel are $^{214}$Bi and $^{208}$Tl (and other isotopes from natural radioactive chains) . The contamination level has been studied to determine the background contribution in the $\beta\beta$ candidate signal from the Neodinium foil .

Preliminary results for a total time acquisition of 10560 hours give 756 $\beta\beta$-like events with signal over background ratio $\frac{S}{B}$=3.4 in the [400-3600] keV full spectra. The half-life of the $2\nu\beta\beta$ process is :

$$T_{1/2}(2\nu) = (9.75 \pm 0.35(stat.) \pm 0.85(syst.))10^{18} years \quad (4)$$

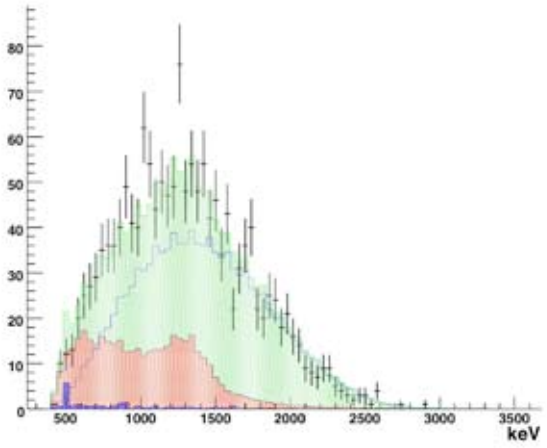


Figure 3: Total energy spectra in the two internal electron channel. Dots are real data. Blue/red histograms represent the expected contamination from external/internal background. The blue line is the $2\nu\beta\beta$ contribution. The green histogram represents the sum of all contributions mentioned previously.

There is no expected background event in the [3-3.6] MeV energy range. No $0\nu\beta\beta$ candidate event have been observed in the 10560 hours data sample from $^{150}$Nd foil. The limit obtained is $T_{1/2}(0\nu) > 8.0 \quad 10^{21}$ y at 90% CL for the light majorana exchange hypothesis. Up to now there is no lepton number violation evidence using $^{150}$Nd data in the NEMO-3 detector.

## References

1. NEMO Coll.,Technical design and performance of the NEMO-3 detector *Nucl. Instrum. Methods* A **536** 2005

# WIMP MASS FROM DIRECT, INDIRECT DARK MATTER DETECTION EXPERIMENTS AND COLLIDERS: A COMPLEMENTARY AND MODEL-INDEPENDENT APPROACH.

Nicolás Bernal
*Laboratoire de Physique Théorique, Bâtiment 210,*
*Université Paris-Sud XI, 91405 Orsay Cedex, France*

We study the possibility of identifying dark matter properties from direct (XENON100) and indirect (GLAST) detection experiments. In the same way, we examine the perspectives given by the next generation of colliders (ILC). All this analysis is done following a model-independent approach. We have shown that the three detection techniques can act in a highly complementary way. whereas direct detection experiments will probe efficiently light WIMPs, given a positive detection (at the 10% level for $m_\chi \sim 50$ GeV), GLAST will be able to confirm and even increase the precision in the case of a NFW profile, for a WIMP-nucleon cross-section $\sigma_{\chi-p} < 10^{-8}$ pb. However, for heavier WIMP ($\sim 175$ GeV), the ILC will lead the reconstruction of the mass.

## 1 Direct detection

Dark Matter (DM) direct detection experiments measure the elastic collisions between WIMPs and target nuclei in a detector, as a function of the recoil energy $E_r$. The detection rate depends on the density $\rho_0 \simeq 0.3$ GeV cm$^{-3}$ and velocity distribution $f(v_\chi)$ of WIMPs near the Earth (a Maxwellian halo will be considered). The differential rate per unit detector mass and per unit of time can be written as:

$$\frac{dN}{dE_r} = \frac{\sigma_{\chi-N}\,\rho_0}{2\,m_r^2\,m_\chi}\,F(E_r)^2 \int_{v_{min}(E_r)}^{\infty} \frac{f(v_\chi)}{v_\chi}\,dv_\chi\,, \tag{1}$$

where $\sigma_{\chi-N}$ is the WIMP-nucleus scattering cross section, $m_\chi$ the WIMP mass and $m_r$ is the WIMP-nucleon reduced mass. $F(E_r)$ is the nucleus form factor; we assume it has the Woods-Saxon form.

The XENON [1] experiment aims at the direct detection of DM via its elastic scattering off xenon nuclei. In this study we will consider the case of a 100 kg Xenon-like experiment and 3

years taking data. We consider 7 energy bins between 4 and 30 keV. For this experiment we took a zero background scenario; of course a more detailed analysis could take into account non-zero background simulating the detector and in particular the neutron spectrum. So, in that sense our results will be optimistic.

One option to discriminate between a DM signal and the background is to use the $\chi^2$ method. Let us call $N^{sign}$ the signal, $N^{bkg}$ the background and $N^{tot} \equiv N^{sign} + N^{bkg}$ the total signal measured by the detector. For an energy range divided into $n$ bins the $\chi^2$ is defined as:

$$\chi^2 = \sum_{i=1}^{n} \left( \frac{N_i^{tot} - N_i^{bkg}}{\sigma_i} \right)^2 . \tag{2}$$

We assume a Gaussian error $\sigma_i \equiv \sqrt{\frac{N_i^{tot}}{M \cdot T}}$ on the measurement, where $M$ is the detector mass and $T$ the exposure time.

## 2 Indirect detection

The spectrum of gamma–rays generated in dark matter annihilations and coming from the galactic center can be written as

$$\Phi_\gamma(E_\gamma) = \sum_i \frac{dN_\gamma^i}{dE_\gamma} Br_i \langle \sigma v \rangle \frac{1}{8\pi\, m_\chi^2} \int_{line\ of\ sight} \rho^2\ dl\ , \tag{3}$$

where the discrete sum is over all dark matter annihilation channels, $dN_\gamma^i/dE_\gamma$ is the differential gamma–ray yield, $\langle \sigma v \rangle$ is the annihilation cross-section averaged over the WIMPs' relative velocity distribution and $Br_i$ is the branching ratio of annihilation into the $i$-th final state. It is possible to concentrate ourselves on a process which gives 100% annihilation into $WW$ pairs, as this choice will not influence significantly the result of the study [2]. The dark matter density $\rho$ is usually parametrized as

$$\rho(r) = \frac{\rho_0}{(r/R)^\gamma \left[1 + (r/R)^\alpha\right]^{(\beta-\gamma)/\alpha}}. \tag{4}$$

We assume a NFW profile with $\alpha = \gamma = 1$, $\beta = 3$ and $R = 20$ kpc, producing a profile with a behavior $\rho(r) \propto r^{-\gamma}$ in the inner region of the galaxy.

The gamma-ray telescope GLAST [3] will perform an all-sky survey covering an energy range $1 - 300$ GeV. We will consider a GLAST-like experience with an effective area and angular resolution on the order of $10^4$ cm$^2$ and $0.1^\circ \times 0.1^\circ$ ($\Delta\Omega \simeq 10^{-5}$ sr) respectively, who will be able to point and analyze the inner centre of our galaxy. We consider also 3 years of effective data acquisition experiment.
For this experiment, the background can be modeled by interpolating [2] the gamma-ray spectrum measured by HESS [4] (for $E_\gamma > 160$ GeV) and EGRET [5] (for $E_\gamma < 10$ GeV) missions.

## 3 Colliders

Recently an approach was proposed by A. Birkedal et al.[6] which allows to perform a model-independent study of WIMP properties at lepton colliders. Since the known abundance of DM gives specific values for the DM annihilation cross section, one might hope this cross section can be translated into a rate for a measurable process at a collider.
The starting point is to relate total annihilation cross section to the cross section into $e^+e^-$ pairs

$$\kappa_e \equiv \sigma(\chi\chi \to e^+e^-)/\sigma(\chi\chi \to all). \tag{5}$$

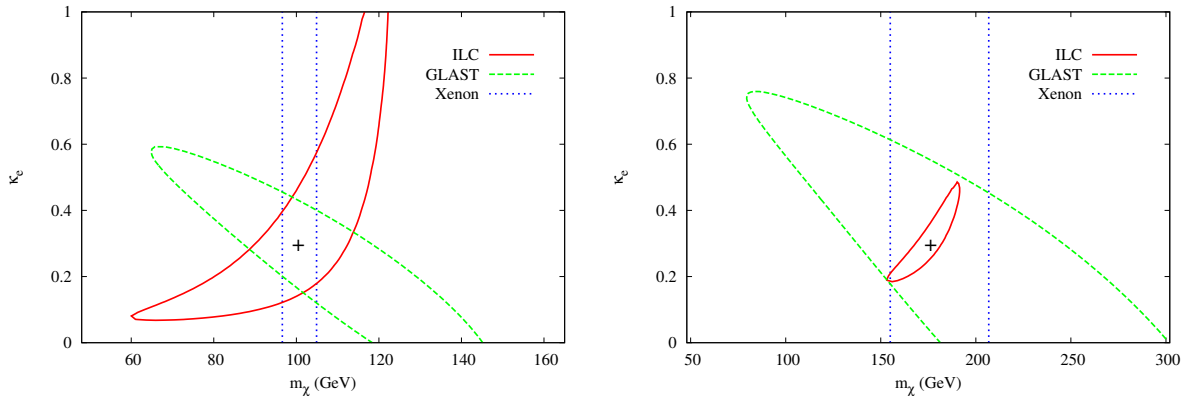


Figure 1: Comparison between a 100 kg XENON-like experiments (dotted line) with $\sigma_{\chi-p} = 10^{-7}$ pb, GLAST (dashed line) in the case of an NFW halo profile with $\langle\sigma v\rangle = 3 \cdot 10^{-26}$ cm$^3$s$^{-1}$, and unpolarized ILC sensitivity (solid line) at $2\sigma$ of confidence level, for different WIMP masses $m_\chi = 100$ and 175 GeV, and $\kappa_e = 0.3$.

Then we can use the *detailed balancing* equation to relate $\sigma(\chi\chi \to e^+e^-)$ to $\sigma(e^+e^- \to \chi\chi)$, for non-relativistic WIMPs. But this kind of process containing only WIMPs in the final state is not visible in a collider since they manifest themselves just as missing energy. However this process can be correlated to the radiative WIMP pair-production $\sigma(e^+e^- \to \gamma\,\chi\chi)$ using the *collinear factorization*. This approach is valid for photons which are either soft or collinear with respect to the colliding beams. The accuracy of the approximation outside the previous region has been discussed [6] with the conclusion that the approach works quite well.
So, starting from the total annihilation cross section $\sigma_{an}$ we can compute $\sigma(e^+e^- \to \gamma\,\chi\chi)$

$$\frac{d\sigma(e^+e^- \to \chi\chi\gamma)}{dx\,dcos\theta} \approx \frac{\alpha\,\kappa_e\,\sigma_{an}}{16\,\pi}\,\frac{1+(1-x)^2}{x}\,\frac{1}{\sin^2\theta}\,2^{2\,J_0}\,(2S_\chi+1)^2\left(1-\frac{4\,m_\chi^2}{(1-x)\,s}\right)^{1/2+J_0} . \quad (6)$$

Here $x \equiv 2\,E_\gamma/\sqrt{s}$, $\theta$ is the angle between the photon and the incoming beam, $S_\chi$ and $J_0$ are the spin of the WIMP and the dominant value of the angular momentum in the velocity expansion for $\langle\sigma v\rangle$.
We place ourselves in the framework of the ILC project with a center-of-mass energy of $\sqrt{s} = 500$ GeV and an integrated luminosity of 500 fb$^{-1}$. For this process with only a single photon detected, the main background in the standard model is radiative neutrino production [2].

## 4 Complementarity

Recently, several works have studied the determination of the WIMP mass for the case of direct[7] and indirect [8] detection experiments. Furthermore, Drees and Shan [9] showed that one can increase such a precision with a combined analysis of two experiments of direct detection.
In figure 1 we compare the precision levels for direct and indirect detection experiments, along with the corresponding results of the method we followed for the ILC for $\kappa_e = 0.3$ and two cases of WIMP masses $m_\chi = 100$ (left panel) and 175 GeV (right panel). All the results are plotted for a $2\sigma$ confidence level. The green-dashed lines correspond to the results for a GLAST-like experiment assuming a NFW halo profile. The total annihilation cross-section has been taken to be $\langle\sigma v\rangle = 3 \cdot 10^{-26}$ cm$^3$s$^{-1}$. The red-plain line represents the result for an ILC-like collider with non-polarized beams. The blue-dotted line corresponds to a 100 kg XENON-like experiment, assuming a WIMP-nucleus scattering cross-section of $10^{-7}$ pb. All the parameter space points that lie within the marked regions can not be discriminated by the corresponding experiments. It is pertinent to study the complementarity between the three experiences listed above firstly

Table 1: Precision on a WIMP mass expected from the different experiments at $2\sigma$ after 3 years of exposure, for $\sigma_{\chi-p} = 10^{-7}$ pb, a NFW profile and a 500 GeV unpolarized linear collider with a luminosity of 500 fb$^{-1}$. All values are given in GeV.

| $m_\chi$ | XENON | GLAST | ILC |
|---|---|---|---|
| 50 | $\pm$ 1 | $\pm$ 8 | ** |
| 100 | $\pm$ 6 | $-25/+32$ | $-40/+20$ |
| 175 | $-25/+35$ | $-70/+100$ | $-20/+15$ |
| 500 | $-250/**$ | $-350/**$ | ** |

because the mass reconstruction yields comparable results, hence a combination of these data can substantially improve the final result. Secondly, because we can probe different regions in the parameter space.
For the case of a 100 GeV WIMP, a GLAST- or an ILC-like experiment alone can provide a limited precision for the WIMP mass ($\sim$ 60%). Combined measurements can dramatically increase the precision , reaching an accuracy of $\sim$ 25%. If we additionally include direct detection measurement, we can reach a precision of the order of $\sim$ 9%.

In table 1 we show the precision expected for several dark DM masses. A light WIMP mass ($\sim$ 50 GeV) can be reconstructed by both direct and indirect DM experiments with a high level of precision; however for the ILC the model independent procedure fails because of the relativistic nature of the WIMP. On the contrary, the ILC will be particularly efficient to measure a WIMP with a mass of about 175 GeV. Concerning a 500 GeV WIMP, only a loose lower bound could be extracted form direct and indirect experiments. In this case the ILC will not be kinematically able to produce so heavy WIMPs.

## Acknowledgments

I would like to thank the organising committee for inviting me at this pleasant conference. Likewise, I would like to thank the ENTApP Network of the ILIAS project RII3-CT-2004-506222 and the French ANR project PHYS@COL&COS for financial support. The work reported here is based in collaboration with A. Goudelis, Y. Mambrini and C. Muñoz.

## References

1. J. Angle *et al.* [XENON Collaboration], Phys. Rev. Lett. **100** (2008) 021303 [arXiv:0706.0039 [astro-ph]].
2. N. Bernal, A. Goudelis, Y. Mambrini and C. Muñoz, arXiv:0804.1976 [hep-ph].
3. N. Gehrels and P. Michelson, Astropart. Phys. **11**, 277 (1999).
4. F. Aharonian *et al.* [The HESS Collaboration], Astron. Astrophys. **425** (2004) L13 [arXiv:astro-ph/0408145].
5. S. D. Hunger *et al.*, Astrophys. J. **481** (1997) 205.
6. A. Birkedal, K. Matchev and M. Perelstein, Phys. Rev. D **70**, 077701 (2004) [arXiv:hep-ph/0403004].
7. A. M. Green, JCAP **0708** (2007) 022 [arXiv:hep-ph/0703217]; A. M. Green, arXiv:0805.1704 [hep-ph].
8. S. Dodelson, D. Hooper and P. D. Serpico, Phys. Rev. D **77** (2008) 063512 [arXiv:0711.4621 [astro-ph]].
9. M. Drees and C. L. Shan, arXiv:0803.4477 [hep-ph]; C. L. Shan and M. Drees, arXiv:0710.4296 [hep-ph].

# $\ell_1 \to \ell_2\gamma$ in type III seesaw

F. BONNET [a]
*Laboratoire de Physique Théorique UMR 8627,*
*Université Paris-Sud 11, Bat. 210, 91405 Orsay Cedex, France*

We study the decay rates of the $\mu \to e\gamma$ and $\tau \to \ell\gamma$ transitions in the framework of the type III seesaw model, where fermionic triplets are exchanged to generate neutrino masses. We show that the observation of one of those decays in planned experiments would contradict bounds arising from present experimental limits on the $\mu \to eee$ and $\tau \to 3l$ decay rates, and therefore imply that there exist other sources of lepton flavour violation than those associated to triplet of fermions.

## 1 Introduction

The Standard Model (SM) has the unique property of conserving flavour in the leptonic sector. However, since the experimental discovery of neutrino oscillations, we know that lepton flavour is violated in the neutrino sector. Neutrinos mass naturally arises within the framework of the seesaw mechanism (via the exchange of heavy fields). In such models flavour violating rare leptonic decays such as $\mu \to e\gamma$ and $\tau \to \ell\gamma$ are expected to be relevant. These decays have already been studied in type I [1] and type II [2] seesaw models. In the following, we study these decays in the framework of the type III seesaw model [3,4], where heavy triplets of fermions are exchanged.

## 2 The type-III Seesaw model

The type-III seesaw model consists in adding $SU(2)_L$ triplets of fermions $\Sigma$, with zero hypercharge, to the SM. At least two triplets are needed to account for the observation of neutrino masses, but in fact only one is sufficient to generate non-vanishing $\ell_1 \to \ell_2\gamma$ rate. In the following we will not specify the number of triplets. The heavy fermions are in the adjoint representation

[a] florian.bonnet@th.u-psud.fr

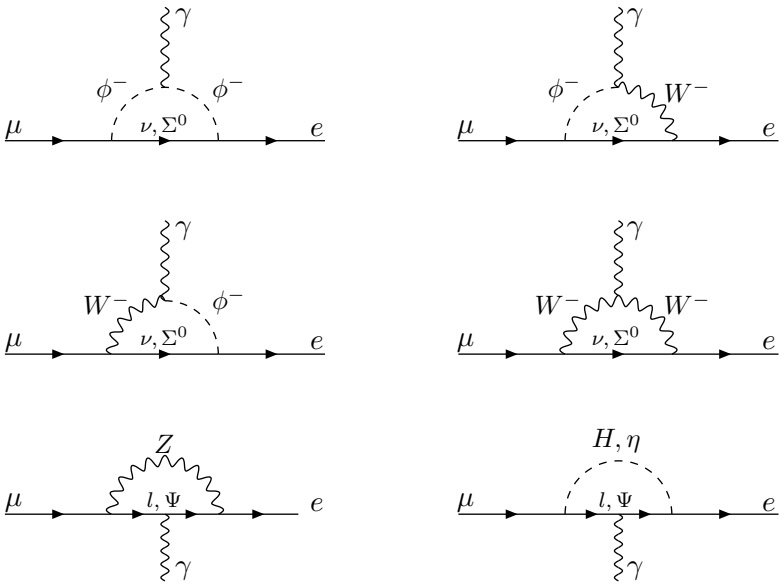


Figure 1: Diagrams contributing to the $\mu \to e\gamma$ transition. $\phi^{\pm}$, $\eta$ denote the three Goldstone bosons associated with the $W^-$ and $Z$ bosons. $H$ stands for the physical Higgs boson, and $\Psi = \Sigma_R^{+c} + \Sigma_R^-$.

of the $SU(2)_L$ group and have a gauge invariant Majorana mass term. The Lagrangian of its interactions reads:

$$\mathcal{L} = Tr[\overline{\Sigma} i \not{D} \Sigma] - \frac{1}{2} Tr[\overline{\Sigma} M_\Sigma \Sigma^c + \overline{\Sigma^c} M_\Sigma^* \Sigma] - \tilde{\phi}^\dagger \overline{\Sigma} \sqrt{2} Y_\Sigma L - \overline{L} \sqrt{2} Y_\Sigma{}^\dagger \Sigma \tilde{\phi}\,, \tag{1}$$

where $L \equiv (l, \nu)^T$, $\phi \equiv (\phi^+, \phi^0)^T \equiv (\phi^+, (v + H + i\eta)/\sqrt{2})^T$, $\tilde{\phi} = i\tau_2 \phi^*$, $\Sigma^c \equiv C\overline{\Sigma}^T$ and with, for each fermionic triplet,

$$\Sigma \;=\; \begin{pmatrix} \Sigma^0/\sqrt{2} & \Sigma^+ \\ \Sigma^- & -\Sigma^0/\sqrt{2} \end{pmatrix}, \quad \Sigma^c = \begin{pmatrix} \Sigma^{0c}/\sqrt{2} & \Sigma^{-c} \\ \Sigma^{+c} & -\Sigma^{0c}/\sqrt{2} \end{pmatrix}. \tag{2}$$

After electroweak symmetry breaking, the neutrino mass matrix is given by: $m_\nu = -\frac{v^2}{2} Y_\Sigma^T \frac{1}{M_\Sigma} Y_\Sigma$. The new Yukawa couplings are the source of mixing between the light leptons and the heavy fermions, which, combined with the presence of the Majorana mass term, allow lepton flavour violating processes. Thus, the study of these processes will enable to derive some bounds on the new couplings: $Y_\Sigma$ and $M_\Sigma$

## 3 Flavour changing radiative leptonic decays

We briefly describe the main steps of the calculation of the $\mu \to e$ rate. The $\tau$ decay rates will straightforwardly follow. The on-shell transition $\mu \to e\gamma$ is a magnetic transition, and it can be written, in the limit $m_e \to 0$, as:

$$T(\mu \to e\gamma) = A \times \overline{u_e}(p - q) \left[ i q^\nu \varepsilon^\lambda \sigma_{\lambda\nu} (1 + \gamma_5) \right] u_\mu(p)\,, \tag{3}$$

where $\varepsilon$ is the polarization of the photon, $p_\mu$ the momentum of the incoming muon, $q_\mu$ the momentum of the outgoing photon and $\sigma_{\mu\nu} = \frac{i}{2}[\gamma_\mu, \gamma_\nu]$. The fourteen diagrams contributing to these decays are shown in Fig. 1. The details of the calculation can be found in the related paper [5]. In the limit $M_\Sigma \gg M_W$, at $\mathcal{O}((\frac{Y_\Sigma v}{M_\Sigma})^2)$, the total amplitude is given by:

$$\begin{aligned} T(\mu \to e\gamma) \;&=\; i \frac{G_F^{SM}}{\sqrt{2}} \frac{e}{32\pi^2} m_\mu \overline{u_e}(p - q)(1 + \gamma_5)\, i\sigma_{\lambda\nu} \varepsilon^\lambda q^\nu u_\mu(p) \\ &\times\; \left\{ \left( \frac{13}{3} + C \right) \epsilon_{e\mu} - \sum_i x_{\nu_i} (U_{PMNS})_{ei} \left( U_{PMNS}^\dagger \right)_{i\mu} \right\}, \end{aligned} \tag{4}$$

where $C = -6.56$, $\epsilon = \frac{v^2}{2} Y_\Sigma^\dagger M_\Sigma^{-2} Y_\Sigma$ and $x_{\nu_i} \equiv \frac{m_{\nu_i}^2}{M_W^2}$. The first part of the amplitude correspond to the contribution of the fermionic triplet, while the second one is the usual contribution from neutrino mixing (suppressed by a GIM cancellation). The branching ratio then reads :

$$Br\left(\mu \to e\gamma\right) = \frac{3}{32}\frac{\alpha}{\pi}\left|\left(\frac{13}{3} + C\right)\epsilon_{e\mu} - \sum_i x_{\nu_i}\left(U_{PMNS}\right)_{ei}\left(U_{PMNS}^\dagger\right)_{i\mu}\right|^2 . \tag{5}$$

$\tau \to l\gamma$ decays can be obtained from Eq. (5) by replacing $\mu$ by $\tau$, $e$ by $l$ and by multiplying the obtained result by[6] $Br(\tau \to e\nu_\tau\bar{\nu}_e) = (17.84 \pm 0.05)\cdot 10^{-2}$. Since the neutrino mixing contribution is extremely suppressed, it cna be neglected when compared to the present experimental bounds on the branching ratios[6,7]. This allow us to convert these experimental bounds into bounds on the $\epsilon_{\alpha\beta}$ coefficients :

$$|\epsilon_{e\mu}| = \frac{v^2}{2}|Y_\Sigma^\dagger \frac{1}{M_\Sigma^\dagger}\frac{1}{M_\Sigma} Y_\Sigma|_{\mu e} \leq 1.1 \cdot 10^{-4}, \tag{6}$$

$$|\epsilon_{\mu\tau}| = \frac{v^2}{2}|Y_\Sigma^\dagger \frac{1}{M_\Sigma^\dagger}\frac{1}{M_\Sigma} Y_\Sigma|_{\tau\mu} \leq 1.5 \cdot 10^{-2}, \tag{7}$$

$$|\epsilon_{e\tau}| = \frac{v^2}{2}|Y_\Sigma^\dagger \frac{1}{M_\Sigma^\dagger}\frac{1}{M_\Sigma} Y_\Sigma|_{\tau e} \leq 2.4 \cdot 10^{-2} . \tag{8}$$

## 4 Comparison to $\mu \to eee$ and $\tau \to 3\ell'$ decays

The presence of heavy fermions not only allows for one-loop lepton flavour violating processes, but also for tree level decays such as $\mu \to eee$ and $\tau \to 3\ell'$. The latter branching ratios have already been calculated in the type III seesaw model[4]. It turns out that the bounds obtained from these decays exactly apply on the same parameters $\epsilon$ as those obtained in Eqs. (6)-(8). To understand this property let us study the example of $\mu \to e\gamma$ and $\mu \to eee$ . In both cases one wants to link a muon to an electron with a same fermionic line. The only way to achieve this is to mix a muon and an electron with a fermionic triplet. This implies that the flavour structure of the $\mu$-to-$e$ fermionic line is the same in both processes. Regarding the couplings, there is only one way to combine two Yukawa couplings and two inverse $M_\Sigma$ mass matrices to induce a $\mu$-to-$e$ transition along a fermionic line: $\epsilon_{e\mu}$. This relation between the two types of decays implies that the ratios of these branching ratios are fixed :

$$Br(\mu \to e\gamma) = 1.3 \cdot 10^{-3} \cdot Br(\mu \to eee)\,, \tag{9}$$

$$Br(\tau \to \mu\gamma) = 1.3 \cdot 10^{-3} \cdot Br(\tau \to \mu\mu\mu) = 2.1 \cdot 10^{-3} \cdot Br(\tau^- \to e^-e^+\mu^-)\,, \tag{10}$$

$$Br(\tau \to e\gamma) = 1.3 \cdot 10^{-3} \cdot Br(\tau \to eee) = 2.1 \cdot 10^{-3} \cdot Br(\tau^- \to \mu^-\mu^+e^-)\,. \tag{11}$$

Since the processes $\ell \to 3\ell'$ occur at tree level in this model while the $\ell \to \ell'\gamma$ ones are one-loop, small values of the ratios are expected[b]. The $\mu \to eee$, $\tau \to eee$ and $\tau \to \mu\mu\mu$ decays lead to[4] $|\epsilon_{e\mu}| < 1.1 \cdot 10^{-6}$, $|\epsilon_{\mu\tau}| < 4.9 \cdot 10^{-4}$, $|\epsilon_{e\tau}| < 5.1 \cdot 10^{-4}$. Those bounds are better than the one obtained in Eqs. (6)-(8). This means that in this model the tree-level processes will provide the most competitive bounds on the $\epsilon_{\alpha\beta}$ parameters, even if the the experimental limit on the branchng ratios of the radiative decays improves by two order of magnitude. Using the experimental bounds[6,8] $Br(\mu \to eee) < 1 \cdot 10^{-12}$, $Br(\tau \to eee) < 3.6 \cdot 10^{-8}$ and $Br(\tau \to \mu\mu\mu) < 3.2 \cdot 10^{-8}$, one derives predictions for the bounds on branching ratios of the radiative decays :

$$Br(\mu \to e\gamma) < 10^{-15} \tag{12}$$

[b] Note that these ratios are obtained in the limit where $M_\Sigma \gg M_{W,Z,H}$. Not working in this limit, these ratios can vary up to one order of magnitude.

$$Br(\tau \to \mu\gamma) \quad < \quad 4 \cdot 10^{-11} \tag{13}$$
$$Br(\tau \to e\gamma) \quad < \quad 5 \cdot 10^{-11} \tag{14}$$

to be compared with experimental bounds[6,7] : $\mathrm{Br}(\mu \to e\gamma) < 1.2{\cdot}10^{-11}$, $\mathrm{Br}(\tau \to \mu\gamma) < 4.5{\cdot}10^{-8}$, $\mathrm{Br}(\tau \to e\gamma) < 1.1 \cdot 10^{-7}$ [6].

## 5 Conclusion

In our work we were lead to the conclusion that the observation of one leptonic radiative decay in the upcoming experiments will rule out the seesaw mechanism with only fermion triplets. Indeed this would contradict bounds arising from present experimental limits on the $\mu \to eee$ and $\tau \to 3l$ decay rates, and therefore imply that there exist other sources of lepton flavour violation than those associated to triplet of fermions.

## Acknowledgments

I would like to thanks the organisers of the XLIII Rencontres de Moriond for giving me the opportunity to give a talk in this conference and for the enjoyable atmosphere. This work was funded in part by a grant from the European Union "Marie Curie" program, and from the Agence Nationale de Recherche ANR through the project JC05-43009-NEUPAC.

## References

1. See for instance : C. S. Lim and T. Inami, Prog. Theor. Phys. **67** (1982) 1569; P. Langacker and D. London, Phys. Rev. D **38** (1988) 907; W. J. Marciano and A. I. Sanda, Phys. Lett. B **67** (1977) 303; T. P. Cheng and L. F. Li, Phys. Rev. Lett. **45** (1980) 1908; B. W. Lee and R. E. Shrock, Phys. Rev. D **16** (1977) 1444; E. Ma and A. Pramudita, Phys. Rev. D **24** (1981) 1410; S. M. Bilenky, S. T. Petcov and B. Pontecorvo, Phys. Lett. B **67** (1977) 309.
2. J. Bernabeu, A. Pich and A. Santamaria, Phys. Lett. **B148**, 229 (1984); S. M. Bilenky and S. T. Petcov, Rev. Mod. Phys. **59** (1987) 671 [Erratum-ibid. **61** (1989) 169]; R. N. Mohapatra, Phys. Rev. D **46** (1992) 2990.
3. R. Foot, H. Lew, X.-G. He and G.C. Joshi, Z. Phys. C44 (1989) 441; E. Ma, Phys. Rev. Lett. **81** (1998) 1171 [arXiv:hep-ph/9805219]; E. Ma and D. P. Roy, Nucl. Phys. B **644**, 290 (2002) [arXiv:hep-ph/0206150]; T. Hambye, L. Yin, A. Notari, M. Papucci and A. Strumia, Nucl. Phys. B **695**, 169 (2004) [arXiv:hep-ph/0312203]; B. Bajc and G. Senjanovic, JHEP **0708** (2007) 014 [arXiv:hep-ph/0612029]; B. Bajc, M. Nemevsek and G. Senjanovic, Phys. Rev. D **76** (2007) 055011 [arXiv:hep-ph/0703080]; I. Dorsner and P. Fileviez Perez, JHEP **0706** (2007) 029 [arXiv:hep-ph/0612216]; P. F. Perez, Phys. Lett. B **654** (2007) 189 [arXiv:hep-ph/0702287] and Phys. Rev. D **76** (2007) 071701 [arXiv:0705.3589 [hep-ph]].
4. A. Abada, C. Biggio, F. Bonnet, M. B. Gavela and T. Hambye, JHEP **12** (2007) 061 [arXiv:0707.4058 [hep-ph]].
5. A. Abada, C. Biggio, F. Bonnet, M. B. Gavela and T. Hambye, arXiv:0803.0481 [hep-ph].
6. W. M. Yao *et al.* [Particle Data Group], J. Phys. G **33** (2006) 1 (and 2007 partial update for edition 2008).
7. K. Hayasaka *et al.* [Belle Collaboration], arXiv:0705.0650 [hep-ex].
8. K. Abe et al. [Belle Collaboration], Phys. Lett. **B660** (2008) 154.

# NC COHERENT $\pi^0$ PRODUCTION IN THE MiniBooNE ANTINEUTRINO DATA

V. T. NGUYEN
*Department of Physics, Columbia University, 538 W 120th ST, New York, NY 10027*

The single largest background to future $\bar{\nu_\mu} \to \bar{\nu_e}$ ($\nu_\mu \to \nu_e$) oscillation searches is neutral current (NC) $\pi^0$ production. MiniBooNE, which began taking antineutrino data in January 2006, has the world's largest sample of reconstructed $\pi^0$'s produced by antineutrinos. These neutral pions are primarily produced through the $\Delta$ resonance but can also be created through "coherent production." The latter process is the coherent sum of glancing scatters of antineutrinos off a neutron or proton, in which the nucleus is kept intact but a $\pi^0$ is created. A signature of this process is a $\pi^0$ which is highly forward-going. It is advantageous to study coherent production using antineutrinos rather than neutrinos because the ratio of coherent to resonant scattering is enhanced in antineutrino running. The first measurement of NC coherent $\pi^0$ production in the MiniBooNE antineutrino data is discussed here.

## 1 Neutral Current $\pi^0$ Production

At low energy, neutral current (NC) $\pi^0$'s are produced via two different mechanisms:

$$\bar{\nu}N \to \bar{\nu}\Delta \to \bar{\nu}\pi^0 N \qquad (resonant) \tag{1}$$

$$\bar{\nu}A \to \bar{\nu}A\pi^0 \qquad (coherent) \tag{2}$$

In resonant $\pi^0$ production, a(n) (anti)neutrino interacts with the target, exciting the nucleon into a $\Delta^0$ or $\Delta^+$, which then decays to a nucleon plus $\pi^0$ final state. In coherent $\pi^0$ production, very little energy is exchanged between the (anti)neutrino and the target. The nucleus is left intact but a $\pi^0$ is created from the coherent sum of scattering from all the nucleons. A signature of this process is a $\pi^0$ which is highly forward-going.

### *1.1 Why Study NC $\pi^0$ Production?*

NC $\pi^0$ events are the dominant background to $\bar{\nu_\mu} \rightarrow \bar{\nu_e}$ ($\nu_\mu \rightarrow \nu_e$) oscillation searches. A $\pi^0$ decays very promptly into two photons ($\tau_{\pi^0} \sim$ 8x10$^-$17s), and can mimic a $\bar{\nu_e}$ ($\nu_e$) interaction if only one photon track is resolvable in a detector.

In particular, coherent production is much more challenging to predict theoretically than resonant processes. Unfortunately, there are currently only two published measurements of the absolute rate of antineutrino NC $\pi^0$ production (Figure 1); the lowest energy measurement reported with 25% uncertainty at 2 GeV [1]. There exist no experimental measurements below 2 GeV. Furthermore, current theoretical models on coherent $\pi^0$ production [2,3,4] can vary by up to an order of magnitude in their predictions at low energy, the region most relevant for (anti)neutrino oscillation experiments.

The analysis presented at the 43rd Rencontres de Moriond represents the first time we are experimentally probing this process in this energy region.

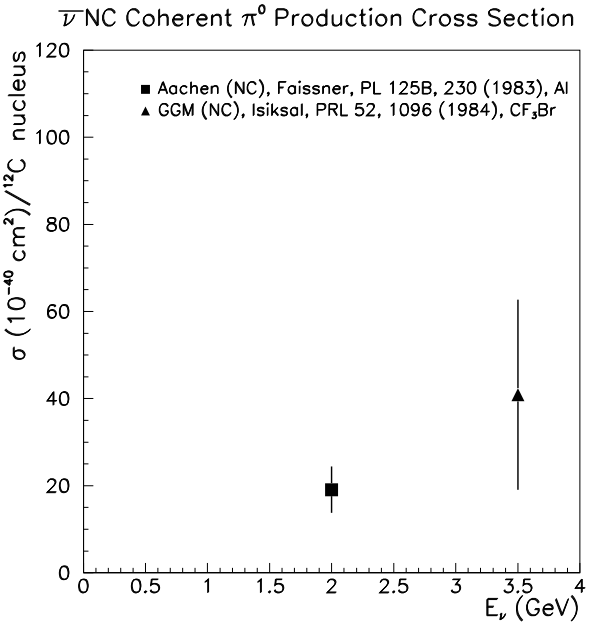


Figure 1: World data on antineutrino NC coherent $\pi^0$ production at low energy.

## 2 The MiniBooNE Experiment

The Mini Booster Neutrino Experiment (MiniBooNE) [5], an experiment at Fermilab designed to measure $\nu_\mu \rightarrow \nu_e$ oscillations, turns out to be very well-suited for $\pi^0$ physics. Its large, open-volume Cherenkov detector with full angular coverage provides excellent $\pi^0$ identification and containment. In fact, MiniBooNE has the world's largest samples of NC $\pi^0$ events in interactions with $\sim$1 GeV neutrinos ($\sim$28k) and with $\sim$1 GeV antineutrinos ($\sim$1.7k). Additional POT has been collected in $\nu$ mode since the MiniBooNE oscillation results [5] with additional POT being collected in $\bar{\nu}$ mode currently.

## 3 Coherent $\pi^0$'s in Terms of $E_\pi(1 - \cos\theta_\pi)$ in $\bar{\nu}$ Mode

As mentioned before, coherent and resonant $\pi^0$ production are distinguishable by $\cos\theta_\pi$, which is the cosine of the lab angle of the outgoing $\pi^0$ with respect to the beam direction. It turns

out that it is even better to study coherent $\pi^0$'s in terms of the pion energy-weighted angular distribution since in coherent events, $E_\pi(1-\cos\theta_\pi)$ has a more regular shape as a function of momentum, than $\cos\theta_\pi$ alone. Thus, we will fit for the coherent content as a function of the pion energy-weighted angular distribution. Furthermore, we need to fit this quantity simultaneously with the invariant mass. This is due to the fact that, in the energy-weighted angular distribution, the resonant and background spectra have similar shapes that are distinct from the forward-peaking coherent spectrum while the resonant and coherent spectra have similar shapes in the invariant mass that are distinct from the background spectrum.

This fit has in fact been done in neutrino mode [6]. Preliminary fits to the antineutrino data were shown at this conference. This sample is important because in antineutrino scattering, there is a helicity suppression for most interactions, including resonant production of $\pi^0$'s, but not for coherent production. Thus, the ratio of coherent to resonant scattering, which is small, is expected to be enhanced in antineutrino running.

### *3.1 Preliminary Results*

Preliminary statistics-only fits between MiniBooNE antineutrino data and MC [a] are shown (Figures 2 and 3). The initial MC includes a rescaling of the Rein-Sehgal [8] coherent cross section based on the measurement in Ref. 6. These studies clearly show evidence for NC coherent $\pi^0$ production, as was the case in neutrino mode. When coherent $\pi^0$ production is absent from the MC (Figure 4), one can see the poor agreement between data and MC in the lower end of $E_\pi(1-\cos\theta_\pi)$, where most of the $\pi^0$'s are expected to be produced from coherent scattering. The agreement improves considerably when coherent $\pi^0$ production is included (Figure 3). Furthermore, the coherent fraction in both $\nu$ and $\bar{\nu}$ modes is roughly 1.5 times lower than the Rein-Sehgal [8] prediction, which is the most widely used model in (anti)neutrino experiments.

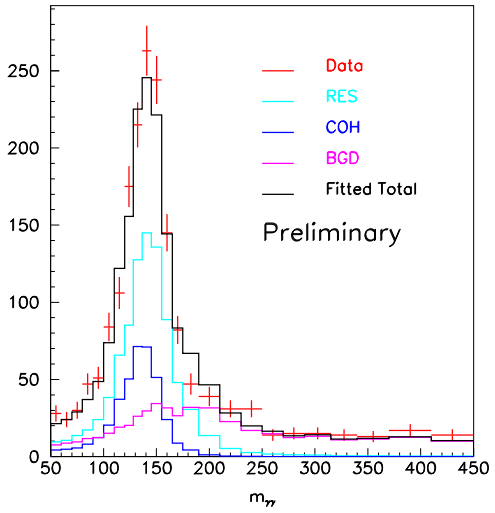


Figure 2: Preliminary statistics-only invariant mass fit.

## Acknowledgments

I would like to give many thanks to the MiniBooNE Collaboration and the NSF.

[a] RES = NUANCE channels 6,8,13, and 15. COH = NUANCE channel 96. BGD = NUANCE channels other than 6,8,13,15, and 96. MC TOT = RES + COH + BGD. See Ref. 7 for channel definitions.

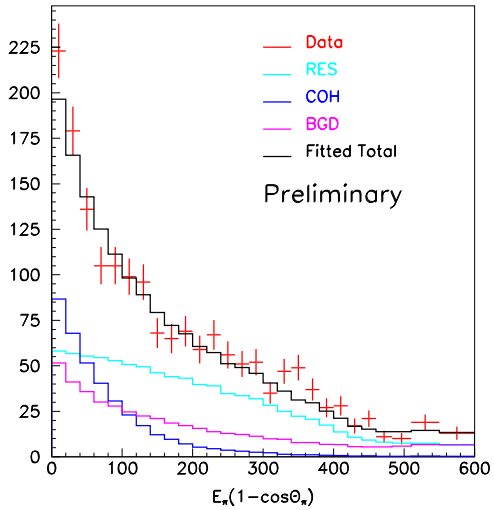


Figure 3: Preliminary statistics-only pion energy-weighted angular distribution fit.

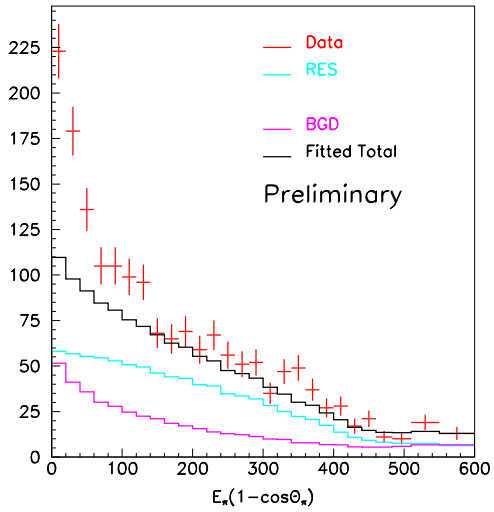


Figure 4: Preliminary statistics-only pion energy-weighted angular distribution fit with no coherent contribution in the total MC.

## References


1. see footnote on page 235 in H. Faissner *et al.*, Phys. Lett. **125B**, 230 (1983).
2. B. Z. Kopeliovich, arXiv:0409079 [hep-ph].
3. J. Marteau, arXiv:9906449 [hep-ph].
4. E. A. Paschos, arXiv:0309148 [hep-ph].
5. A. A. Aguilar-Arevalo *et al.* [MiniBooNE Collaboration], Phys. Rev. Lett. **98**, 231801 (2007).
6. J. M. Link *et al.* [MiniBooNE Collaboration], Phys. Lett. B **664/1-2**, 41-46 (2008).
7. D. Casper, Nucl. Phys. B, Proc. Suppl. **112**, 161 (2002).
8. D. Rein, L. M. Sehgal, Nucl. Phys. B223 29 (1983).